UC Berkeley
UC Berkeley Electronic Theses and Dissertations

Title
From actin to Zap70: the outcomes of the interaction of the actin cytoskeleton with T-cell receptors

Permalink
https://escholarship.org/uc/item/0cn4f9zp

Author
Smoligovets, Alexander Alexandrovich

Publication Date
2012

Peer reviewed|Thesis/dissertation

eScholarship.org Powered by the California Digital Library
University of California

From actin to Zap70: the outcomes of the interaction of the actin cytoskeleton with T-cell receptors

by
Alexander Alexandrovich Smoligovets

A thesis submitted in partial satisfaction of the
requirements for the degree of
Doctor of Philosophy
in
Molecular and Cell Biology
in the
Graduate Division
of the
University of California, Berkeley

Committee in charge:

Professor Jay T. Groves, Chair
Professor Ehud Isacoff, Co-chair
Professor Matthew Welch
Professor Ellen Robey
Professor Mohammad Mofrad

Fall 2012

Abstract

From actin to Zap70: the outcomes of the interaction of the actin cytoskeleton with T-cell receptors

by

Alexander Alexandrovich Smoligovets

Doctor of Philosophy in Molecular and Cell Biology

University of California, Berkeley

Professor Jay T. Groves, Chair
Professor Ehud Isacoff, Co-chair

The actin cytoskeleton has for decades been known to be important in the process of T-cell recognition of antigen. Upon receiving stimulus from T-cell receptors (TCRs), the T-cell cytoskeleton adopts a pattern of radially symmetric, centripetal flow that imposes multi-micrometer scale organization on the protein complement of a T-cell membrane. Many of the details of the interactions between actin and cell surface receptors remain unknown; of particular interest are the connections to TCRs themselves. The actin cytoskeleton appears to modulate TCR-mediated signaling, and thus T-cell behaviors, on a number of levels. On the level of single TCR molecules and oligomers, the presence of actin affects TCR-antigen recognition by altering binding kinetics through mechanisms that are still unclear. On a larger spatial and longer temporal level, actin drives the formation and centripetal movement of small TCR assemblies whose radial distribution correlates with their signaling state. Little is known about the local organization and dynamics of the actin cytoskeleton around these assemblies. A more complete understanding of the process of T-cell activation depends on the ability to characterize the involvement of actin in detail.

This thesis describes how the T-cell actin cytoskeleton locally reacts to TCR assemblies, how it modulates the kinetics of the TCR-antigen interaction, and what role myosin IIA plays in organization of and signaling by TCRs. Direct imaging of actin reveals that the cytoskeletal network transiently slows and compresses at sites of mobility-limited T-cell receptors. Actin disruption during direct observation of antigen peptide binding to TCRs shows that the presence of a functional cytoskeleton increases the rate of antigen unbinding from these receptors. Tracking and disruption of labeled myosin IIA indicates that the motor protein helps but is not required for proper establishment of T-cell membrane organization, but it is necessary for appropriate calcium influx into the T-cell cytoplasm during activation. For all of these observations and others, new experimental and analytical methods are developed or applied.

Acknowledgements

To properly acknowledge everyone who helped me complete the work that led to this thesis and to do justice to their contribution would take many more pages. I feel exceptionally fortunate to have worked with some brilliant people and to have been supported by wonderful friends and family. I hope that the following people will forgive me for the insufficiency of my brief words and that anyone who I omit knows that I am deeply grateful for all their help. I thank

- My collaborators in the Groves lab with whom I have published manuscripts: Adam Smith, Yan Yu, Geoff O'Donoghue, Hung-Jen Wu, Rafal Pielak, Nicole Fay, Jenny Lin, and Rebecca Petit. A special thank-you goes to Adam, who immediately and freely shared a lot of patience, trust, and mutual respect with a brand new graduate student who had done nothing to earn it.
- Former and current members of the T cell subgroup of the Groves lab with whom I have not directly published, but whose presence, guidance, and leftover (or custom-made) reagents have been invaluable: Niña Hartman, Boryana Manz, Cheng-Han Yu, Kate Alfieri, and Hiro Kai.
- Andy DeMond, whose impact on my Groves lab experience far outlasted the few months we actually worked together. Without Andy's mentorship, I may well have never joined the Groves lab.
- The rest of the Groves Lab Playaz, who are some of the smartest and most fun to work with people I have met.
- Pradeep Nair, who made sure that there was never a boring day in the lab while he was there, and who still gets talked about almost every day.
- Jay Groves, possibly the most enigmatic person I have ever met. After working for Jay for over five years, I still know almost nothing about him, but I cannot imagine a boss with more faith in his employees, which has made it tremendously rewarding and empowering to be in his lab. One day I hope to be as good as he is at getting people excited about their work and motivating themselves to get it done.
- My friends, old and new.
- My parents, who have constantly pushed me to be successful and supported me in every imaginable way.
- Rachel Haurwitz, who has been my inspiration ever since I met her. Every day I am with her, I marvel how lucky I must be to have someone so beautiful, smart, funny, quirky, and kind to share my life with.

Table of contents

Abstract.....1
Acknowledgements..... i
Table of contents..... ii
List of figures.....v

Chapter 1. Introduction: modulation of T-cell signaling by the actin cytoskeleton..... 1

1.1 Introduction…..... 2
1.2 Actin in T cell receptor triggering..... 3
1.3 Actin in microcluster assembly..... 4
1.4 Actin in spatial organization of the immunological synapse.....5
1.5 Molecular motors in TCR signaling.....9
1.6 Conclusion..... 10

Chapter 2. Characterization of dynamic actin associations with T-cell receptor microclusters in primary T cells.....11

2.1 Introduction..... 12
2.2 Materials and methods..... 13
2.2.1 DNA constructs.....13
2.2.2 Retroviral transduction of T cells..... 13
2.2.3 Preparation of T cells for imaging.....14
2.2.4 Microscopy..... 14
2.2.5 Actin motion analysis.....14
2.2.6 Image time-autocorrelation analysis.....15
2.3 Results.....15
2.3.1 Immunological synapse formation on supported lipid bilayers and nanopatterned substrates..... 15
2.3.2 Analysis of cortical actin flow in primary T cells.....17
2.3.3 Resistance-dependent slowing of actin at sites of TCR clusters.....19
2.3.4 Coordinated actin fluctuations near TCRs.....21
2.4 Discussion..... 23

Chapter 3. Ratiometric imaging of the T-cell actin cytoskeleton reveals the nature of dynamic receptor-induced cytoskeletal enrichment.....24

3.1 Introduction.....25
3.2 Materials and methods..... 25
3.3 Results.....25
3.4 Discussion..... 27

Chapter 4. Direct single molecule measurement of MHC/agonist:TCR unbinding kinetics in living primary T cells 28

4.1 Introduction 29
4.2 Materials and methods 29
4.2.1 DNA, protein, and T cell preparation 29
4.2.2 Peptide purification and labeling 30
4.2.3 Microscopy 30
4.2.4 Imaging chamber and supported lipid bilayer preparation 31
4.2.5 Data analysis 31
4.2.6 Stochastic kinetic simulation 32
4.3 Results 33
4.3.1 Hardware filtering and characterization of MHC/agonist:TCR complexes 33
4.3.2 Single molecule MHC/agonist:TCR kinetics 35
4.3.3 Stochastic reaction-diffusion simulations 37
4.4 Discussion 40

Chapter 5. Myosin IIA modulates T cell receptor transport and CasL phosphorylation during early immunological synapse formation 42

5.1 Introduction 43
5.2 Materials and methods 44
5.2.1 Animals 44
5.2.2 CD4+ cell harvest 44
5.2.3 DNA constructs 44
5.2.4 Reagents 44
5.2.5 Retroviral transfection 44
5.2.6 Bilayer assembly and cell imaging 45
5.2.7 Calcium imaging 45
5.2.8 Speckle tracking and image analysis 46
5.3 Results 46
5.3.1 Myosin IIA transiently drives translocation of TCR microclusters 46
5.3.2 Forces applied to TCR clusters are translated to myosin IIA 50
5.3.3 Myosin IIA is required for Ca^{2+} influx 51
5.3.4 Inhibition of myosin IIA reduces association of active ZAP-70 with TCR 52
5.3.5 Inhibition of myosin IIA reduces CasL phosphorylation 53
5.4 Discussion 54

Chapter 6. Patterned two-photon photoactivation illuminates spatial reorganization in live cells 56

6.1 Introduction 57

6.2 Materials and methods..... 58
6.2.1 Microscope..... 58
6.2.2 DNA constructs.....59
6.2.3 Phoenix cell culture, transfection, and retrovirion production..... 59
6.2.4 T-cell culture and transduction..... 60
6.2.5 T-cell imaging: preparation of substrates, buffers, and cells..... 60
6.2.6 Cos-7 cell culture, transfection, and preparation for imaging..... 61
6.2.7 Optical patterning..... 61
6.3 Results.....62
6.3.1 Patterned photoactivation in cells.....62
6.3.2 Spatial dynamics with singular value decomposition.....64
6.3.3 Actin dynamics in live T-cells.....67
6.4 Discussion..... 69

Chapter 7. Closing remarks..... 72

Bibliography.....74

List of figures

Figure 1.1. The actin cytoskeleton scaffolds signaling cluster assembly and drives the centripetal translocation of T cell receptor (TCR) microclusters during T cell activation..... 2
Figure 1.2. The hybrid live cell-nanopatterned supported lipid bilayer platform allows the coupling between TCR microclusters and actin or myosin to be examined..... 6
Figure 1.3. Custom particle identification and tracking algorithms reveal the dynamics of TCR microcluster motion and centripetal actin flow.....7
Figure 1.4. The model for size-dependent protein sorting in the immunological synapse.....8

Figure 2.1. The supported lipid bilayer allows visualization of the T cell cortical actin cytoskeleton during immunological synapse formation..... 16
Figure 2.2. Analysis methods for bulk cytoskeletal flow are distinct from those used to describe speckle motion.....18
Figure 2.3. Actin features slow down in TCR-rich regions..... 19
Figure 2.4. Increased actin escape times correspond to motion perpendicular to TCR diffusion barriers..... 20
Figure 2.5. Transient enrichments of the actin cytoskeleton occur at TCR clusters..... 22

Figure 3.1. Ratiometric imaging of the cytoskeleton in live T cells distinguishes between dynamic and stable actin populations..... 26
Figure 3.2. Dynamic receptor-induced cytoskeletal enrichment at sites of pinned TCRs corresponds to a primarily stable actin fraction..... 27
Figure 3.3. Three-dimensional ratiometric imaging shows that actin enrichment extends away from the cell membrane..... 27

Figure 4.1. A slow mobility MCC fraction is observed after addition of live T cells..... 34
Figure 4.2. The slow mobility MCC/agonist fraction recruits Zap70, follows linear trajectories similar to Zap70, and is agonist-specific..... 35
Figure 4.3. TCR and MCC colocalization.....36
Figure 4.4. Peptide specificity is independent of fluorophore..... 36
Figure 4.5. The distribution of live cell single molecule MCC/I-E^k-TCR dwell times is observed directly..... 37
Figure 4.6. Stochastic reaction-diffusion simulation of time before MCC escape from TCR clusters, τ_{esc}.....38
Figure 4.7. Simulations of $\frac{\tau_{esc}}{\tau_{off}}$ as a function of TCR cluster size, τ_{off}, and k_{on}..... 39
Figure 4.8. Interaction of the 226 TCR with the MCC peptide..... 40

Table 4.1. Measured $\langle \tau_{off} \rangle$ values under cytoskeletal disruption, high MCC density, and low temperature..... 38

Figure 5.1. Myosin IIA transiently drives TCR translocation and actin retrograde flow in immunological synapse formation..... 47
Figure 5.2. Inhibition of myosin only affects morphology of the early immunological synapse.....49
Figure 5.3. Physical constraints on TCR microcluster translocation impede myosin IIA movements.....50
Figure 5.4. Inhibition of myosin IIA abolishes intracellular Ca^{2+} influx..... 51
Figure 5.5. Inhibition of myosin IIA reduces phosphorylation of ZAP-70 and colocalization of pZAP-70 with TCR microclusters..... 52
Figure 5.6. Inhibition of myosin IIA reduces phosphorylation of CasL..... 53

Figure 6.1. 63
Figure 6.2. 65
Figure 6.3. Summary of SVD results for three representative cells..... 67
Figure 6.4. Photoactivation in live, antigen-activated T-cells..... 69
Figure 6.5. SVD whole-image analysis of the image sequence from Figure 6.2..... 70

Chapter 1

Introduction: modulation of T-cell signaling by the actin cytoskeleton

*The work presented in this chapter is currently under review as part of the following paper: Yu, Y., Smoligovets, A.A., and Groves, J.T. Modulation of T cell signaling by the actin cytoskeleton. *J. Cell Science,* (2013).

*Alexander Smoligovets initially wrote sections 1.2, 1.3, and parts of 1.1, while Yan Yu wrote the remainder of the manuscript. Yan Yu then integrated the individual sections into the overall manuscript. Both authors edited the manuscript prior to final revisions and submission by Yan Yu.

1.1 Introduction

T cells play a central role in adaptive immunity. To perform their immune functions, T cells must engage pathogen-derived peptides on the surfaces of antigen-presenting cells (APCs) and transduce the extracellular stimuli into specific immune responses via many tightly-coordinated signaling processes on multiple time and length scales. A crawling T cell constantly scans the surfaces of APCs in search of antigen peptides bound to major histocompatibility complex proteins (pMHCs). Upon recognition of such peptides, T cell receptors (TCRs) rapidly assemble into microclusters of tens to hundreds of molecules. Concurrently, other signaling kinases such as Zap70[1,2] and Lck[3], adaptor proteins such as Lat[4] and SLP76[5], and actin polymerizing factors such as WASP, WAVE2, and mDIA1[6,7], are recruited to the macromolecular signaling complexes for signal initiation and amplification (Figure 1.1A). As the T cell spreads to form the tight membrane junction known as the immunological synapse, TCR microclusters are continuously generated at the cell periphery and subsequently translocated to the center of the synapse, forming the central supramolecular activating complex (cSMAC), while integrins and other proteins reorganize into a ring structure in the cell periphery. The signaling events necessary for proper immunological synapse formation must be regulated tightly in time and space to achieve proper T cell activation, and are each dependent on the actin cytoskeleton.

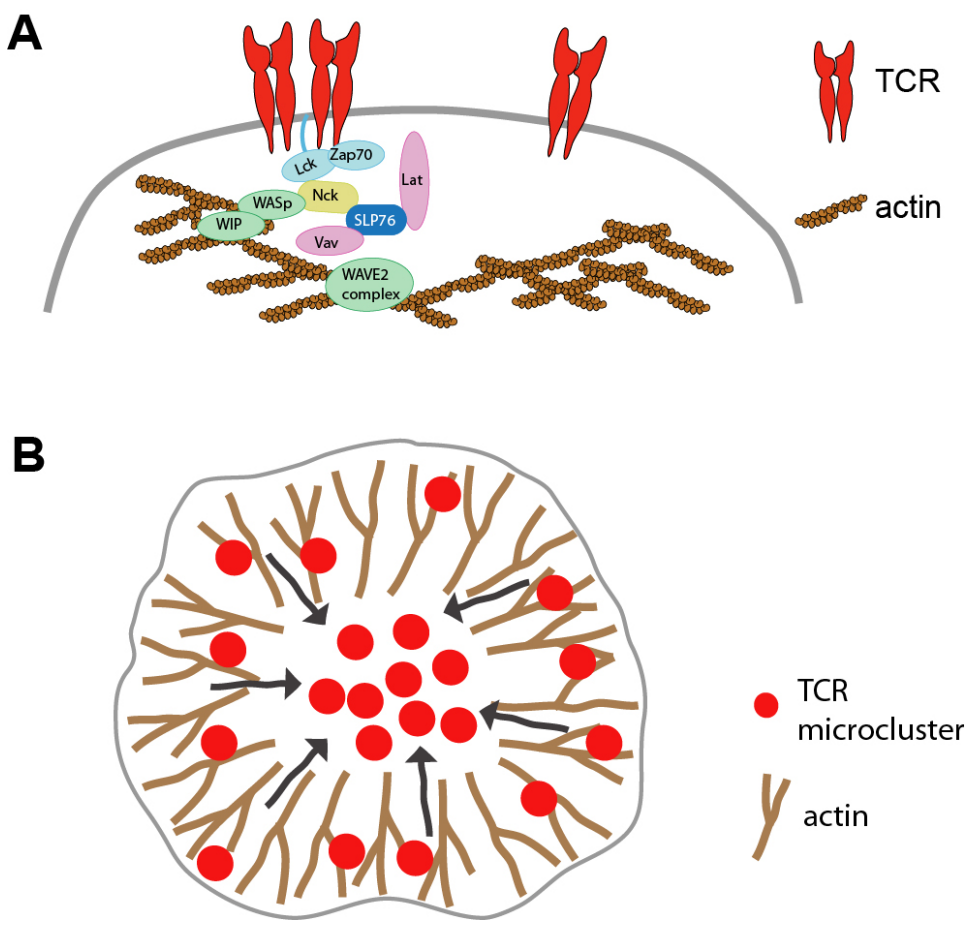


Figure 1.1. The actin cytoskeleton scaffolds signaling cluster assembly and drives the centripetal translocation of T cell receptor (TCR) microclusters during T cell activation. (**A**) During signal initiation, TCRs rapidly assemble into microclusters that subsequently recruit signaling kinases such as Zap70 and Lck, adaptor proteins such as Lat and SLP76, and actin polymerizing factors such as WASp and WAVE2. (**B**) Later in the process of T cell activation, TCR microclusters are transported by actin retrograde flow into the center of the immunological synapse, where actin is depleted.

The actin cytoskeleton is a filamentous network that has been known to provide the mechanical forces for cell polarization and motility, to scaffold proteins for binding and assembly, and also to transport biomolecules. Since the discovery that the polarization of the cytoskeletal is necessary for lymphocyte activation[8,9], studies in the past decades have established the key role of the actin cytoskeleton in T cell activation[6,10–13]. While a substantial amount of knowledge has come from studies using genetic mutation of actin regulatory proteins or biochemical assays such as co-immunoprecipitation, the recent advancement of experimental strategies, from imaging techniques to the incorporation of nanotechnology, has allowed us to understand the role of actin in T cell signaling from a new perspective. In particular, spatial and temporal information about T cell activation can now be obtained by imaging and tracking actin and membrane receptors at the hybrid live T cell-supported membrane interface. Using supported lipid bilayers to mimic the APC surfaces allows direct manipulation of the structure and composition of the artificial membrane, leading to a series of recent investigations on actin in T cell activation[14–21]. An emerging picture is that the dynamic actin cytoskeleton provides the framework for tight regulation of both mechanical and biochemical signaling pathways in T cell activation. This chapter focuses on recent studies that have provided new insights into how the actin cytoskeleton and molecular motors regulate T cell activation, including TCR triggering, signaling protein assembly and translocation, formation of the immunological synapse, and receptor internalization.

1.2 Actin in T cell receptor triggering

Actin polymerization begins rapidly at the site of TCR ligation and accelerates in the cell periphery. Meanwhile, it depolymerizes near the cSMAC boundary, resulting in a retrograde actin flow centripetally. The indispensable role of actin in T cell receptor (TCR) activation has long been recognized and supported by numerous observations that disruption of actin by pharmacological reagents abrogates TCR triggering[22–24]. But what is the exact physical coupling between TCRs and the actin cytoskeleton? What are the mechanisms by which actin modulates TCR triggering? To the best of our knowledge, only one study so far has suggested that the TCR zeta-chain, once tyrosine-phosphorylated, becomes physically associated with the actin cytoskeleton[25]. This conclusion was based on the experimental observation that the association of the TCR-zeta chain with a detergent-insoluble fraction was disrupted by the actin destabilizing agent, cytoshalasin D. More studies have instead demonstrated an indirect coupling between TCR and actin via components of TCR microclusters including Vav1, and adaptor proteins such as SLP76 and Nck[10,26–30]. In either case, there is likely a physical pathway, direct or indirect, to transduce forces between the actin cytoskeleton and TCRs. Several mechanisms have been proposed regarding how actin facilitates TCR triggering, among which one central hypothesis is the conformational change model[31,32]. It was proposed that TCR conformational changes induced by mechanical forces from actin or other sources may trigger T cell signaling, thus making TCRs themselves to act as mechanosensors. The hypothesis is supported by several experimental observations of T cell activation triggered by physical forces[31,33–35]. Using anti-CD3 antibody-coated beads, Kim et al. demonstrated T cell activation induced by a

50 pN force applied by optical tweezers. Interestingly, even though larger forces were also applied normally to the T cell surface, only tangential forces induced T cell activation as confirmed by calcium flux. Therefore, the authors suggested that TCR mechanosensing is direction-specific[33]. Consistent with this interpretation, T cell activation was shown in a recent study to correlate with the docking orientation of pMHC instead of the TCR-pMHC binding affinity[36]. Force-induced T cell activation was also observed by Li et al., although there was no clear direction dependence of the stimulatory force: both parallel shear force and perpendicular pulling force triggered T cell activation[34]. The receptor-deformation model is intriguing, because the proposed mechanism not only explains the role of actin in TCR triggering, but also seems to fit well with some experimental observations in costimulation of T cell activation. For example, CD28 costimulation promotes actin polymerization[37]. Based on the receptor-deformation model, the generation of forces in the actin cytoskeleton due to costimulation may enhance TCR triggering, and thus lower the threshold of T cell activation. The same argument may also be made to explain why integrin signaling costimulates T cell activation. In fact, the Saito group has observed that an actin 'cloud' is initiated at T cell-APC contacts without antigen triggering and it lowers the threshold for activation in subsequent APC encounters[15].

If cytoskeleton-generated strain triggers TCR signaling, the same strain could also be expected to influence TCR-pMHC interactions[31]. By measuring two-dimensional TCR-pMHC binding kinetics using single molecule FRET between a TCR and its interacting antigen peptide, the Davis group demonstrated that disruption of actin significantly prolongs TCR-pMHC associations[38], suggesting that forces from the actin cytoskeleton destabilize TCR interactions. The effect of the cytoskeleton on TCR-pMHC interactions was also independently observed by researchers in the Zhu group, who used a micropipette and a biomembrane force probe to measure bond formation between a T cell and an antigen-presenting red blood cell brought into close proximity. In their study, TCR-pMHC affinity decreased in response to actin disruption[39]. The results from these two studies are not contradictory, because they emphasized different parameters of the TCR-pMHC interaction, and both are evidence that actin cytoskeleton may regulate T cell responsiveness by influencing intrinsic TCR-pMHC binding. Overall, more studies are supporting the hypothesis that forces from actin are involved in TCR triggering via conformational changes, but there has been no direct experimental evidence to demonstrate the structural changes of TCRs upon physical forces. Many questions also are unsolved, such as how this receptor-deformation model is related with the requirement of forming microclusters for TCR signaling.

1.3 Actin in microcluster assembly

Immediately after triggering, T cell receptors assemble into microclusters of tens to hundreds of molecules, where signaling persists. It has been well established that the actin cytoskeleton is necessary for TCR clustering, as microclusters fail to form when the cytoskeleton is disrupted[23]. The challenging question, however, is to understand the nature of actin's involvement in the assembly of TCR microclusters. Actin may facilitate the assembly of signaling molecules by serving as a dynamic scaffold to rapidly transport TCR cofactors (Figure 1.1A, B). By imaging protein assembly at the live T cell-

supported membrane interface during T cell activation, signaling proteins including Lck, Zap70, SLP76, and Lat have been observed to assemble into TCR microclusters within seconds following the initial TCR-pMHC ligation[40]. On the same time scale, TCR triggering also leads to recruitment of cytoskeleton regulatory proteins, such as Vav1, WASp, Cdc42, and Nck, to the site of TCR engagement and then actin polymerization occurs rapidly[10]. Vav1, a key protein for actin remodeling, was found to link the clusters to the actin network[26–30]. An interesting observation from the study by Miletic et al. was that even though Vav1 is a guanine nucleotide exchange factor (GEF), its intrinsic GEF activity is not its sole contribution to TCR signaling. Instead, by integrating TCRs to the actin network, Vav1 seems to promote the scaffolding effects of actin on microcluster assembly and signaling[29]. An alternative mechanism regarding the role of actin in the assembly of microclusters is best described by the picket fence model of diffusion restriction[41]. This model posits that the high local density of actin and actin-associated membrane proteins restricts diffusion of other membrane-associated or membrane-proximal cytoplasmic proteins and thus promotes microcluster assembly. Consistent with this model, actin islands and ERM protein 'pickets' have been observed to strongly determine BCR diffusion in B cells[42,43]. In basophils, the diffusion of the high affinity IgE receptor (FcεRI) also exhibits similar actin dependence[44].

Once microclusters are assembled, they become self-stabilized and can survive actin disruption[24]. Moreover, a recent study has also suggested that microclusters possess the capacity to locally template the actin cytoskeleton around themselves[18]. A unique platform for this study is the patterned supported membrane (Figure 1.2A). Supported lipid bilayers form on glass substrates with uniform metal grid patterns, which hinder TCR cluster transport but do not prevent the cluster formation. When the movement of TCRs is blocked by the physical barrier, actin slows down at sites of physically constrained TCR clusters and transiently enriches at these sites (Figure 1.2B). It is important to note that although the cytoskeleton becomes dispensable to the integrity of fully assembled TCR microclusters, it remains necessary for proper signaling, as disrupting actin results in a rapid reduction of calcium flux even at time points significantly later than the formation of the majority of new TCR microclusters[24].

1.4 Actin in spatial organization of the immunological synapse

In addition to its role in microcluster assembly, the actin cytoskeleton is important for translocating and sorting signaling proteins to form the "bull's eye" pattern in the immunological synapse (Figure 1.2). One characteristic feature of dynamic process is the directed movement of TCR microclusters, which can be readily studied using single-molecule imaging at the hybrid live cell-supported membrane interface and then tracking analysis with approximately 50 nm precision (Figure 1.3). Immediately following binding to pMHCs, TCRs cluster with other signaling proteins such as Lck and are radially transported to the center of the cell-cell junction to form the cSMAC. Simultaneously, ligated integrins and associated proteins also undergo centripetal translocation but eventually accumulate around the periphery of the synapse. When T cells were treated with latrunculin, a drug to block actin polymerization, translocation of TCR microclusters stopped during the movements, indicating that the clusters are transported by the retrograde actin flow[23]. TCR-actin coupling has been confirmed in

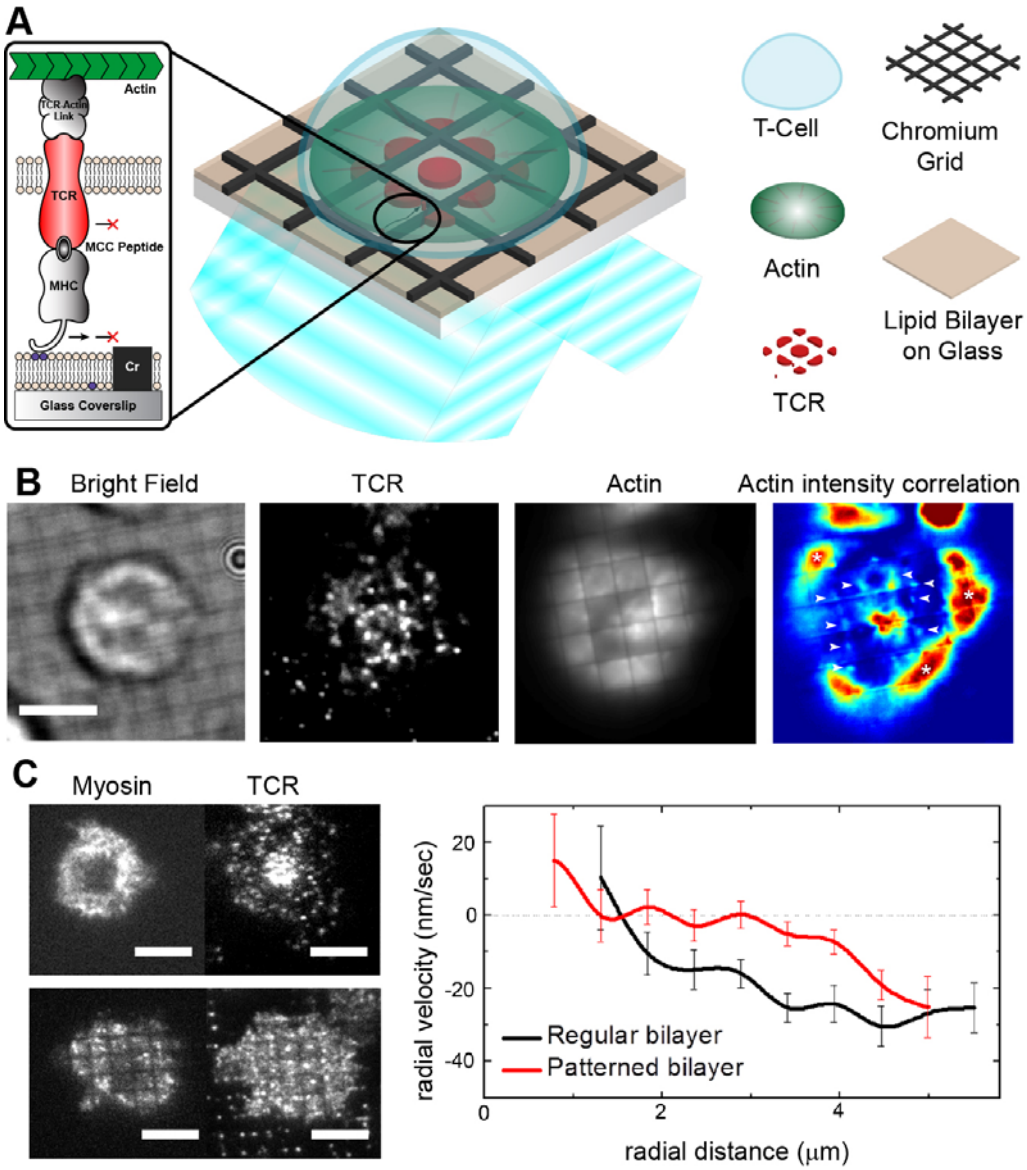


Figure 1.2. The hybrid live cell-nanopatterned supported lipid bilayer platform allows the coupling between TCR microclusters and actin or myosin to be examined. (**A**) Schematic of the experimental setup. T cells interact with a patterned supported lipid bilayer functionalized with the antigen-presenting cell proteins ICAM-1 and pMHC, which allows cells to activate in a controlled, antigen-dependent manner. Bilayer proteins are laterally mobile, but they can be spatially constrained by chromium diffusion barriers nanopatterned onto the glass substrate. (**B**) The nanopatterned supported lipid bilayer platform was used to study actin accumulation at sites of pinned TCR microclusters. Images of a T cell on a nanopatterned supported lipid bilayer show a typical frustrated immunological synapse with TCRs pinned at the corners of the grid pattern by continuous centripetal actin flow. The pixel-by-pixel autocorrelation of the actin fluorescence intensity profile (rightmost panel) shows discrete large-scale intensity fluctuations at areas adjacent to the grids (white arrows). The white asterisks correspond to areas of extension and retraction of the lamellipodia. Color scale: arbitrary; scale bar: 5 μm. (**C**) A mechanical connection exists between TCRs and myosin. TIRF images of T cells on unpatterned and patterned supported lipid bilayers show the different distributions of both TCR microclusters and myosin in unperturbed and frustrated immunological synapses. The centripetal radial velocity (nm/sec) of EGFP-labeled myosin IIA decreases when TCR microclusters encounter diffusion barriers, suggesting a mechanical connection between TCRs and myosin.

several studies in which TCR microclusters, integrins, and the actin cytoskeleton were shown to move in the same direction[14,17,21,45]. Using total internal fluorescence microscopy for single-molecule imaging and subsequent vector-field based tracking algorithms, cluster transport and retrograde actin flow can be quantified in the immunological synapse (Figure 1.3). The observations that TCRs move slower than the underlying retrograde actin flow suggest a frictional "stick-slip" motion of the TCR microclusters on the cytoskeleton during their translocation to the cSMAC[14]. More direct evidence was achieved by using patterned supported membrane surfaces (Figure 1.2A, B)[17,18,45]. When transport of TCR clusters is hindered by metal patterns acting as the physical barrier, actin flow slows down but does not completely stop, as expected for a dynamic coupling between TCRs and actin.

Beyond purely transporting proteins, the frictional coupling between actin and membrane receptors also appears to play an important role in their spatial organization in the immunological synapse formation. A study in which the clustering state of

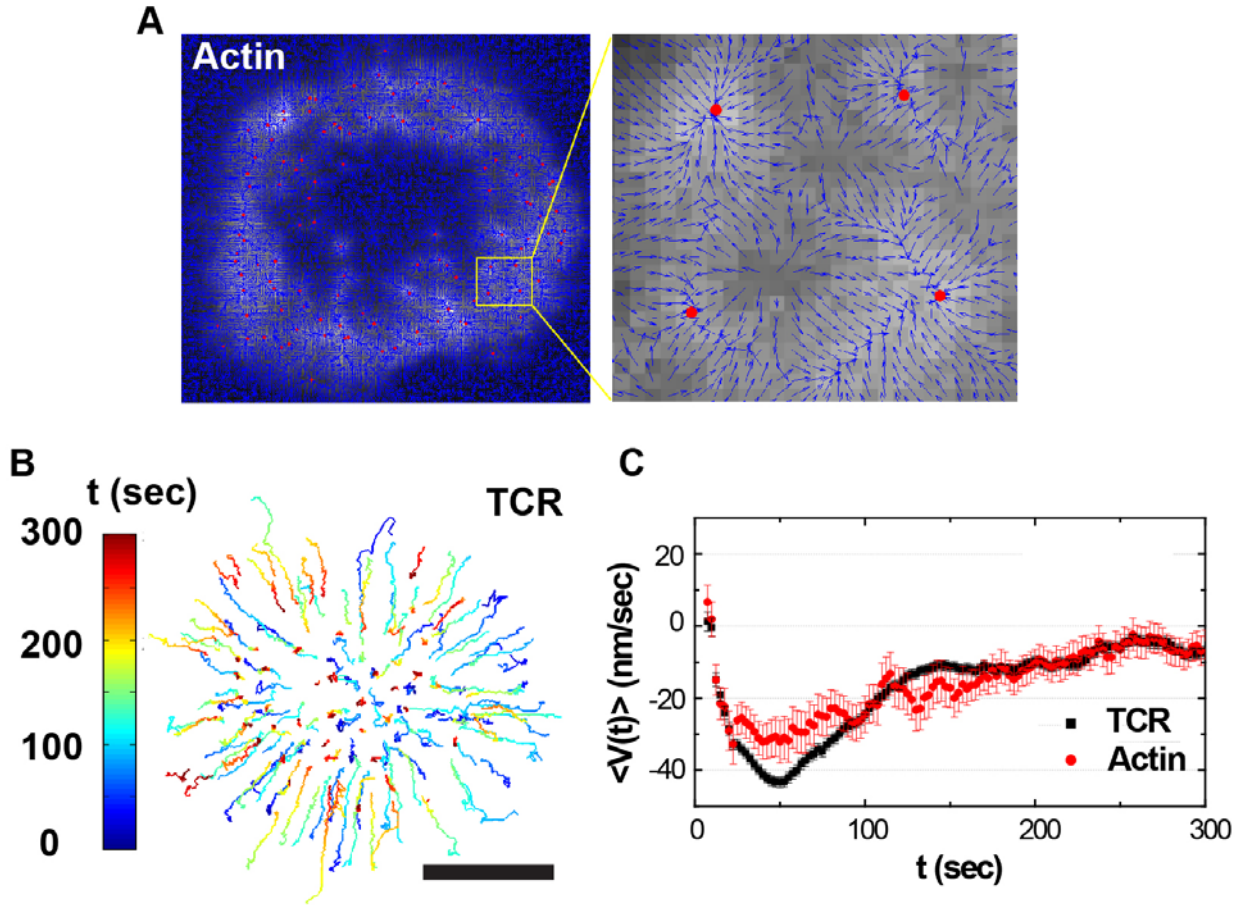


Figure 1.3. Custom particle identification and tracking algorithms reveal the dynamics of TCR microcluster motion and centripetal actin flow. (**A**) A vector-field algorithm identifies actin features (red dots) across the whole immunological synapse. The panel on the right shows individual intensity vectors pointing to four distinguishable features. (**B**) The velocities of TCR microclusters correlate with the time elapsed following immunological synapse formation. All trajectories are color-coded based on the elapsed time following the initial cell-bilayer contact. Scale bar: 5 μm. (**C**) The radial velocities of TCR microclusters and actin retrograde flow identified simultaneously by the vector-field algorithm show how centripetal flow at the immunological synapse changes over time.

lymphocyte function-associated antigen 1 (LFA-1) was experimentally manipulated[46] has provided insight into this phenomenon (Figure 1.4). When LFA-1 cluster size was progressively increased by using bivalent and tetravalent antibody crosslinking of either LFA-1 or its intercellular adhesion molecule 1 (ICAM-1) ligand, larger clusters due to higher degree of crosslinking were observed to be transported closer to the center of the immunological synapse. Tetravalently crosslinked LFA-1 was able to reach the cSMAC region with TCRs, which are otherwise larger than native LFA-1 clusters. This size-dependent protein sorting again supports the frictional coupling between the protein clusters and actin. More importantly, the observation shows that the coupling strength scales with the receptor cluster size and determines the final localization of receptors in the immunological synapse.

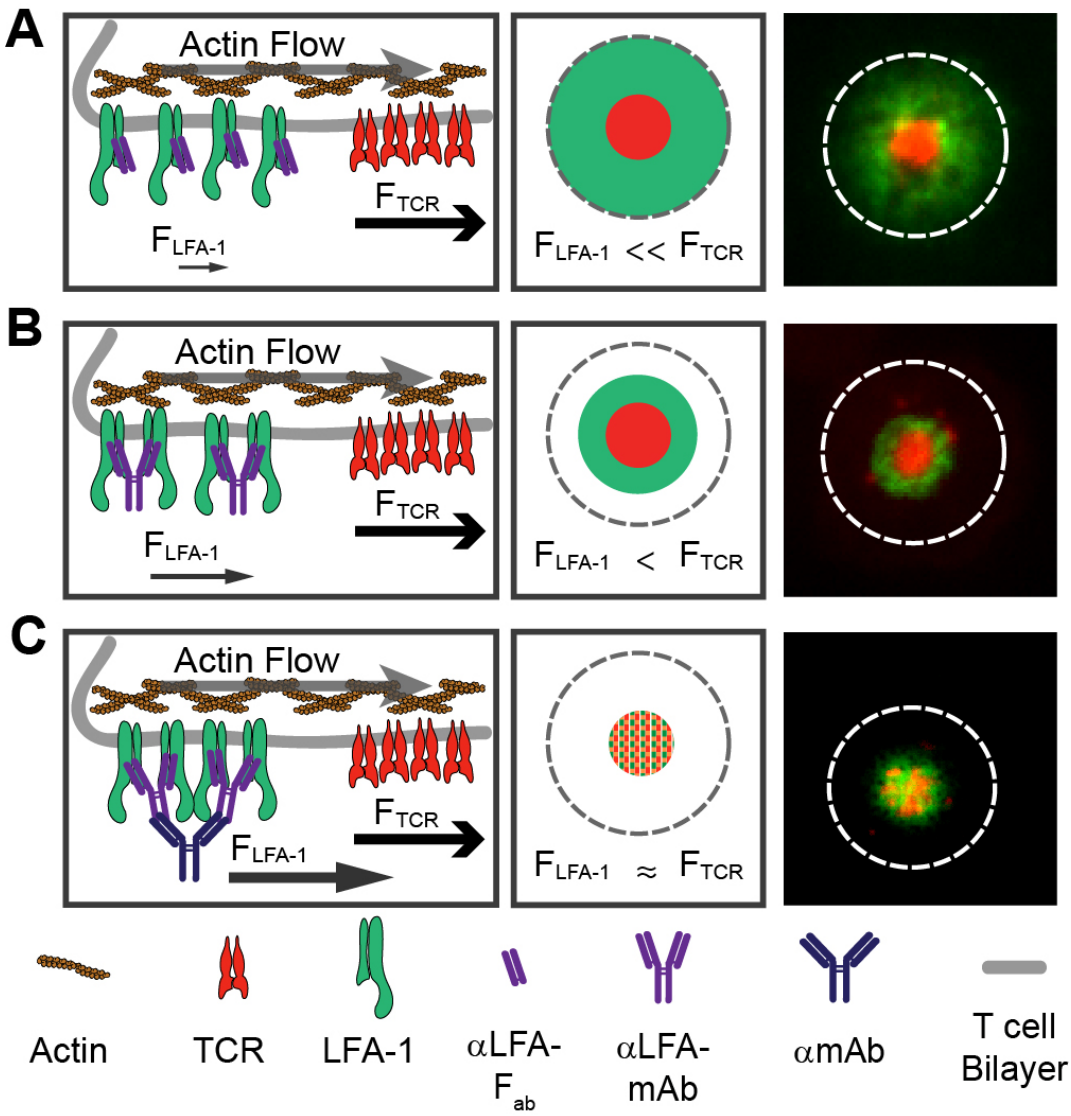


Figure 1.4. The model for size-dependent protein sorting in the immunological synapse. LFA-1 becomes increasingly crosslinked by the addition of monomeric and multimeric primary antibodies, and LFA-1 cluster sizes correspondingly increase. Larger clusters are transported closer to the center of the immunological synapse due to their relatively strong association with the actin cytoskeleton.

Actin-mediated protein sorting may also be a key process for T cells to modulate signaling, considering the longstanding notion that the large-scale protein pattern at the immunological synapse is correlated with T cell activity[47–50]. Most of the early signaling events, such as phosphorylation of the immunoreceptor tyrosine-based activation motifs (ITAMs) by Lck[23], occur in the TCR microclusters prior to or during the centripetal transport[51,52]. Key signaling proteins such as Zap70 and SLP76 are also phosphorylated during that process before being downregulated in the cSMAC[26]. When the centripetal movement of TCR microclusters at the cell periphery was physically blocked by micropatterns in lipid bilayers, those microclusters pinned along the diffusional barrier remained phosphorylated at time points when TCRs at the cSMAC would otherwise be dephosphorylated and inactivated[53]. This suggests that TCR signaling activity is influenced by a microcluster's radial location instead of the absolute time scale of signaling. Therefore, by transporting and differentially sorting signaling microclusters, actin appears to play a key role in ensuring the spatial and temporal connectivity between signaling activities in T cell activation.

1.5 Molecular motors in TCR signaling

Compared to the extensive studies on actin in T cell signaling, there have been fewer studies on the role of molecular motors in the process. The most characterized molecular motors in T lymphocytes are non-muscle myosin IIA and dynein, which are actin-associated and microtubule-associated molecular motors, respectively. Myosin II proteins are a family of ATP-dependent motor proteins that reversibly bind to actin and are known to provide contractile forces in the actin network during a wide spectrum of processes, from muscle contraction to cell motility[54–57]. Non-muscle myosin IIA is the dominantly expressed isoform in T cells[58]. It has been shown to play an important role in T cell polarity and migration[16,59–61]. However, the role of myosin IIA in T cell signaling and immunological synapse formation is less clear. Studies reached contradictory conclusions regarding whether myosin is necessary for TCR microcluster movement and immunological synapse organization[20,21,62–64] or not[19,58,65]. Several recent studies imaged and tracked TCR movement and actin retrograde flow at the cell-lipid bilayer interface in either Jurkat cells or primary T cells[20,21,64]. All three studies independently showed that myosin IIA is important for T cell activation and that both actin polymerization and myosin contraction are the driving forces for the centripetal movement of TCRs during T cell signaling. Myosin drives a rapid inward translocation in the first one to two minutes of signaling, while actin polymerization provides a slower basal rate of motion that persists throughout the entire process[21]. Therefore, inhibition of myosin IIA alone slows down the movement of TCRs, but does not disrupt the "bull's eye" protein pattern at the immunological synapse at much later time points. This suggests that the discrepancy between the earlier studies may have arisen from the different time points at which the immunological synapse morphology was examined. Moreover, a mechanical feedback between TCRs and myosin/actin was also proposed based on the experimental observation that both actin and myosin slowed down when TCR transport was blocked on the patterned lipid bilayers (Figure 1.2C)[21]. However, the Krummel group suggested that myosin is not required for immunological synapse formation[19]. They reported that TCR translocation is dependent on actin

depolymerization instead of myosin and proposes that the contradictory observations may reflect the species-specific roles of motor proteins in human, mouse, and Jurkat T cells.

The role of dynein, the microtubule-associated molecular motor in TCR microcluster translocation and the immunological synapse formation has also been under debate recently[20,66]. In contrast to myosin IIA, which exerts contractile forces in actin filaments, dynein transports intracellular cargos along microtubules. The Saito group reported that inhibition of dynein leads to slower TCR microcluster movement and impaired cSMAC formation in T cells, suggesting an important role of dynein in T cell immunological synapse[66]. However, research by the Hammer group showed that dynein plays a negligible role in TCR transport[20]. The exact role of dynein in T cell activation is to be further explored.

Both myosin IIA and dynein may involve in T cell signaling, but likely in dramatically different ways. Inhibition of myosin IIA diminishes T cell signaling, demonstrated by reduced calcium ion influx and Zap70 phosphorylation[21,63]. Inhibition of dynein, however, leads to enhanced T cell activation[66]. It is possible that myosin-driven TCR transport on actin is required for signaling initiation and the dynein-driven translocation on microtubule is involved in receptor internalization and signal termination in cSMAC. However, the exact mechanisms are not clear. Because molecular motors are unlikely to directly participate in signaling pathways, it is possible that motor proteins such as myosin IIA modulate T cell signaling by transducing intracellular physical forces to biochemical signals. One possible mechanism may involve a mechanosensing protein, CasL (Crk-associated substrate of the lymphocyte type). CasL has been suggested to be sensitive to myosin-generated strain through conformational changes that may lead to enhancement of tyrosine phosphorylation and possible downstream signaling[21,64]. What is not yet clear is how exactly CasL correlates with the actin cytoskeleton or what is its precise role in TCR signaling pathways. Further studies are also necessary to elucidate the exact role of dynein in T cell activation.

1.6 Conclusion

The role of the actin cytoskeleton in T cell activation transcends the maintenance of cell morphology and transport of proteins. An emerging idea is that the physical forces generated by actin and actin-associated proteins modulate T cell activation by influencing biochemical signaling. To uncover the exact mechanisms of signaling regulation by the actin cytoskeleton remains the key as well as the challenge to understanding T cell activation. Tremendous progress has been made in identifying individual molecules linking the complex signaling pathways and cytoskeletal elements through traditional biochemical studies. The most recent breakthroughs in our understanding of T cell signaling, however, showcase that understanding the integration of those mechanical and biochemical components requires development of novel interdisciplinary approaches, from high-resolution imaging techniques to sophisticated nanofabrication. We expect that new aspects of actin's contribution in T cell signaling will be revealed with multidisciplinary approaches, such as surface nanopatterning techniques and super-resolution imaging.

Chapter 2

Characterization of dynamic actin associations with T-cell receptor microclusters in primary T cells

*The work presented in this chapter has been previously published as part of the following paper: Smoligovets, A.A., Smith, A.W., Wu, H.-J., Petit, R.S., and Groves, J.T. Characterization of Dynamic Actin Associations with T-cell Receptor Microclusters in Primary T-cells. *J. Cell Science*, 125, 735-42 (2012).

*Alexander Smoligovets conceived the experiments, prepared necessary materials and reagents, performed the experiments, interpreted the data, and wrote the manuscript. Adam Smith performed the bulk of the microscopy during the experiments, developed and applied the autocorrelation data analysis algorithm, and edited the manuscript. Hung-Jen Wu developed and applied the vector field identification and tracking algorithms. Rebecca Petit nanofabricated the patterned glass substrates.

2.1 Introduction

T cells are activated when their T-cell antigen receptors (TCRs) are triggered by interactions with antigen peptide–major histocompatibility complex (pMHC) proteins on antigen-presenting cell (APC) surfaces. T cells exhibit exquisite selectivity and sensitivity, and the physical basis for these attributes within the TCR signaling system has attracted much interest. A significant aspect of TCR triggering is the spatial assembly of receptors on multiple length scales. At the scale of the cell itself, TCRs are visibly transported towards the center of the T-cell–APC interface, and the resulting spatial patterns of TCRs and other molecules are called the immunological synapse[67,68]. Physically interfering with these transport processes can induce detectable changes in T cell signaling, such as phosphorylation of immunoreceptor tyrosine-based activation motifs on the TCR complex and intracellular calcium flux[53]. On shorter time and length scales, TCRs form microclusters upon engagement with pMHC[26,69,70]. Much of the relevant signaling activity takes place within these TCR microclusters, which function as integrated signaling machines.

Underlying the spatial assembly and transport of TCRs during T cell activation are interactions between the receptors and the actin cytoskeleton[6,10,45]. In response to TCR triggering, the cytoskeleton transitions from a crawling morphology to a pattern of centripetal flow[9,14,71,72]. Simultaneously, TCR microclusters coalesce and translocate towards the center of the immunological synapse. Both coalescence and translocation are actin-dependent, as disruption of the cytoskeleton with latrunculin prevents both processes[23,24]. Additionally, recent work has shown that actin can affect local TCR–pMHC binding kinetics[38,39], illustrating another mechanism for involvement of the cytoskeleton in signaling.

TCR microclusters need not move at the same speed as the retrograde flowing actin[14,17], nor do they need to move in the same direction. When translocating microclusters encounter physical obstacles imposed using patterned supported membrane substrates, the microclusters are deflected and move at angles to the actin flow with speeds that exhibit a cosine scaling law, which is consistent with dissipative, or frictional, actin-coupling mechanisms[45]. In other words, numerous weak interactions sum to yield a net force on the TCR microcluster, but there appears to be no stable or elastic association with the actin network. Such frictional coupling mechanisms appear to extend beyond TCR in the immunological synapse. Differentially clustering the integrin lymphocyte function-associated antigen 1 (LFA-1) using antibodies has been shown to redirect this protein to different positions within the synapse, with the most highly clustered LFA-1 ending up in the center along with TCRs[46].

Although a significant role for actin in the immunological synapse is clear, many physical aspects of actin–TCR interactions are still relegated to the imagination. Preliminary observations of actin engaged in such interactions have been made in Jurkat cells[14,17], but although these are a tractable T-cell-based model system, they have important differences from primary T cells[73–75]. Because their TCR agonist is not known, Jurkat cells must be triggered through artificial antibody-induced crosslinking of their CD3 receptors, which inherently supplants endogenous TCR–TCR associations and has the potential to overstabilize the microcluster. This might add to already-documented differences in membrane protein organization between Jurkat cells and

primary T cells[73]. Furthermore, a number of Jurkat cell proteins exhibit levels of phosphorylation unlike those of their primary T cell counterparts, including known actin regulatory molecules such as Pyk2 and Vav1[74]. These differences raise questions about findings from studies based on Jurkat cell studies and necessitate the ultimate characterization of actin cytoskeleton behavior in primary cells.

In this study, we quantitatively characterized cortical actin motion within antigen-triggered primary T cells to obtain a deeper level of understanding of the elaborate interactions between the cytoskeleton and the plasma membrane during T-cell activation. We employed the hybrid live cell–nanopatterned supported lipid bilayer system, which allows both for assembly of TCR microclusters through interactions with laterally mobile, membrane-tethered pMHC and control of the lateral mobility of these microclusters with nanopatterned barriers in the substrate[47,53,76]. Analysis was performed using vector-field identification and tracking algorithms to characterize actin lateral movement and image time-autocorrelation to extract dynamic fluctuations. We observed that the actin cytoskeleton responds to laterally confined TCR clusters by slowing down in their vicinity, a result consistent with a previous report utilizing Jurkat T cells[17], and that the slowing is direction-dependent with respect to the resistance against TCR motion. Image time-autocorrelation revealed that the entire actin assembly forms and disassembles *en masse*. From this observation, we postulate that the primary stability of TCR microclusters originates from the receptors themselves, or other molecules in the microcluster, and that this stability templates assembly of the more dynamic actin, ultimately leading to a linkage to the bulk cytoskeleton.

2.2 Materials and methods

2.2.1 DNA constructs

A plasmid containing EGFP fused to the calponin homology domain of utrophin (EGFP–UtrCH) was a gift of William Bement, University of Wisconsin, Madison, WI[77]. The EGFP–UtrCH gene was amplified using PCR and subcloned into a murine stem cell virus parent-vector-containing puromycin *N*-acetyltransferase expressed from an internal ribosome entry site (pMSCV-Puro) as previously described[78]. A retroviral-vector-containing EGFP–β-actin was similarly produced by subcloning the gene from an EGFP–β-actin-containing pCDNA3 vector[79].

2.2.2 Retroviral transduction of T cells

AND CD4+ T cells[80] were harvested and retrovirally transduced as previously described[78]. Briefly, retrovirus-containing cell medium was harvested from cultures of Phoenix retroviral packaging cells transfected with pMSCV-Puro containing the gene of interest. The medium was used to transduce CD4+ T cells isolated from the lymph nodes and spleens of AND × B10.BR mice, primed with 2 μM moth cytochrome *c* (amino acids 88–103) and stimulated with 50 U/ml of interleukin-2 (IL-2). T cells were transduced 48 and/or 72 hours after isolation, selected using 0.5 μg/ml puromycin from 78 to 120 hours after isolation and used in experiments 168 hours after isolation.

2.2.3 Preparation of T cells for imaging

Imaging experiments were performed as previously described[78]. Briefly, supported lipid bilayers containing 2 mol% Ni^{2+}-DOGS and 98 mol% DOPC (Avanti Polar Lipids, Alabaster, AL) were formed within FCS2 Closed Chamber Systems (flow cells; Bioptechs, Butler, PA) on piranha-etched glass coverslips or patterned chromium substrates nanofabricated using electron beam lithography as previously described (Salaita et al., 2010). The bilayers were functionalized with polyhistidine-tagged MHC loaded with moth cytochrome *c* (amino acids 88–103) and with polyhistidine-tagged ICAM-1 proteins, and the flow cells were brought to 37°C. T cells were rinsed with a previously described imaging buffer[78], pelleted, resuspended in a solution of 5 µl Alexa-Fluor-568- or -647-labeled H57 anti-TCR antibody fragment (Fab) diluted in 100 µl imaging buffer and incubated on ice for 20 minutes. Cells were then rinsed with imaging buffer, pelleted, resuspended in pre-warmed imaging buffer and injected into flow cells. The flow cells were kept at 37°C throughout the experiments and all images were acquired within 120 minutes of the injection of the cells.

2.2.4 Microscopy

Cell imaging was performed on an inverted microscope (Nikon Eclipse Ti; Technical Instruments, Burlingame, CA). TIRF microscopy was done using a fiber-coupled Nikon TIRF illuminator with a custom-built laser source (Smith et al., 2011). The 647 nm (RCL-050-640; Crystalaser, Reno, NV), 561 nm (GCL-100-561; Crystalaser, Reno, NV) and 488 nm (Sapphire HP; Coherent, Santa Clara, CA) asers were launched into a single-mode fiber that was connected to the TIRF illuminator. Excitation powers at the sample were on the order of 1 kW/cm^2. Images were acquired with an Orca-R2 digital camera (C10600-10B; Hamamatsu Photonics K.K., Japan).

2.2.5 Actin motion analysis

To analyze the motion of the actin cytoskeleton, we developed a set of algorithms for identifying and tracking visibly mobile fluctuations in actin and/or probe density and implemented them in MatLab. Features in the actin distribution are first identified using a supplemented image gradient approach. Each frame of an actin time-lapse recording is convolved with a Gaussian filter to remove low-level imaging noise, and local maxima in the fluorescence intensity image are used to identify candidate features. Because individual features often contain multiple fluorescence intensity maxima, vector fields are created based on fluorescence intensity gradients within the image, and features are assigned locations by positions with converging vectors, which correspond to low local intensity variations. The vector fields also overcome uneven levels of fluorescence across the cell, thus allowing features to be identified consistently in spite of subcellular variations in cytoskeletal density or illumination[81].

Following identification, nearest neighbor features in consecutive frames are linked to generate actin trajectories as previously described[17]. Briefly, linking is performed only on features that are visible in consecutive frames within 5 pixels (0.315 µm) of each other. The appearances and disappearances of features are monitored

such that if a feature is present in frame *t* and has no identifiable nearest neighbor in frame *t*+1, it is defined as disappearing after frame *t*. Mergers and splits of features are also monitored.

The trajectories of actin features are evaluated using an algorithm that determines the time it takes each feature to move a certain distance. We refer to this time as the 'escape time' (τ) to signify that there is no directional bias to the algorithm, and the selected 'escape distance' (*r*=3 pixels=0.189 μm) thus defines a circular boundary around the feature. Note that although the escape distance is below the Rayleigh diffraction limit, it is still possible to localize maxima in the light field with high precision. Our approach is based on centroid analyses used in single molecule localization algorithms[82,83] except that we are tracking inhomogeneities in the fluorophore density field rather than single objects. This is fundamentally analogous to single fluorophore position identification in standard super-resolution optical techniques such as photoactivated localization microscopy[84] and stochastic optical reconstruction microscopy[85]. Escape times are determined iteratively for each frame in which a given feature is identified. They are not recorded when a feature disappears before exceeding the escape distance.

2.2.6 Image time-autocorrelation analysis

The time-autocorrelation function of the fluctuating fluorescence intensity was calculated on a pixel-by-pixel basis using the time-lapse image stacks. The time-dependent intensity of each pixel is designated at $I_{x,y}(t)$, where the *x* and *y* subscripts refer to the pixel position. The correlation function was calculated using the fluctuations of the intensity away from time-averaged value:

$$\delta I_{x,y}(t) = I_{x,y}(t) - \left\langle I_{x,y}(t) \right\rangle$$

where

$$\left\langle I_{x,y}(t) \right\rangle = \frac{1}{T}\int_0^T I_{x,y}(t)dt$$

.

The pixel-by-pixel time-autocorrelation function is then calculated as:

$$G_{x,y}(\tau) = \frac{\left\langle \delta I_{x,y}(t) \cdot \delta I_{x,y}(t+\tau) \right\rangle}{\left\langle I_{x,y}(t) \right\rangle^2}.$$

2.3 Results

2.3.1 Immunological synapse formation on supported lipid bilayers and nanopatterned substrates

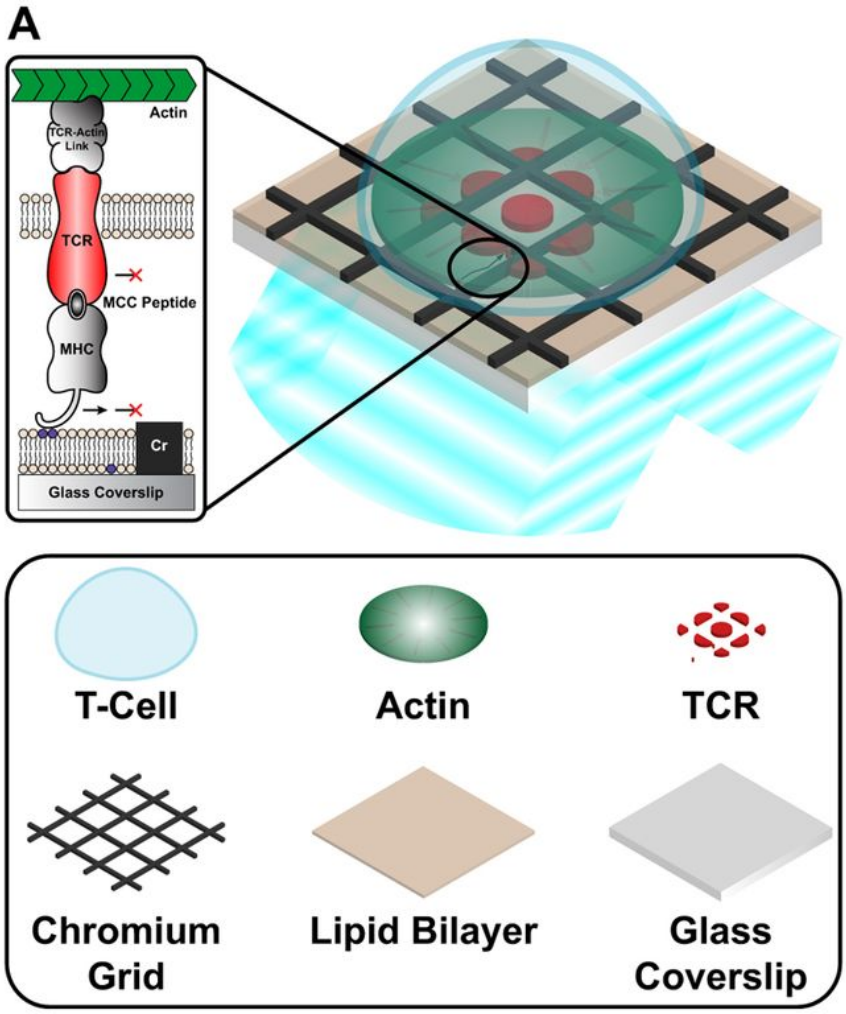


Figure 2.1. The supported lipid bilayer allows visualization of the T cell cortical actin cytoskeleton during immunological synapse formation. (**A**) Schematic outline of the experiment. T cells interact with a supported lipid bilayer functionalized with APC proteins. Centripetal flow of the actin cytoskeleton causes TCR microclusters to coalesce and translocate until they reach a chromium barrier (Cr), where they accumulate. The ICAM-1 APC protein (not shown) is also included and interacts with T cell LFA-1. Ni^{2+}-DOGS lipids (purple circles) and the TIRF illumination beam (cyan) are not labeled. (**B–G**) TIRF microscopy images of TCRs, the actin cytoskeleton and ICAM-1, as well as bright field and reflection interference contrast microscopy (RICM) images of a cell on a grid-patterned substrate show a typical frustrated immunological synapse. Scale bar: 5 μm.

We visualized the cortical actin cytoskeleton in primary murine T cells during immunological synapse formation by allowing primed T cells to interact with a supported lipid bilayer functionalized with pMHC and intercellular adhesion molecule 1 (ICAM-1) proteins (Figure 2.1A). This well-established system simulates the APC surface and effectively triggers T cells while allowing the use of total internal reflection fluorescence (TIRF) microscopy to image events within hundreds of nanometers of the cell–bilayer interface[86–88]. An actin-binding probe composed of enhanced green fluorescent protein (EGFP) bound to the calponin homology domain of utrophin (EGFP–UtrCH) enabled observation of F-actin dynamics[77], and key observations made with EGFP–UtrCH were validated using EGFP–β-actin.

Experiments in which the spatial configuration of the immunological synapse is physically altered with nanopatterned substrates have proven informative in a variety of studies[47,86]. Substrates patterned with grids of continuous metal lines (typically ~100 nm line width, ~10 nm height and 2-5 μm spacing) block diffusive transport of lipids, bilayer-associated protein ligands and their cognate receptors on the plasma membrane between isolated corrals, but they do not impose any effect on lateral diffusion within each corral[47,53,76,89,90]. Thus, when T cells interact with a protein-functionalized supported lipid bilayer on a nanopatterned substrate, TCR–pMHC microclusters and LFA-1–ICAM-1 assemblies form properly but cannot move outside the corral boundaries. Discontinuous barriers (crosses) that permit lateral diffusion of lipids and bilayer proteins serve as a control for nonspecific interactions of the cell with the metal barrier material. This system reliably reproduces the classic Kupferian synapse in T cells (Figure 2.1B–G).

2.3.2 Analysis of cortical actin flow in primary T cells

One effective way of imaging the movement of the actin cytoskeleton is fluorescence speckle microscopy (FSM)[91]. In this methodology, fluorescent probes are incorporated sparsely into the actin cytoskeleton, and intrinsic density fluctuations in their random distribution provide features, or ‘speckles’, whose movement can be tracked. FSM generally does not involve actual imaging of individual fluorophores, though this is possible with modern methods. Stochastic density fluctuations are readily discernable for up to ten fluorophores per diffraction spot. As such, coordinated translational movement of feature patterns mirrors bulk cytoskeletal flow, whereas time evolution of the translating pattern reflects dynamic redistribution of the monomers.

In the experiments described here, we performed FSM using relatively high fluorescent probe densities. This enables better mapping of actual actin density fluctuations (as opposed to stochastic labeling fluctuations) but also requires more sophisticated image analysis. At very low probe densities, speckle features tend to have simpler shapes than they do at higher density. Thus, simple particle tracking algorithms are easily foiled by the complex patterns seen in highly labeled cells. To improve tracking accuracy in these systems, we developed a set of algorithms (see Materials and Methods) that identify features in images based on shape-independent gradient tracking, link them across multiple frames and evaluate their motion. The vector-field algorithm that we employed is a modification of those commonly used in medical imaging applications[81], which isolate endpoints in the fluorescence intensity gradient of

an image as shown in Figure 2.2A–C. This method overcomes the tendency of raster-based algorithms to identify multiple false centers in features based on their multiple local fluorescence intensity maxima. Features are then tracked across consecutive frames using a modified nearest-neighbor approach (Fig. 2.2B,C).

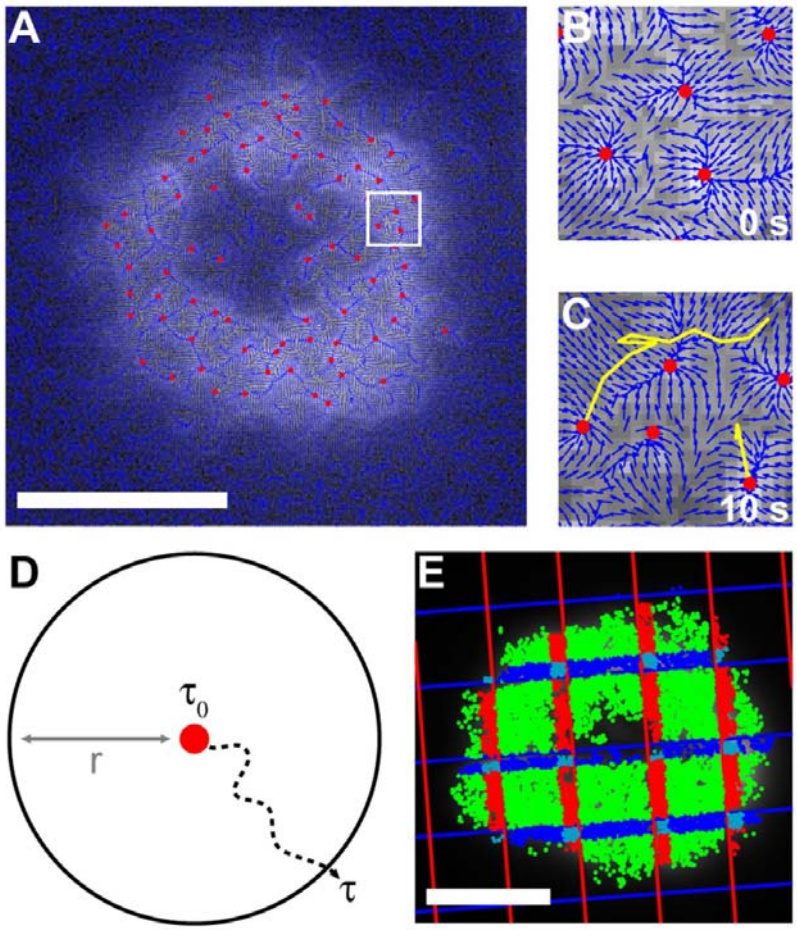


Figure 2.2. Analysis methods for bulk cytoskeletal flow are distinct from those used to describe speckle motion. (**A**) A vector-field algorithm identifies the centers of actin features across a whole cell. (**B,C**) The white square in A is enlarged to clearly show individual vectors in the vector field, and actin features are tracked across multiple frames. New features without tracks are also visible in C. (**D**) Schematic of the escape time analysis. The time it takes for a feature to travel further than a given escape distance (*r*) in any direction is its escape time (τ). (**E**) Escape times are distributed into populations based on each feature's instantaneous position. For example, features within 0.63 μm (10 pixels) of a single pattern boundary and on the opposite side from the cell center are colored dark blue or red, those within 0.63 μm of two boundaries are colored light blue and all other features are colored green. Scale bars: 5 μm.

The most common parameter used for evaluating moving objects is velocity. Although this parameter has been used effectively to describe speckle motion, we found that imaging of the cytoskeleton through an opaque chromium pattern displaced the identified centers of actin features near pattern boundaries and impacted both their apparent speed and direction of travel. We therefore evaluated actin motion in terms of the time it took a feature to travel a certain distance, here referred to as the 'escape time' (τ) and the 'escape distance' (*r*) (Figure 2.2D). This analysis method, which is demonstrated in the associated manuscript[18] and explained in detail in the Materials and Methods section, is effectively a determination of mean square displacement, except that the output is in the form of time per (unit distance)^2 instead of the inverse. The escape time analysis is not biased by the direction of motion and demonstrably avoids the optical artifacts mentioned above. To test the effects of imaging artifacts, image stacks from cells on unpatterned substrates were overlaid with grid shadow images prior to analysis to simulate the appearance of cells on actual patterned substrates. The escape times in these cells showed no dependence on proximity to

pattern boundaries (supplementary material Figure S6 in the associated manuscript[18]). Escape times were also similar between cells expressing EGFP–UtrCH and EGFP–β-actin (supplementary material Figure S7 in the associated manuscript[18]).

The primary purpose of the grid experiments was to pin the position of TCR microclusters so that changes in actin movement and fluctuations at these microclusters could be analyzed. Such analysis required binning the escape times of features based on spatial distribution (e.g. Figure 2.2E). Escape times were also normalized within each cell to facilitate comparison between different cells in a population, even in the presence of cell-to-cell variability. This normalization allowed statistically robust quantitative data sets to be assembled.

2.3.3 Resistance-dependent slowing of actin at sites of TCR clusters

In the following studies, T cells were allowed to form immunological synapses on substrates nanopatterned with metal grids. Grid barriers effectively trap TCR microclusters, pinning them in place for extended periods of time without otherwise interfering with their assembly. In cells that formed synapses on the edge of a patterned region, large bands of clustered TCR were visible at the pattern boundary. In these partially patterned cells, it was possible to compare escape times of features in regions with and without clustered TCRs that were approximately equidistant from the cell center (Figure 2.3A). As anticipated, escape times in a region corresponding to clustered TCRs were higher than those in a region lacking TCRs (Figure 2.3B). This can be interpreted as the result of slowing down or of concentration of actin in the immediate

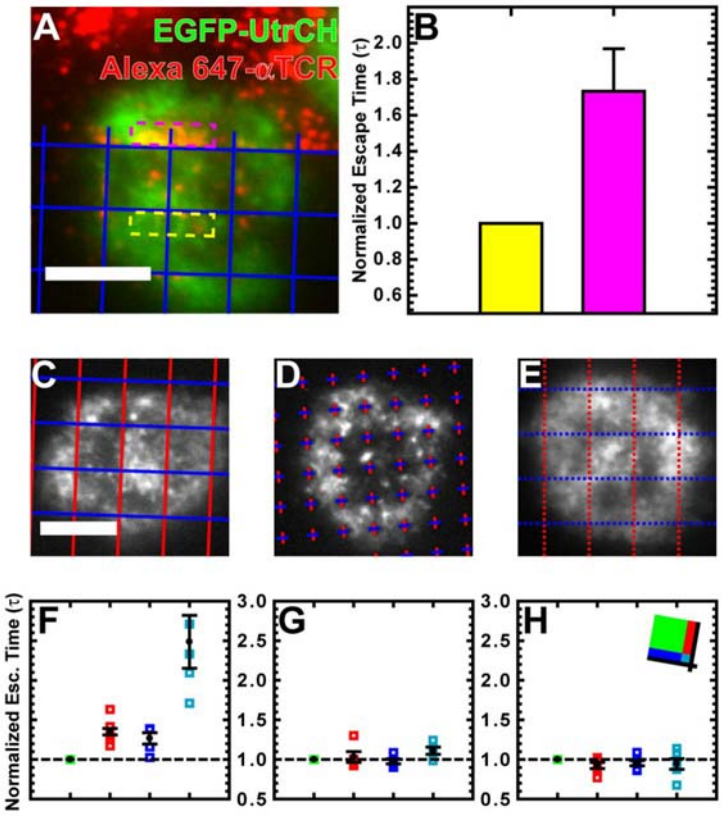


Figure 2.3. Actin features slow down in TCR-rich regions. (**A,B**) Two regions of a cell partially on a grid-patterned supported lipid bilayer equidistant from the cell center were selected (yellow and purple rectangles in **A**) for analysis of actin escape times (**B**). (**C–E**) Representative frames from time lapses show cells interacting with a grid-patterned substrate (**C**), a cross-patterned substrate (**D**) or an unpatterned substrate overlaid with the grid used for analysis (**E**). (**F–H**) Actin features from the cells in **C–E** were partitioned into four populations and analyzed for escape times. The inset shows that the green population is composed of all steps occurring further than 0.63 μm (10 pixels) from the outside edge of a grid line, the dark blue and red populations are composed of steps occurring within 0.63 μm of an x or y grid line, respectively, and the light blue population is composed of steps occurring within 0.63 μm of both grid lines. Error bars represent s.e.m. Scale bars: 5 μm.

vicinity of the TCR cluster.

TCR visualization in cells fully on grid patterns is hindered by the overall small size of the structures. Nonetheless, based on the above observations as well as past reports, it is reasonable to assume that TCRs will be generally concentrated along the grid boundaries. With this information, the grids themselves become fiduciary markers of where TCR microclusters are enriched, and statistical analysis of the data can be performed without the need for direct TCR imaging. For this analysis, all observable features in several cells were tracked, and measured escape times from each position in the cell were binned according to their proximity to zero, one vertical, one horizontal or two grid lines (Figure 2.3C–H). The results indicate that escape times increased near one grid line and greatly increased near two lines (corresponding to a grid corner) (Figure 2.3C,F). Because actin within the T cell can only interact with the metal substrate barriers through TCR–pMHC or possibly also LFA–ICAM interactions[17,45], the slowing of actin movement near grids reflects interactions between actin and these proteins on the cytoplasmic side of the T cell membrane. The escape times of all four populations remained essentially constant when cells interacted with control substrates of chromium crosses that did not block long-range TCR transport (Figure 2.3D,G) and when cells were not on grids (Figure 2.3E,H).

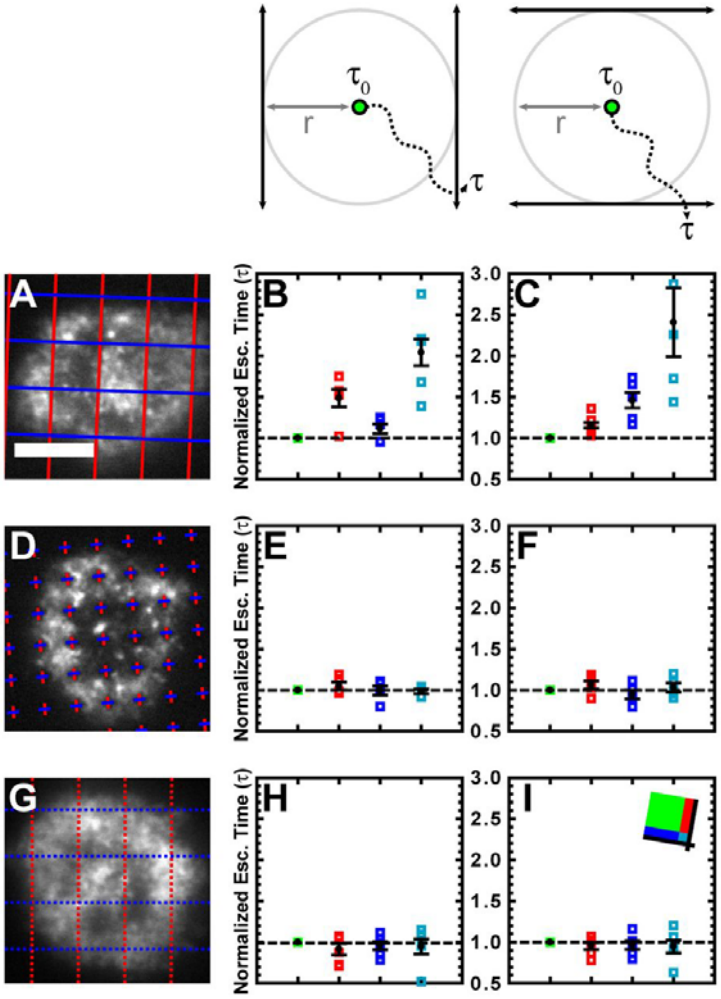


Figure 2.4. Increased actin escape times correspond to motion perpendicular to TCR diffusion barriers. (**A,D,G**) Representative frames from time lapses show cells interacting with a grid-patterned substrate (**A**), a cross-patterned substrate (**D**) or an unpatterned substrate overlaid with the grid used for analysis (**G**). (**B,E,H**) The escape time analysis from Figure 2.3 was repeated for the cells in **A,D,G**, but the escape time was redefined as the time it takes for a feature to move outside of an area identified by boundaries tangential to the original escape area and parallel to the y grid line (schematic above column). This in effect considers only the *x* component of motion of the feature. (**C,F,I**) The escape time analysis from Figure 2.3 was repeated for the cells in **A,D,G**, but the escape time was redefined as the time it takes for a heterogeneity to move outside of an area identified by boundaries tangential to the original escape area and parallel to the x grid line (schematic above column). This in effect considers only the *y* component of motion of the feature. Error bars represent s.e.m. Scale bars: 5 μm.

To determine whether actin features are slowed by the mere presence of TCRs or by resistance against their motion from barriers, the directional components of escape times parallel or perpendicular to grid lines were evaluated. These components referred to the amount of time it took a feature to traverse a total vector distance equivalent to the original escape distance in the *x* or *y* direction, as defined by the layout of the grid (Figure 2.4; supplementary material Figures S4, S5 in the associated manuscript[18]). The components of the escape time perpendicular to a barrier increased in the populations of features near that barrier, whereas components of the escape time parallel to the barrier were essentially unaffected (Figure 2.4A–C). Also unaffected by this analysis method were all components in cells interacting with diffusion-permissive substrates patterned with chromium crosses and all components in cells that were not on grids (Figure 2.4D–I). These data suggest that active resistance to TCR cluster motion as opposed to the mere presence of TCRs is necessary to induce a slowing of the cortical actin cytoskeleton and it is unlikely that the effect is an artifact of nonspecific cell interactions with chromium.

2.3.4 Coordinated actin fluctuations near TCRs

In time-lapse recordings of EGFP–β-actin, actin accumulations frequently appeared adjacent to substrate barriers (supplementary material Movie 1 in the associated manuscript[18]). These accumulations transiently increased in intensity before dissipating to the background level of fluorescence without translocating past the barrier towards the center of the immunological synapse. Such large-scale fluctuations in total actin density indicate a large degree of coordination in the coupling between actin and T cell surface proteins, including TCRs. Although interactions between actin and TCRs have generally been described as dynamic, the nearly complete dissipation of actin accumulations observed here is somewhat unexpected. At the label densities used in these experiments, the observed fluctuations reflect real dissipation of the actin itself, rather than stochastic fluctuations in fluorophore density. We observed fluorescence intensity accumulations that were two to four times higher than the cell background level that exhibited near 100% variance (complete dissipation). This is more than an order of magnitude beyond what can be expected from stochastic fluctuations[92].

To better characterize the spatiotemporal dynamics of EGFP–β-actin, we developed a numerical approach based on time-autocorrelation of fluorescence intensity as a function of spatial position. This method is distinct from previously developed image correlation spectroscopy (ICS)[93] and spatiotemporal ICS (STICS)[94–97] in that there is no correlation of the spatial coordinates. Methods like ICS and STICS can be powerful ways to analyze the dynamics of protein clusters in cells, but they are limited in cases where the cluster sizes are heterogeneous. Our approach effectively identifies transient accumulations of arbitrary size with dynamics that are distinct from stochastic fluctuations in the EGFP–β-actin matrix.

In a typical EGFP–β-actin-labeled cell (Figure 2.5A–C), the EGFP–β-actin time-average is a weak indication of where and for how long accumulations occur (Figure 2.5D). However, the frame-by-frame fluorescence intensity profiles of areas corresponding to accumulations (Figure 2.5D,E, blue areas and traces) show discrete large-scale intensity fluctuations, whereas in nearby areas lacking accumulations

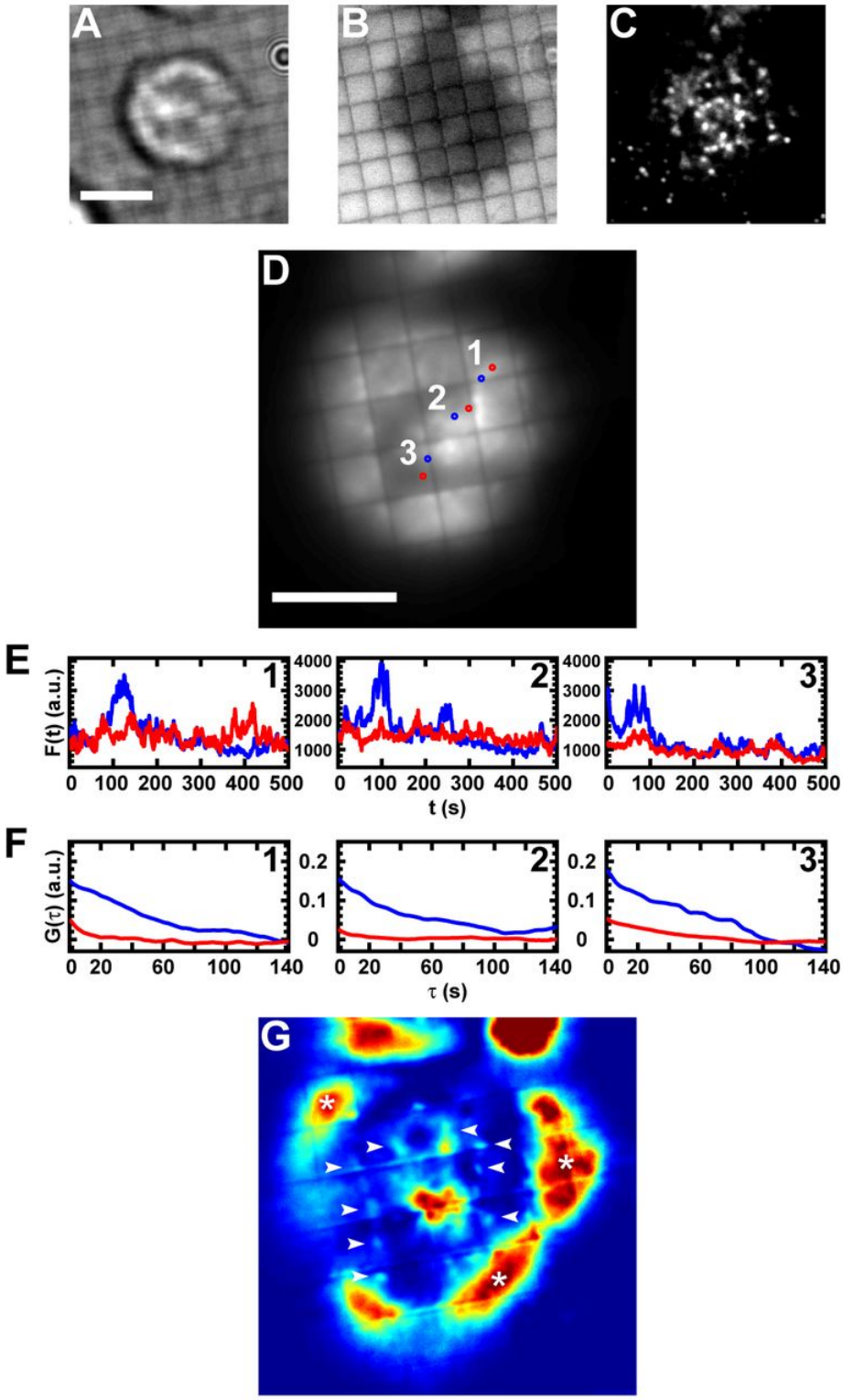


Figure 2.5. Transient enrichments of the actin cytoskeleton occur at TCR clusters. (**A–C**) Images taken before cytoskeletal time-lapse recording show the bright field (**A**), RICM (**B**) and TCR channel (**C**) views of an EGFP–β-actin-labeled cell. (**D**) The entire cytoskeletal time-lapse recording was time-averaged and areas corresponding to actin accumulations (blue regions 1, 2 and 3) and nearby background areas (red regions 1, 2 and 3) selected. (**E**) Fluorescence intensity profile over time is shown for each pixel within the regions selected in **D**. (**F**) Autocorrelation of the results shown in **E**. (**G**) The integral of the autocorrelation of the fluorescence intensity profile of every pixel in the cytoskeletal time-lapse image stack is output in the *x*–*y* location corresponding to its original pixel and displayed according to a color scale of arbitrary units. The white asterisks correspond to areas of extension and retraction of the lamellipodia and the white arrows highlight areas of high autocorrelation due to putative actin accumulations. Scale bars: 5 μm.

(Figure 2.5D,E, red areas and traces) the fluorescence fluctuates on a much smaller scale around a background value. The time-autocorrelation functions of fluorescence intensity from the respective regions clearly reflect these differences (Figure 2.5F). This

analysis can be readily applied to the entire image area, as shown in Figure 2.5G, where the integral of the autocorrelation function of each image pixel is plotted at the original pixel position. High autocorrelations in areas on the periphery of the cell correspond to extensions and retractions of the lamellipodia (Figure 2.5G, white asterisks), whereas locally high autocorrelations are visible at areas adjacent to substrate barriers (Figure 2.5G, white arrows and others). These latter areas correspond well to cytoskeletal accumulations visible in the data recordings (supplementary material Movie 1 in the associated manuscript[18]) and to areas that contain a high TCR density prior to time-lapse recording (Figure 2.5C).

2.4 Discussion

The involvement of actin in T cell signaling is well established, but recent studies have shown that beyond acting as a simple transport mechanism, the actin cytoskeleton actively modulates TCR recognition of antigen by altering TCR–pMHC kinetics[38,39]. To better understand how this modulation occurs, there is a need to move beyond bulk inhibition of the cytoskeleton with latrunculin, cytochalasin and similar compounds by probing specific receptor–actin interactions and using quantitative analysis methods to describe the outcomes. We used the hybrid live cell–nanopatterned supported lipid bilayer system to pin TCR clusters and developed specialized tracking algorithms and an image time-autocorrelation analysis to characterize properties of a mobile and fluctuating cytoskeletal network interacting with these receptor assemblies. Using these tools, we have shown that, in primary T cells, actin slows down and assembles and disassembles en masse in the vicinity of TCR clusters.

The slowing and, to some extent, the overall average increase in density of actin at the sites of pinned TCR clusters are to be expected from a receptor–actin interaction that has previously been shown to be highly dissipative, or frictional[14,17,45]. However, such a coupling does not on its own give rise to the large transient actin enrichments, or fluctuations, that we observe at these sites. We make this argument based on the fact that fluctuations in a random distribution of n independent objects scale with $\sqrt{n}$[92]. Larger-scale fluctuations are indicative of coordination within the system. Here, proximity to TCR microclusters leads to increases in large cytoskeletal fluctuations, suggesting greater degrees of coordination within the actin network. Taken in the context of studies that have shown microclusters to survive actin disruption[23,24], this finding demonstrates that TCR microclusters are the more stable element in the TCR–actin interaction and that they template the dynamic actin around themselves.

Chapter 3

Ratiometric imaging of the T-cell actin cytoskeleton reveals the nature of dynamic receptor-induced cytoskeletal enrichment

*The work presented in this chapter is being submitted for publication as part of the following short-format paper: Smoligovets, A.A., Smith, A.W., and Groves, J.T. Ratiometric imaging of the T-cell actin cytoskeleton reveals the nature of dynamic receptor-induced cytoskeletal enrichment. *Biophysical J*, (2013).

*Alexander Smoligovets conceived the experiments, prepared necessary materials and reagents, performed the experiments, analyzed and interpreted the data, and wrote the manuscript. Adam Smith performed microscopy, developed and applied the autocorrelation data analysis algorithm, and edited the manuscript.

3.1 Introduction

The T-cell actin cytoskeleton is critical for proper antigen recognition by the mammalian adaptive immune system. During T-cell receptor (TCR) triggering by antigen peptides presented on major histocompatibility proteins (pMHCs) on the surfaces of antigen-presenting cells (APCs), the T-cell actin cytoskeleton adopts a pattern of centrosymmetric retrograde flow[9,14,71]. This simultaneously promotes further TCR triggering[13] and rearranges various T-cell membrane proteins and their APC counterparts into an organized cell-cell interface termed the immunological synapse (IS)[46,47,50,67,68]. During this process, TCRs form microclusters that move to the center of the IS in an actin-dependent manner[23,24]. When engineered physical barriers interrupt the centripetal motion of TCR clusters, actin flow slows near the pinned microclusters, and the cytoskeletal network transiently accumulates and dissipates at the sites[17,18]. The amplitude and duration of the induced cytoskeletal fluctuations are much greater than would be expected for a random distribution of independent objects, indicating that the actin in the local environment is coordinated. Whether this coordination arises from a rearrangement in the existing F-actin network or represents *de novo* polymerization of the cytoskeleton, as predicted by the association of TCRs with actin polymerizing factors[6], remains unclear. Here, we use a dual-probe cytoskeleton labeling approach that distinguishes between stable and dynamic populations of actin by exploiting the different relative affinities of monomeric actin and actin-binding proteins towards each population. This strategy reveals that TCR-associated actin is composed primarily of the stable cytoskeletal fraction and that local enrichment results from three-dimensional bunching of the existing filamentous actin network.

3.2 Materials and methods

All cell culture and transduction were performed as previously described[18,78] except as follows. Dual-labeled T cells were generated by separately transfecting Phoenix cells with mKate2–β-actin or EGFP–UtrCH and then pooling the resulting retrovirus-containing supernatants prior to T-cell transduction. T cells were not selected with puromycin, but they were sorted by FACS at the UC Berkeley Flow Cytometry Facility 5 days (120 hours) after isolation. Microscopy was performed essentially as previously described[18], and three-dimensional stacks were recorded using a Stanford Photonics XR/Mega-10Z S30 ICCD camera (Stanford Photonics, Palo Alto, CA) attached to a Yokogawa CSU-X1 spinning disk head (Yokogawa, Tokyo, Japan). All microscopy hardware was controlled by the μManager software suite[98].

3.3 Results

Primary T cells from mice transgenic for the AND TCR were triggered using synthetic APCs consisting of supported lipid bilayers functionalized with pMHC and the integrin ligand intercellular adhesion molecule 1 (ICAM-1). Nanopatterned metal grids on the bilayer substrate acted as diffusion barriers that prevented lateral transport of TCR-pMHC complexes[53,76]. Dynamic enrichment of actin at TCR clusters trapped at these barriers was visualized using fluorescent fusions of actin itself (mKate2–β-actin)

and the F-actin binding domain of utrophin (EGFP–UtrCH). Such a dual-probe strategy allows for discrimination between different pools of actin: dynamic populations characterized by high polymerization and/or short filament fragments tend to be relatively better labeled by direct actin fusions whereas stable populations composed of longer filaments can support higher labeling by fluorescent fusions of F-actin binding proteins. This visualization method has been effective in distinguishing actin populations during wound healing in Xenopus oocytes[77], and in Jurkat cells it recently revealed the presence and influence of actin arcs in the lamella[20].

Our results show that the T-cell periphery is relatively enriched in mKate2–β-actin (Figure 3.1C, box 1), while EGFP–UtrCH dominates towards the center of the IS (Figure 3.1C, box 2). We infer from this probe distribution that the cytoskeleton at the T-cell periphery is composed of short fragments and is a site of active polymerization, whereas at the center of the IS, actin filaments are longer and predominantly stable. This is consistent with previous models of the T-cell actin network[14,20]. An effective way to highlight each of these cytoskeletal regions is to consider the relative ratios of the two probes at each location. In this case, a high UtrCH/actin ratio corresponds to stable actin, and a high actin/UtrCH ratio corresponds to dynamic actin (Figure 3.1D).

Actin enrichment at trapped TCR clusters incorporates both mKate2–β-actin (Figure 3.2A and C) and EGFP–UtrCH (Fig. 3.2B and C). The relative UtrCH/actin ratio at these sites (Fig. 2 D, box 2) is quite high relative to nearby background areas (Figure 3.2D, box 1), indicating that the actin is derived primarily from the stable actin population.

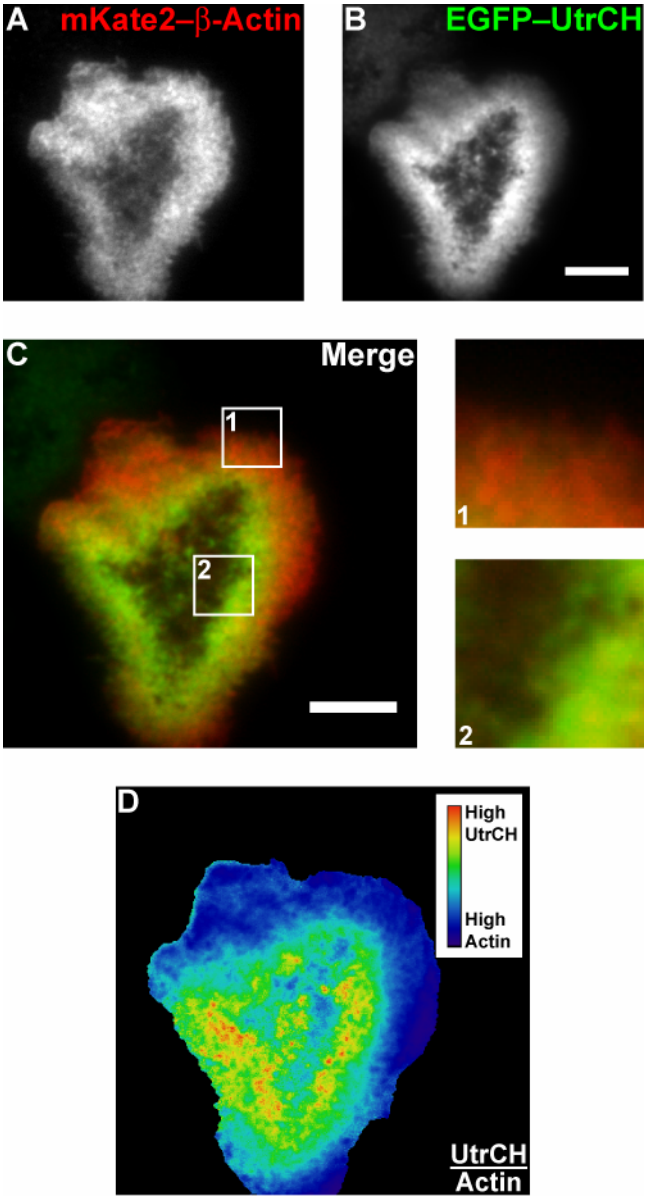


Figure 3.1. Ratiometric imaging of the cytoskeleton in live T cells distinguishes between dynamic and stable actin populations. (**A**) mKate2–β-actin, (**B**) EGFP–UtrCH, and (**C**) merged images of a triggered T cell show different actin pools. The cutouts in (**C**) correspond to a region high in dynamic actin featuring short, polymerizing filaments and/or actin monomers (**1**) and a region with a stable actin population featuring longer filaments to which UtrCH can bind (**2**). (**D**) The UtrCH/actin ratio image highlights pools of relatively high UtrCH (red) or actin (blue). (Scale bars: 5 μm.)

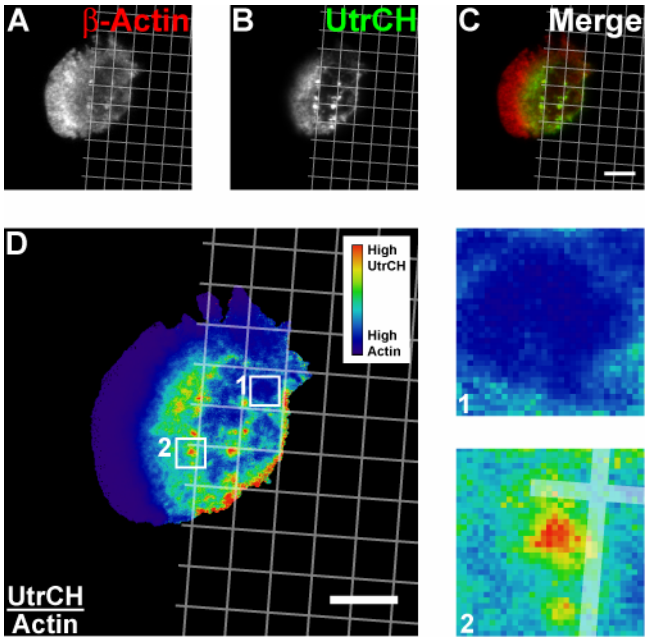


Figure 3.2. Dynamic receptor-induced cytoskeletal enrichment at sites of pinned TCRs corresponds to a primarily stable actin fraction. (**A**) mKate2–β-actin, (**B**) EGFP–UtrCH, and (**C**) merged images of a triggered T cell interacting with a nanopatterned supported lipid bilayer show actin enrichment corresponding to putative sites of pinned TCRs. (**D**) The UtrCH/actin ratio is high at sites displaying actin enrichment, indicating a primarily stable actin fraction in these regions (**1**) compared to nearby background areas (**2**). (Scale bars: 5 μm.)

The three dimensional distribution of TCR-associated actin was analyzed in dual-labeled live T cells using a spinning disk confocal microscope. The recordings show actin extending away from the cell membrane in the vicinity of trapped TCRs, while the rest of the actin cytoskeleton remains relatively flat (Figure 3.3). These protrusions of actin away from the membrane surface are predominantly composed of stable, filamentous actin, as indicated by their relatively high UtrCH/actin ratio (Figure 3.3B).

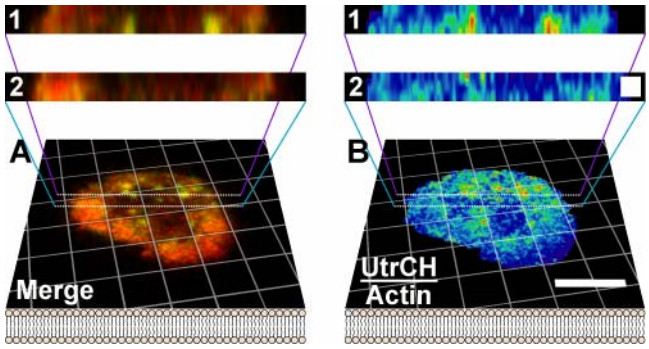


Figure 3.3. Three-dimensional ratiometric imaging shows that actin enrichment extends away from the cell membrane. Single planes from (**A**) merged mKate2–β-actin and EGFP–UtrCH and (**B**) UtrCH/actin ratio three-dimensional stacks show actin enrichment at the cell membrane. Cutouts represent Z-projections passing through sites of enrichment (**1**) and nearby background regions (**2**). The color distribution in B is analogous to that in Figures 3.1D and 3.2D, and is omitted for clarity. (Scale bar: 5 μm in the *x* axis only. Scale box: 1 μm.)

3.4 Discussion

These results indicate that the filamentous actin network is relatively dense at sites of pinned TCRs. Although TCRs are intentionally trapped as part of this experimental strategy, it is likely APCs can naturally impede TCR ligand mobilities under certain circumstances, and this been shown to impact T-cell signaling[99,100]. Actin architecture near cell surface proteins has been extensively studied in focal adhesions of fibroblasts[101], but the lack of stress fibers in T cells makes it unlikely that the two structures are similar. Thus, dynamic receptor-induced cytoskeletal enrichment at TCR clusters adds to the catalog of actin behaviors *in situ*, which is conveniently probed by techniques such as ratiometric dual-probe imaging in live cells.

Chapter 4

Direct single molecule measurement of MHC/agonist:TCR unbinding kinetics in living primary T cells

*The work presented in this chapter is being submitted for publication as part of the following paper: O'Donoghue, G.P., Pielak, R.M., Smoligovets, A.A., Lin, J.J., and Groves, J.T. Direct single molecule measurement of MHC/agonist:TCR unbinding kinetics in living primary T cells. (2013).

*Geoff O'Donoghue and Rafal Pielak conceived and performed the experiments, analyzed and interpreted data, and wrote the manuscript. Rafal Pielak also prepared some of the necessary reagents. Alexander Smoligovets prepared necessary materials and reagents, cultured cells, performed experiments, and contributed to the manuscript. Jenny Lin performed experiments and analyzed data.

4.1 Introduction

An essential aspect of adaptive immunity is the ability of T cells to discriminate between structurally similar agonist and non-stimulatory self peptides bound to major histocompatibility complex molecules (MHC) presented on the surface of antigen-presenting cells (APCs). Fewer than 10 MHC/agonist molecules have been shown to trigger signaling reactions in T cells, even when self-peptides outnumber agonist by at least 100:1[102,103]. Furthermore, this signaling response can occur on a timescale of seconds[104]. For decades, hypotheses explaining this exquisite T cell sensitivity and specificity for agonist have been based on peptide-specific differences in binding parameters such as the equilibrium dissociation constant (K_d)[105] and the kinetic off-rate (k_{off})[106], and largely based on experimental correlations between solution assays of MHC/peptide binding of T cell receptor (TCR) and bulk measurements of T cell activity and proliferation. Recently, several groups have reported single molecule measurements of MHC/agonist:TCR binding kinetics at cell-cell[39] and cell-supported lipid bilayer (SLB)[38,107] interfaces. The results are intriguing, but also perplexing. The long-lived MHC/agonist:TCR complexes observed in solution measurements were not observed on the cell surface. Instead, the kinetic off-rates appear to be orders of magnitude faster than the corresponding solution kinetics (150 ms vs. 8-30 s measured by SPR at 25°C for the 5C.C7 and 2B4 TCRs)[38,107]. This discrepancy has called for a reevaluation of the physical basis of agonist discrimination and signal amplification by T cells in an effort to account for rapid binding and unbinding of a single MHC/agonist to multiple TCRs.

Here we report direct observations of MHC/agonist binding dwell times in living primary AND T cells using a multi-timescale single molecule fluorescence imaging approach. Key to this strategy is the variable control of excitation dose and hardware discrimination of molecular species with different mobilities, which enables unambiguous tracking of individual molecules for up to minutes before photobleaching. This facilitates observation of long-lived states, which can easily be obscured by photobleaching. Under these conditions, long-lived MHC/agonist:TCR complexes are observed with a mean dwell time of 69.3±13.0 s. This is within the range of solution measurements of MHC/agonist:TCR molecular binding kinetics[107,108] and at least 400 times longer than recent reports with 5C.C7 and 2B4 live cell systems[38,107].

4.2 Materials and methods

4.2.1 DNA, protein, and T cell preparation

A plasmid containing enhanced green fluorescent protein fused to CD3 zeta-chain-associated protein of 70 kDa (Zap70-EGFP) was a gift of Takashi Saito, RIKEN Research Center for Allergy and Immunology, Yokohama, Japan[26]. The Zap70-EGFP gene was amplified by PCR and subcloned into a murine stem cell virus parent vector (pMSCV).

Bi-hexahistidine-tagged major histocompatibility complex (MHC) class II I-E^k protein was produced and purified as previously described[87]. A decahistidine-tagged ICAM-1-TagBFP fusion protein was generated by PCR amplifying the TagBFP

sequence (Evrogen Inc., Moscow, Russia) and subcloning it into a pN1-ICAM-1 vector. The entire ICAM-1-TagBFP gene was then further subcloned into the pFastBac1 vector (Invitrogen Inc., Carlsbad, CA), which was used to generate baculovirus for infection of High Five cells (Invitrogen Inc., Carlsbad, CA). The ICAM-1-TagBFP was subsequently purified on a Ni-NTA-Agarose affinity column, eluted with an imidazole gradient, dialyzed, and stored in Tris buffer containing 10% glycerol. AND CD4+ T cells[80] were harvested and cultured essentially as previously described[18,78].

T cells were transduced with Zap70-EGFP and sorted using fluorescence-activated cell sorting (FACS) according to viability and EGFP expression. The population of transduced cells that was used expressed EGFP at no more than 50% of the highest EGFP level in the overall EGFP-positive population.

4.2.2 Peptide purification and labeling

Using the basic sequence of moth cytochrome *c* (amino acids 88-103) and previously described variants[38], the following peptides were synthesized by David King at the HHMI Mass Spectrometry Laboratory at UC Berkeley and/or commercially: MCC (ANERADLIAYLKQATK), MCC(C) (ANERADLIAYLKQATKGGSC), MCC-null(C) (ANERAELIAYLTQAAKGGSC). For fluorophore labeling, cysteine-containing peptides were dissolved in a small amount of non-saline phosphate buffer and mixed in a 1:2 molar ratio with Atto 647N resuspended in a small amount of 1-propanol or lyophilized Atto 488 (Atto-Tec GmbH, Siegen, Germany) and labeled using maleimide-thiol chemistry. The peptides where then incubated at room temperature for at least 1 hour and purified on a C18 reverse phase column (Grace–Vydac, Deerfield, IL) and H_2O:acetonitrile gradient using ÄKTA explorer 100 FPLC system (Amersham Pharmacia Biotech, Piscataway, NJ). Peptide identity was confirmed after purification using mass spectrometry.

4.2.3 Microscopy

TIRF experiments were performed on an inverted microscope (Nikon Eclipse Ti; Technical Instruments, Burlingame, CA) using a custom-built laser launch with 488 nm (Sapphire HP; Coherent Inc., Santa Clara, CA) and 640 nm (Cube; Coherent Inc., Santa Clara, CA) diode lasers, as described previously[106]. Laser powers measured at the sample were 0.8 mW (640 nm) and 0.5 mW (488 nm) for 500 ms exposures and 4.4 mW (640 nm) for 17.5 ms exposures. A dichroic beamsplitter (z488/647rpc; Chroma Technology Corp., Bellows Falls, VT) reflected the laser light through the objective lens (Nikon 1.49 NA TIRF; Technical Instruments, Burlingame, CA) and fluorescence images were recorded using an EM-CCD (iXon 597DU; Andor Inc., South Windsor, CT) after passing through a laser-blocking filter (Z488/647 M; Chroma Technology Corp., Bellows Falls, VT). Bandpass filters (FF03 525/50; Semrock Inc., Rochester, NY and ET 700/75, Chroma Technology Corp., Bellows Falls, VT) were placed in a DualView 2 Simultaneous Imaging System (Photometrics, Tuscon, AZ). Colors were registered by imaging 100 nm Tetraspec beads (Invitrogen Inc., Carlsbad, CA) deposited on a coverslip patterned with a Cr grid with ~80 nm width and 3-4 μm pitch Cr lines, since the Tetraspec beads preferentially bind the regular Cr pattern. Exposure times and time-

lapse periods (500ms and 10s, respectively, for Figure 4.5) for most experiments were set using image collection software (MetaMorph 7.5; Molecular Devices Inc., Downingtown, PA), which drives an external shutter (Uniblitz LS6; Vincent Associates, Rochester, NY). Exposure time and Fast Kinetics Mode for short (17.5 ms) integration time experiments were set using Andor Solis (Andor Inc., South Windsor, CT). Exposure times were measured directly from the Fire output of the EM-CCD using an oscilloscope (TDS 210; Tektronix, Inc., Beaverton, OR).

4.2.4 Imaging chamber and supported lipid bilayer preparation

Single unilamellar vesicles (SUVs) were formed by tip sonication of a solution composed of 98 mol % 1,2-dioleoyl-sn-glycero-3-phosphocholine (DOPC) and 2 mol % 1,2-dioleoyl-sn-glycero-3-[(N-(5-amino-1-carboxypentyl) iminodiacetic acid) succinyl] (nickel salt) (Ni^{2+}-NTA-DOGS) (Avanti Polar Lipids; Alabaster, AL). Tip sonication was preferred to vesicle extrusion due to the introduction of significant levels of fluorescent impurities into the SUVs during extrusion. Prior to experiments, #2 40 mm diameter round coverslips were ultrasonicated for 30 minutes in 50:50 isopropyl alcohol:water, rinsed thoroughly in Milli-Q water (EMD Millipore, Billerica, MA), etched for 5 minutes in piranha solution (3:1 sulfuric acid:hydrogen peroxide), and again rinsed thoroughly in Milli-Q water. The coverslips were used in the assembly of FCS2 Closed Chamber Systems (flow cells; Bioptechs, Butler, PA), which were pre-filled with Tris-buffered saline (TBS; 19.98 mM Tris, 136 mM NaCl, pH 7.4; Mediatech Inc., Herndon, VA). SUVs were then flowed into the chambers, and bilayers were allowed to form for at least 30 minutes. The bilayers were rinsed once with TBS, incubated for 5 minutes with 100 mM $NiCl_2$ in TBS, rinsed with TBS, and then rinsed with a T cell imaging buffer composed of 1 mM $CaCl_2$, 2 mM $MgCl_2$, 20 mM HEPES, 137 mM NaCl, 5 mM KCl, 0.7 mM Na_2HPO_4, 6 mM d-glucose, and 1% w/v bovine serum albumin. 48 hours prior to experiments, MHC was loaded with peptide at 37ºC in a buffer composed of 1% w/v bovine serum albumin in phosphate-buffered saline and brought to pH 4.5 with citric acid. Unbound peptide was separated from peptide loaded MHC (pMHC) using 10K spin concentrators (Amicon Ultra, Cork, Ireland) and then pMHC was diluted in imaging buffer. ICAM-1-TagBFP and pMHC were further diluted with imaging buffer, introduced into the flow cells, and incubated for 35 minutes followed by a rinse with imaging buffer. T cells were spun down, resuspended in imaging buffer, and added to the flow cells 35 minutes after the final rinse and imaged immediately for 30-60 minutes. To visualize TCR, T cells were incubated in a solution of 1 µl Alexa 647 (Invitrogen Inc., Carlsbad, CA)-labeled H57 anti-TCR Fab: 100 µl imaging buffer for 20 minutes at 4ºC prior to the regular imaging buffer resuspension. All other incubations during this protocol were performed at room temperature, and imaging experiments were performed at 37ºC.

4.2.5 Data analysis

Single molecule diffraction-limited spots were detected in raw .tif image stacks of MCC-Atto 488 and MCC-647N molecules by filtering for both size and intensity and linked into tracks using published particle detection and tracking algorithms[109] adapted for MATLAB (The Mathworks; Natick, MA) by Daniel Blair and Eric Dufresne

(http://physics.georgetown.edu/matlab/; accessed 16 August 2012). Size and intensity thresholds were first determined by eye using a test data set and then applied uniformly to all data collected with the same exposure time and incident laser intensities. Single molecule behavior was confirmed by step photobleaching detected in an automated way using a Bayesian change point detection algorithm[110].

Zap70-EGFP puncta (as shown in Figure 4.2C) were detected using a gradient vector flow algorithm[18,21] and tracked using a nearest-neighbor algorithm. Zap70-EGFP intensity traces like those in Figure 4.2B were obtained by summing the intensity of the Zap70-EGFP channel using the MCC-Atto 647N molecule position as a mask.

Lifetime distributions were fit to an exponential function of the form $f(\tau) = \langle \tau_{ob} \rangle^{-1} e^{-\tau/\langle \tau_{ob} \rangle}$, where τ_{ob} is the observed dwell time in our experiments. The individual kinetic transitions were derived assuming the following model:

$$pMHC_{fast-mobility} \underset{k_{off}}{\overset{k_{on}}{\rightleftharpoons}} pMHC_{slow-mobility} \xrightarrow{k_b} pMHC_{bleached},$$

where $pMHC_{fast\text{-}mobility}$ is the fast-mobility state, $pMHC_{slow\text{-}mobility}$ is the slow-mobility state (or the TCR stably bound state), $pMHC_{bleaching}$ is the bleached slow-mobility state, k_{off} and k_{on} are the rates of transitions between the slow-mobility state and the fast-mobility state, and k_b is the rate of transition from the slow-mobility state to the bleached state. We assume that the transitions between the kinetic states represent a Markov memory-less process and use probability theory to derive a probability density function (PDF) for the single molecule dwell time distribution described by the above model. The corresponding PDF describing observed dwell time distribution is as follows: $f(\tau) = \left(\langle \tau_b \rangle^{-1} + \langle \tau_{off} \rangle^{-1} \right) e^{\tau \left(\langle \tau_b \rangle^{-1} + \langle \tau_{off} \rangle^{-1} \right)}$, where $\left(\langle \tau_b \rangle^{-1} + \langle \tau_{off} \rangle^{-1} \right)^{-1} = \langle \tau_{ob} \rangle$ is the observed mean dwell time in our experiments. Atto 488 and Atto 647N SLB bleaching curves were background subtracted and then fit to an exponential decay function of the form $f(t) = k_b e^{-k_b t}$. Fitting was done using MATLAB.

4.2.6 Stochastic kinetic simulation

Simulations were performed using MATLAB. Our simulation models a TCR cluster as a square lattice upon which MCC molecules bind discrete TCR lattice sites for duration τ_{off}^{i}, where τ_{off}^{i} is treated as a random variable drawn from an exponential distribution with mean equal to $\langle \tau_{off} \rangle$. $\langle \tau_{off} \rangle$ is varied over several orders of magnitude and is chosen to match measured values from the literature. After each time period (determined by τ_{off}^{i}), the MCC molecule steps to a new lattice site or stays at the same lattice site (each TCR lattice site is assumed to be 10nm by 10 nm) until the MCC is no longer on the TCR cluster, such that $\tau_{esc}^{k} = \sum_{i=0}^{n} \tau_{off}^{i} + \sum_{i=1}^{n} \tau_{on}^{i} + \tau_{exit}$, where n indicates the number of steps an individual MCC molecule takes before exiting the TCR cluster, τ_{on} is the time period between binding events, and τ_{exit} is the time between the last unbinding event and the ultimate exit from the TCR cluster. Step size is treated as a combination of two independent random variables, $(\Delta x, \Delta y)$ drawn from Gaussian distributions with

mean 0 and standard deviation $\sqrt{2D_{SLB}\tau_{on}}$.The step size is then a random variable $\Delta r = \sqrt{\Delta x^2 + \Delta y^2}$ and the angle of displacement is drawn from a uniform distribution. The interval between binding events, τ_{on}, is treated as a random variable drawn from an exponential distribution with mean $k_{on} \cdot \rho_{TCR}$, where the density of TCR, ρ_{TCR}, is taken to be 10,000 molecules/μm^2 (as in the central supramolecular activation cluster). In this way $\langle \tau_{esc} \rangle = \frac{1}{k}\sum_k \tau_{esc}^k$, where *k* is the number of iterations (100 in the case of Figure 4.6 and Figure 4.7), is calculated for every combination of $\langle \tau_{off} \rangle$, TCR cluster size, and k_{on}. Note that since $\tau_{off} >> \tau_{on}$, $\frac{\tau_{esc}}{\tau_{off}} \approx \langle n \rangle$, where $\langle n \rangle$ is equivalent to the TCR cluster size. This relationship between $\frac{\tau_{esc}}{\tau_{off}}$ and TCR cluster size can be seen in Figure 4.7. It is possible that MHC/agonist binding interactions with CD4 could slow the mobility individual MHC/agonist within a TCR cluster relative to D_{SLB} when the MHC/agonist are unbound from TCR. This could hypothetically lead to entrapment and long single molecule tracks (like those reported here) in the absence of direct, sustained MHC/agonist-TCR interactions. While such a mechanism is conceivable, there is no direct evidence for such a tethering mechanism in the literature.

4.3 Results

4.3.1 Hardware filtering and characterization of MHC/agonist:TCR complexes

We probe MHC/agonist:TCR complex dynamics in hybrid live cell–SLB junctions[68] (Figure 4.1A). The fully fluid SLB is functionalized with MHC (I-E^k) and intercellular adhesion molecule-1 fusion with a blue fluorescent protein (ICAM-TagBFP), both linked to the membrane via C-terminal poly-His tag binding to Ni^{2+}-chelating lipids[87]. The MHC is loaded with peptide (moth cytochrome *c* (MCC) agonist or null) that is covalently coupled in a 1:1 stoichiometry (verified by HPLC) to the photostable fluorophores Atto 647N or Atto 488 using maleimide-thiol chemistry. Upon contact between the T cell and the supported membrane, LFA-ICAM binding leads to rapid cell spreading and formation of an essentially planar interface between the T cell and supported membrane, within which MHC/peptide:TCR interactions occur.

At fast exposure times (17.5 ms) and high excitation powers (0.2 W/cm^2), all individual MHC/agonist molecules are readily resolved (Figure 4.1B, top; Figure 4.1C). In regions without a cell, MHC/agonist diffused freely. The step-size distribution from these trajectories is Gaussian and corresponds to a single lateral diffusion coefficient of 0.44 (SEM = 0.002) μm^2/s, which is typical for high quality supported membranes[111]. Within the T cell junction, the step-size distribution becomes bimodal (Figure 4.1D), with a distinct slow-moving component. This result is comparable to fast frame-rate observations in other systems with reportedly different MHC/agonist:TCR kinetics[112]. MHC/agonist:TCR binding kinetics cannot be uniquely inferred from the step size distribution.

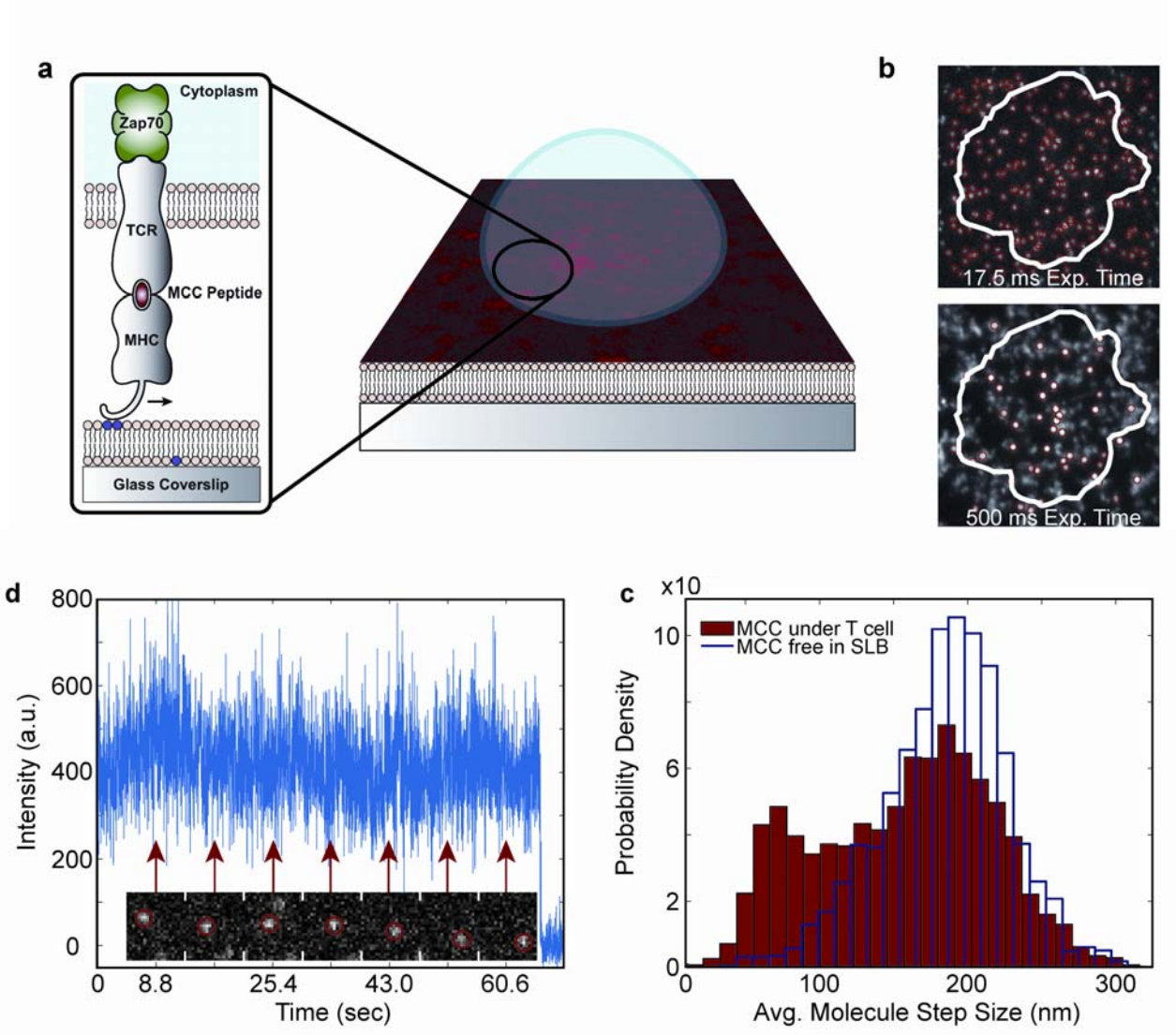


Figure 4.1. A slow mobility MCC fraction is observed after addition of live T cells. (**A**) Schematic of the hybrid live cell–SLB system. (**B**) At short exposure times (17.5 ms, top) all MCC/agonist molecules are readily resolved. Imaging with a long exposure time (500 ms, bottom) allows for unambiguous hardware discrimination between the slow, bound fraction of MCC/agonist and the fast diffusing fraction of MCC/agonist. Hardware discrimination between bound & unbound MCC/agonist fractions allows for long (1-10 s interval) time-lapse sequences (Supplementary Movie 1 in the associated manuscript). Automated detection of single molecule features (red circles) is discussed in online methods. (**C**) Representative intensity trace showing a single agonist bound continuously for ~60 s. Linear trajectory (inset) indicates engagement with the cytoskeleton. (**D**) Step size histogram of single MCC-Atto 647N molecules in a SLB is bimodal under T cells (red) and unimodal before addition of T cells (blue).

At long exposure times (500 ms) and low excitation powers (0.02 W/cm^2), the fast moving MHC/agonist fraction in Figure 4.1D is averaged over several pixels to form a relatively homogenous background. The slow moving molecules remain highly localized and can be easily tracked for longer than a minute using 1-10 s time-lapses (Figure 4.1B, bottom; Supplementary Movie 1 in the associated manuscript). Using this hardware filtering approach we observe individual MHC/agonist molecules (confirmed by single-step photobleaching, Figure 4.1C and Figure 4.2A) that colocalize with TCR

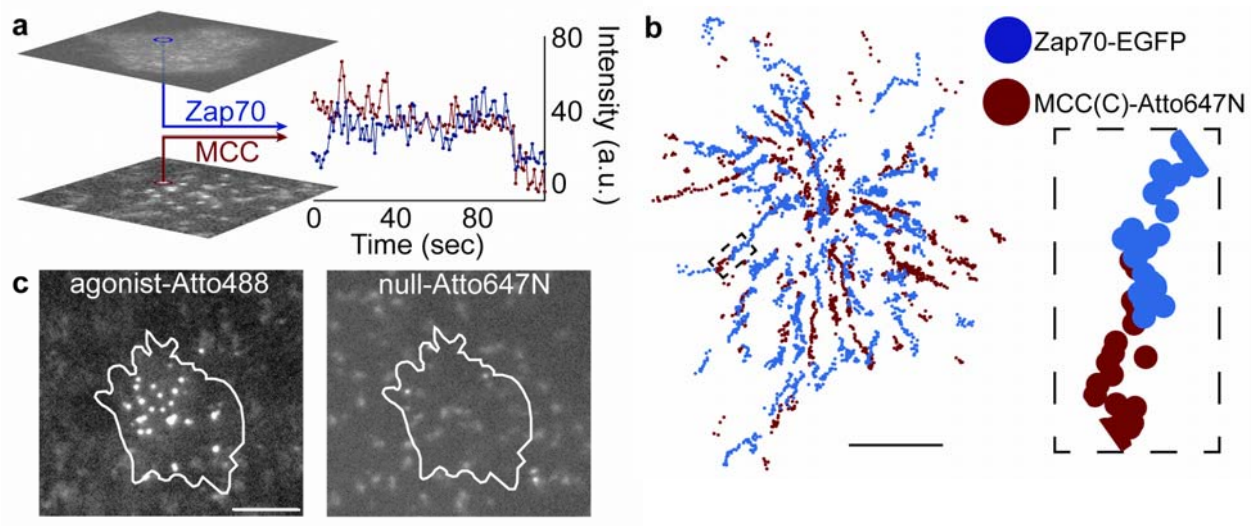


Figure 4.2. The slow mobility MCC/agonist fraction recruits Zap70, follows linear trajectories similar to Zap70, and is agonist-specific. (**A**) Single MCC molecules can result in recruitment of single Zap-70 molecules. (**B**) Both single MCC molecules and Zap70-EGFP puncta follow linear trajectories towards cell center. (**C**) Agonist specificity of slow mobility fraction. Many slow mobility MCC agonist molecules are detected, while no slow mobility null molecules are detected. Equivalent densities of free MCC and free null are used prior to addition of cells.

(Figure 4.3) and move in linear trajectories toward the geometric center of the cell-supported membrane junction. Cytosolic ZAP70-EGFP (incorporated by retroviral transfection, see online methods) exhibits stochastic colocalization with the slow-moving MHC/agonist molecules and travels along the same linear trajectories (Figure 4.2A and B), indicating that the intracellular domains of the associated TCRs are phosphorylated. The MHC/agonist densities (~0.2 molecules/μm^2) used in these experiments are near thresholds for triggering Ca^{2+} flux[103], and below levels where stable TCR microclusters are readily visible (Figure 4.3). Nonetheless, the observed single molecule MHC/agonist motion is reminiscent of the well-characterized actomyosin-driven TCR microcluster radial transport seen in cells that are activated[14,23,26,45]. Taken together, these observations suggest that individual MHC/agonist molecules are stably bound to TCR, engage the actin cytoskeleton, and form biologically functional signaling complexes with Zap70. Moreover, since every MHC/peptide:TCR complex is individually resolved in these experiments, we confirm that a single MHC/agonist:TCR complex (addressed further below) can lead to TCR triggering without molecular-scale association with other MHC molecules.

The long-lived MHC/agonist:TCR complexes are uniquely observed with agonist peptide. When MHC is loaded with a mixture of agonist and null peptides, with different fluorescent labels, only the agonist peptides are observed in the slow-moving complexes (Figure 4.2C & Figure 4.4). The result is identical when the fluorophores are reversed, excluding the possibility that fluorophore effects could be responsible for binding.

4.3.2 Single molecule MHC/agonist:TCR kinetics

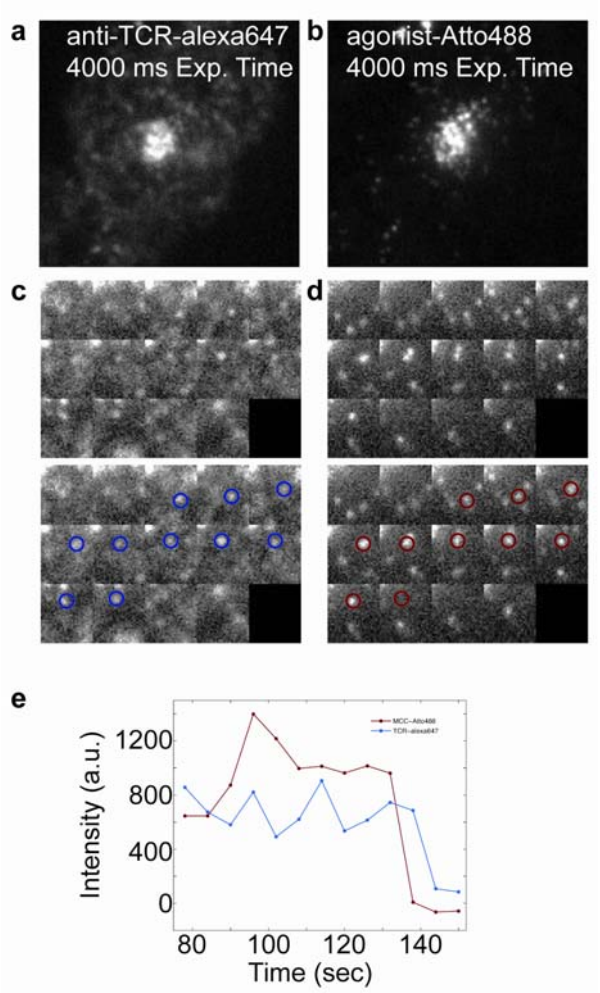


Figure 4.3. TCR and MCC colocalization. (**A-B**) TCR and MCC colocalize in bulk in the central supramolecular assembly cluster (cSMAC) and (**C-E**) at the single molecule level.

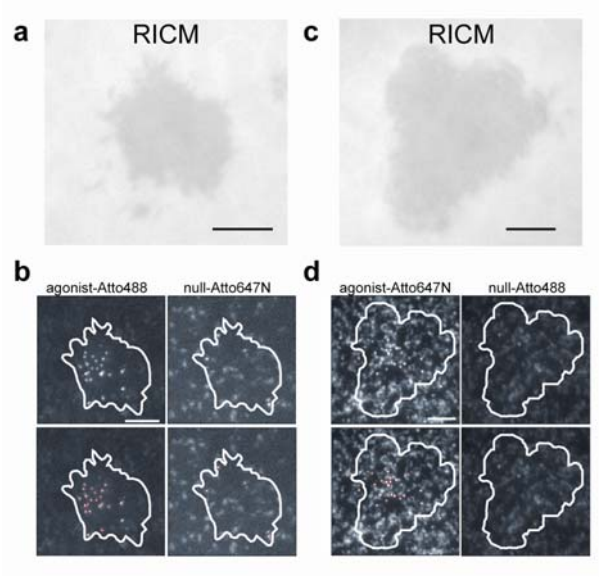


Figure 4.4. Peptide specificity is independent of fluorophore.

Since the slow-moving MHC/agonist are well-resolved from the fast moving component, the lifetime of molecules in this bound state can be directly observed. Of course unbinding and photobleaching are indistinguishable in fluorescence methods such as this. The observed distribution of dwell times can be described by

$$f(\tau) = \left(\left\langle \tau_b \right\rangle^{-1} + \left\langle \tau_{off} \right\rangle^{-1} \right) e^{\tau \left(\left\langle \tau_b \right\rangle^{-1} + \left\langle \tau_{off} \right\rangle^{-1} \right)},$$

where $\left\langle \tau_b \right\rangle^{-1}$ is the photobleaching rate (k_b), $\left\langle \tau_{off} \right\rangle^{-1}$ is the unbinding rate (k_{off}), and $\left(\left\langle \tau_b \right\rangle^{-1} + \left\langle \tau_{off} \right\rangle^{-1} \right)^{-1} = \left\langle \tau_{ob} \right\rangle$ is the observed mean dwell time in this experiment. Thus by measuring both $\left\langle \tau_b \right\rangle$ and $\left\langle \tau_{ob} \right\rangle$, it is possible to determine $\left\langle \tau_{off} \right\rangle$ as long as $\left\langle \tau_{ob} \right\rangle \le \left\langle \tau_b \right\rangle$. We determine $\left\langle \tau_{off} \right\rangle$ to be 69.3±13.0 s for Atto 488-labeled peptide agonist with $\left\langle \tau_b \right\rangle$ of 243 s (Figure 4.5). Similar values of $\left\langle \tau_{off} \right\rangle$ were measured at high MHC/agonist density (100 molecules/μm^2), which is far above minimal levels required for T cell activation and observation of stable TCR microlusters[103] (Table 4.1). We observe that cytoskeleton disruption by the actin-binding molecule latrunculin A moderately increases $\left\langle \tau_{off} \right\rangle$ with the AND TCR (Figure 4.5; Table 4.1).

Specifically, our tracking observations reveal the time intervals over which individual MHC/agonist molecules remain physically trapped within the immediate vicinity of the same TCR. Unbinding of MHC/agonist from TCR followed by rapid rebinding to the same TCR or another TCR within the same signaling cluster could

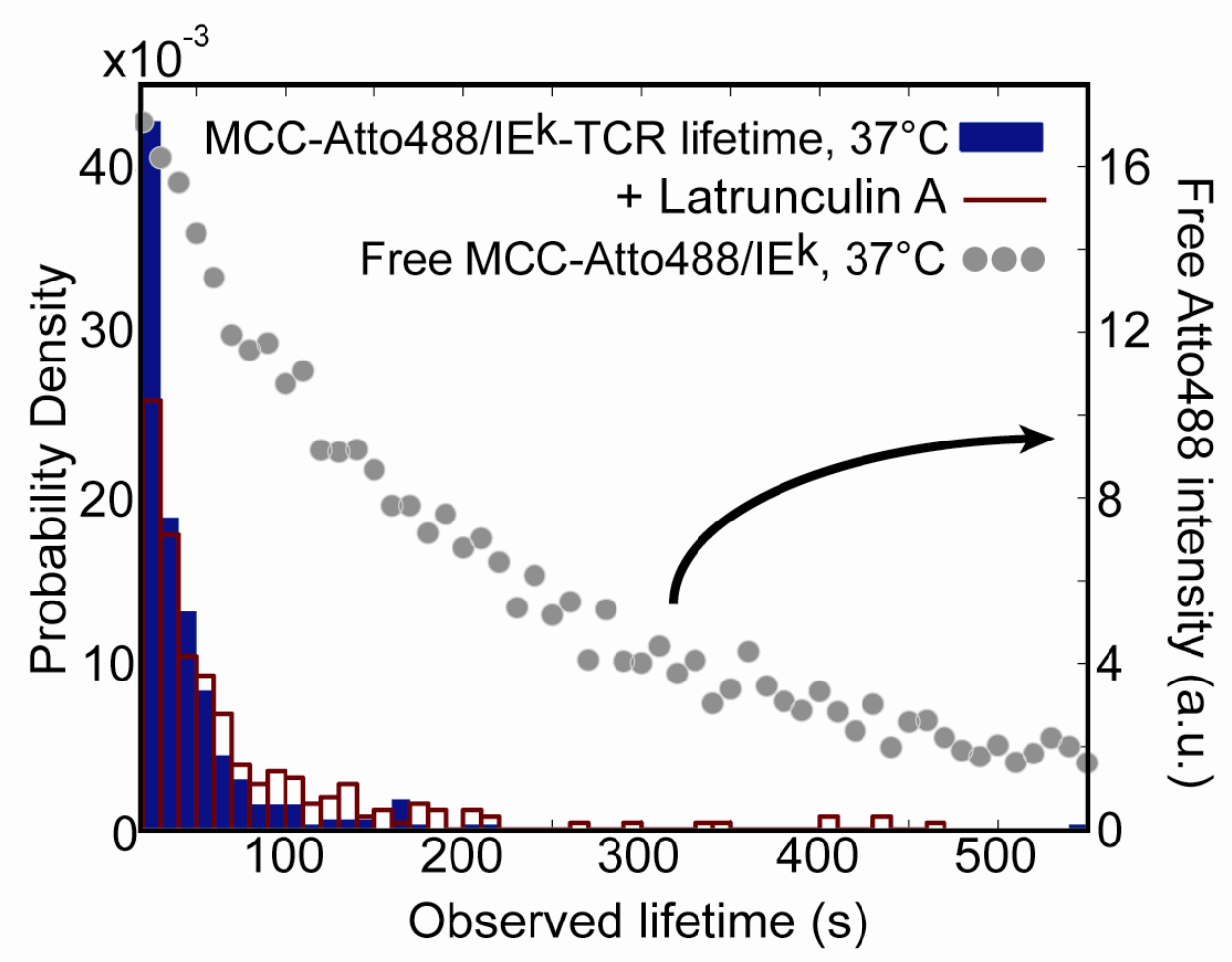


Figure 4.5. The distribution of live cell single molecule MCC/I-E^k-TCR dwell times is observed directly (blue histogram). A noticeable shift to longer dwell times is observed after addition of the actin binding small molecule latrunculin A under otherwise identical experimental conditions (red histogram). τ_{bl} = 243 s (grey circles) is measured using MCC-Atto 488/ I-E^k SLB standards without cells.

conceivably lead to entrapment of MHC/agonist for timescales longer than the lifetime of the molecular interaction. Such a phenomenon has been hypothesized as a potential mode by which a small number of MHC/agonist could trigger a larger number of TCR[113,114].

4.3.3 Stochastic reaction-diffusion simulations

We quantitatively assess the possibility of serial rebinding of MHC/agonist to different TCR within a TCR cluster using a stochastic reaction-diffusion simulation over a large range of $\langle \tau_{off} \rangle$ and TCR cluster size (Figure 4.6). The total time to escape for an individual molecule, which is the parameter directly measured in our MHC/agonist tracking experiments, is given by:

$$\tau_{esc} = \sum_{i=0}^{n} \tau_{off}^{i} + \sum_{i=1}^{n} \tau_{on}^{i} + \tau_{exit}$$

Table 4.1. Measured $\langle \tau_{off} \rangle$ values under cytoskeletal disruption, high MCC density, and low temperature. Each value in columns two and three represent ~300 MCC/I-E^k molecules per experimental condition from a population of 7-10 cells from the same mouse. In this case, uncertainty is calculated as the standard error of the mean of the molecular dwell time distribution. Uncertainty in the average across different mice, shown in column four, is calculated as the standard error of the mean of the molecular averages from two different mice.

Experimental Condition	$\langle \tau_{off} \rangle$(s) Mouse #1	$\langle \tau_{off} \rangle$(s) Mouse #2	$\langle \tau_{off} \rangle$(s) Average
37°C, 0.2 molecules/μm^2	50.9 ± 0.13	87.8 ± 0.18	69.3 ± 13.0
24°C, 0.2 molecules/μm^2	123 ± 0.04	105 ± 0.19	114 ± 6.38
37°C, 0.2 molecules/μm^2, +LatA	96.7 ± 0.03	134 ± 0.51	115 ± 13.0
24°C, 0.2 molecules/μm^2, +LatA	-	148 ± 0.47	148 ± 0.47
37°C, 100 molecules/μm^2	-	92.9 ± 0.15	92.9 ± 0.15
25°C, solution, SPR measurement	N/A	N/A	345

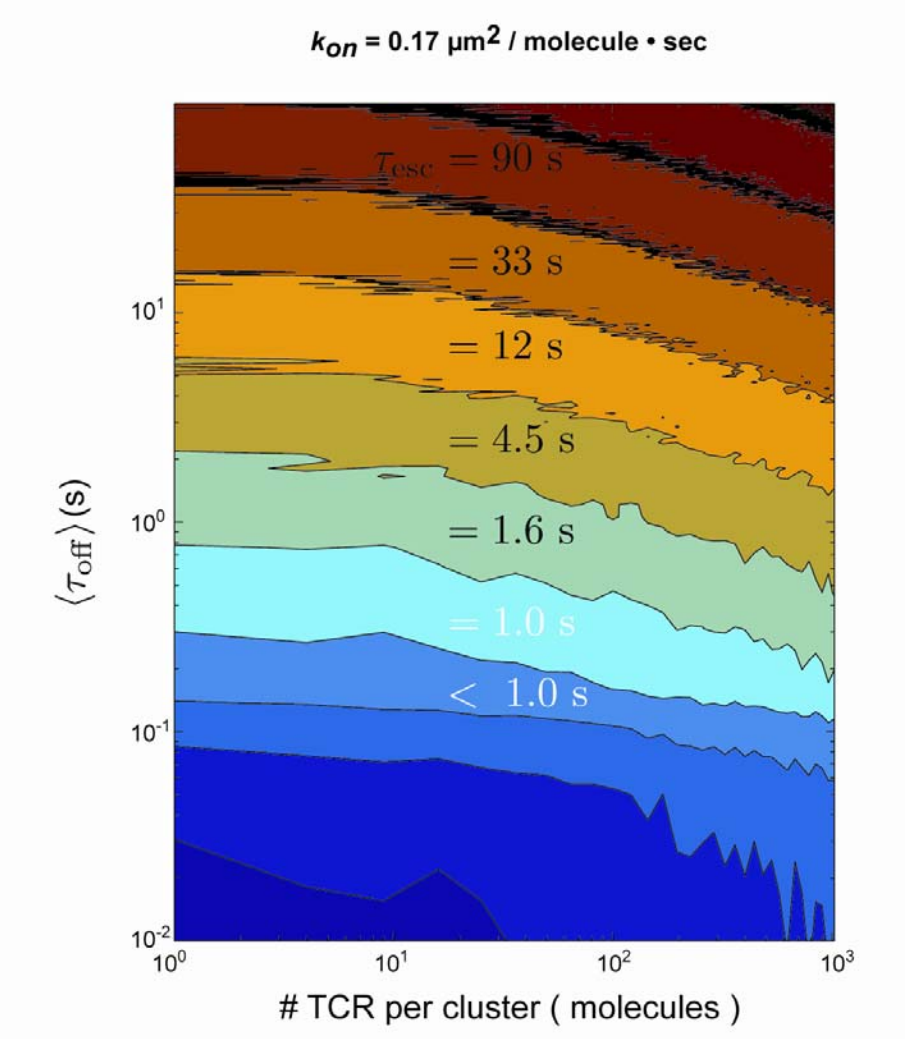


Figure 4.6. Stochastic reaction-diffusion simulation of time before MCC escape from TCR clusters, τ_{esc}. τ_{esc} (in color; log scale) varies as a function of τ_{off} and TCR cluster size. For small TCR clusters (1-100 TCR molecules) $\tau_{off} \approx \tau_{esc}$, and for large TCR clusters (1000-10,000 molecules) $\tau_{off} < \tau_{esc}$. Our simulations indicate that a measured τ_{off} ~ 70 s is unlikely to result from repeated binding/unbinding events on the millisecond time scale, since the time and length scales involved ensure that an MCC/I-E^k molecule would escape the TCR cluster and diffuse away.

In this representation, τ_{off}^{i} and τ_{on}^{i} are the individual dwell times in the bound and unbound configurations, *n* is the number of rebinding events, and τ_{exit} is the duration of the final unbound period prior to ultimate escape. For the stochastic simulation, τ_{off}^{i} and τ_{on}^{i} are treated as random variables with exponential distributions defined by k_{off} and k_{on}, respectively. If the MHC/agonist diffuses out of the TCR cluster during the unbound period (τ_{on}^{i}), it has escaped. Otherwise, the MHC/agonist rebinds and the cycle repeats. Using the fastest k_{on} (0.17 $\mu m^2 s^{-1} molecule^{-1}$) observed in similar hybrid live cell-SLB systems[38] and the measured diffusion coefficient of MHC/agonist in our supported membranes, we find that $\tau_{esc} \approx \tau_{off}$ for TCR clusters of the sizes observed experimentally[24] (≤100 TCR molecules) (Figure 4.6). Only for unrealistically large TCR clusters (up to 1000 TCR molecules) could rebinding within the same cluster lead to appreciable entrapment ($\tau_{esc} > \tau_{off}$) (Figure 4.7). These simulations indicate that the observed value of $\langle \tau_{off} \rangle \approx$ 70 s in these experiments is unlikely to be the result of repeated unbinding and rebinding of one MHC/agonist with many TCR within a TCR cluster. The observed $\langle \tau_{off} \rangle$ therefore corresponds to the molecular k_{off} for MHC/agonist:TCR binding.

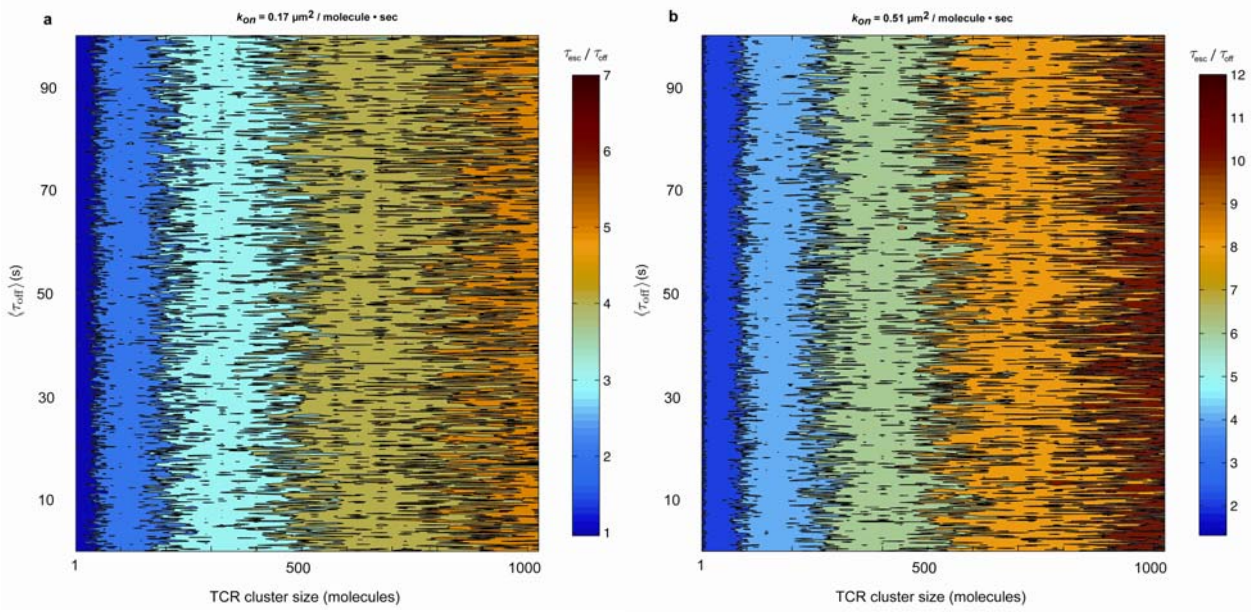


Figure 4.7 Simulations of $\frac{\tau_{esc}}{\tau_{off}}$ as a function of TCR cluster size, τ_{off}, and k_{on}. The ratio $\frac{\tau_{esc}}{\tau_{off}}$, which is an indicator of MHC/agonist entrapment, is a function of TCR cluster size and k_{on}, but not k_{off}. k_{on} = 0.51 $\mu m^2 s^{-1} molecule^{-1}$ corresponds to the fastest average k_{on} that allows for rebinding to the same TCR. Only for large TCR cluster sizes (approaching 1000 TCRs per cluster) and fast k_{on} is $\frac{\tau_{esc}}{\tau_{off}} >> 1$, meaning that entrapment due to millisecond-scale unbinding and rebinding is unlikely to result in the minute-scale dwell times observed in our experiments.

4.4 Discussion

The mean dwell time we measure for the MHC/agonist:TCR interaction is within the range of dwell times measured for agonists (1 to 300 s) in solution assays[107,108] and agrees with recent two-dimensional biochemical measurements[115]. In particular, SPR kinetic measurements of the 226 TCR, reported in conjunction with a structure of the TCR bound to MCC/I-E^k, have shown a slow dissociation rate ($\langle \tau_{off} \rangle$ = 300 s at 24°C)[107] similar to the dissociation rate reported here for the AND TCR, especially for the case of AND binding kinetics under cytoskeleton disruption (Table 4.1). All of the critical residues involved in MCC binding are conserved between the 226 and AND TCRs (Figure 4.8). Our live cell kinetic measurements coupled with these solution-phase kinetic studies of the structurally-similar 226 TCR therefore suggest that the 2D dissociation rate constant measured in living cells is not greatly accelerated as compared to solution measurements.

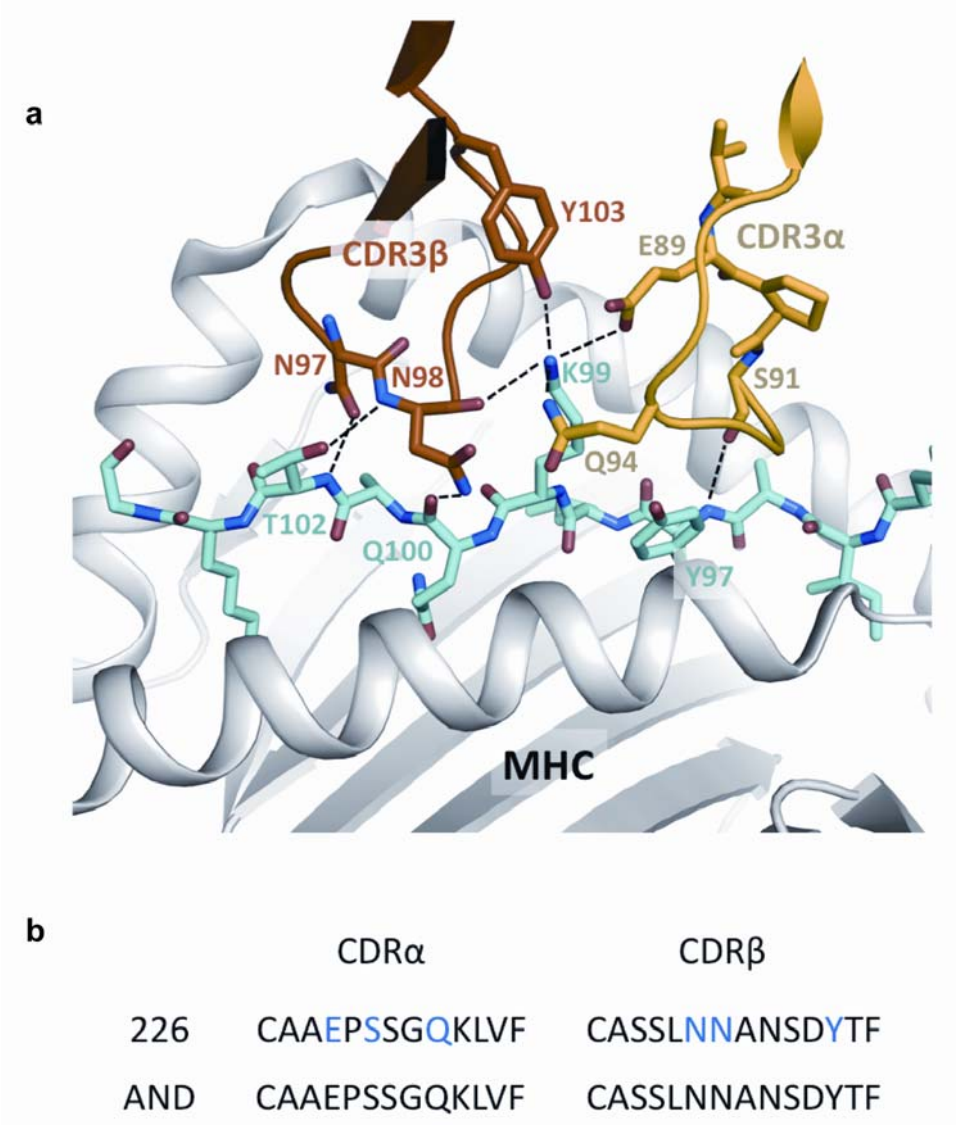


Figure 4.8. Interaction of the 226 TCR with the MCC peptide. (**A**) CDR3α (yellow) and CDR3β (orange) loops form all the specific interactions with the peptide (cyan). Hydrogen bonds between the CDR3 loops and the MCC residues are shown by dashed lines (PDB, 3QIU) (**B**) Comparison of CDR3 loops between the 226 and AND TCRs reveal identical sequences and suggest similar binding kinetics. 226 and AND also share Vα, Jα, Vβ, and Jβ - gene segments that encode the residues specific for interaction with I-E^k. The residues involved in hydrogen bonds between 226 and MCC are shown in blue.

The differences in the kinetic behavior of AND TCR compared with 5C.C7 and 2B4 deserve consideration. The same study that reports short ($\langle \tau_{off} \rangle$ ~150 ms) *in vivo* 2D dwell times, measures $\langle \tau_{off} \rangle$ 25 times longer under conditions of cytoskeleton disruption in the 2B4 and 5C.C7 systems[38], which brings $\langle \tau_{off} \rangle$ more in line with solution values. This result has been interpreted to mean that the actin cytoskeleton actively destabilizes MHC/agonist:TCR complexes. In contrast, we observe only moderate effects of actin disruption on MHC/agonist unbinding from AND by tracking measurements (Figure 4.5; Table 4.1). It is possible that structural differences between AND and both 5C.C7 and 2B4 alter the way the cytoskeleton influences MHC/agonist unbinding kinetics. If so, however, this raises questions concerning how such differing kinetics can lead to T cell triggering at comparable agonist thresholds[102,103].

It is also conceivable that the MHC/agonist:TCR complex does not remain bound in the same structural configuration for the duration of engagement. If mechanical coupling to actin significantly reduces $\langle \tau_{off} \rangle$ in a single molecule FRET measurement, but not in a single molecule tracking experiment, this raises the possibility that mechanical force induces conformational alterations in MHC/agonist:TCR without complete disengagement of the complex. CD4 is known to complex directly with MHC and could stabilize the partially disassociated MHC/agonist:TCR complex. While this putative conformational change would not affect single-molecule tracking measurements, such a conformational fluctuation could produce a FRET signature[116] or present a weakness to applied mechanical force[117]. Under such a scenario, apparently fast (millisecond-scale) $\langle \tau_{off} \rangle$ observed by FRET imaging[38] and force spectroscopy[39] may not correspond with actual escape of MHC/agonist from TCR.

In the case of AND TCR at least, all evidence reported here suggests that individual MHC/agonist remain bound to the same TCR for more than a minute in live cells. Serial rebinding of MHC/agonist to multiple TCRs in a signaling cluster is unlikely to be a universal mechanism for rapid signal amplification in T cells. The kinetics reported here for the AND TCR are comparable to solution kinetic measurements of the structurally similar 226 TCR and agree with estimates of a minimal agonist/MHC-TCR $\langle \tau_{off} \rangle$ of about 2 seconds required for negative thymic selection[118].

Chapter 5

Myosin IIA modulates T cell receptor transport and CasL phosphorylation during early immunological synapse formation

*The work presented in this chapter has been previously published as part of the following paper: Yu, Y., Fay, N.C., Smoligovets, A.A., Wu, H.-J., and Groves, J.T. Myosin IIA Modulates T Cell Receptor Transport and CasL Phosphorylation During Early Immunological Synapse Formation. *PLoS ONE*, 7(2):e30704 (2012).

*Yan Yu conceived and performed the experiments, analyzed and interpreted data, and wrote the manuscript. Nicole Fay performed calcium imaging experiments and analyzed the resulting data. Alexander Smoligovets prepared necessary materials and reagents, cultured cells, and interpreted data. Hung-Jen Wu analyzed data.

5.1 Introduction

The spatial organization of cell membrane receptors at intercellular junctions is emerging as an important aspect of many signal transduction processes[48,90,119–121]. One paradigmatic example is T cell activation in which T cell receptors (TCRs) engage their ligands, antigenic peptide loaded major histocompatibility complex proteins (pMHC), on the surface of antigen-presenting cells (APCs). This cell-cell junction, known as the immunological synapse (IS), exhibits an elaborately choreographed spatial reorganization of proteins on multiple length scales, ranging from molecular dimensions to the size of the cell itself[67,68]. Upon the triggering, T cell receptors (TCRs) collectively nucleate into microclusters of tens to hundreds of molecules together with kinases and adaptor proteins. The signaling clusters are subsequently transported centripetally, ultimately accumulating in the central supramolecular activating complex (cSMAC) where signaling is attenuated[23,24,102,122]. Meanwhile, integrins reorganize into a ring structure, forming the peripheral supramolecular activating complex (pSMAC). Interference with protein pattern formation by physically imposed barriers to TCR translocation leads to changes in TCR phosphorylation, duration and magnitude of calcium response, as well as changes in T cell triggering thresholds[53,103,123].

In the terminology of thermodynamics, force is the conjugate variable to space. As such, spatial organization and mechanical forces are intrinsically coupled; in general, one doesn't occur without the other. In the case of the immunological synapse, forces have been implicated in its formation since its initial identification[62]. Retrograde flow of the actin cytoskeleton drives segregation of signaling complexes at the IS and is required for sustaining TCR signaling[10,14,17,18,45,46]. Dynein has also been shown in a recent study to drive microtubule-dependent transport of TCRs and to negatively regulate T cell signaling[66]. In the immunological synapse, the role of non-muscle myosin IIA, the myosin II isoform that is dominantly expressed in T cells, has been debated in several studies[58,62,63], but without consensus.

Here we examine the role of myosin IIA in the formation of the immunological synapse by tracking movements of TCRs, actin, and myosin with high spatial and temporal resolution. Primary T cells are activated by pMHC and inter-cellular adhesion molecule (ICAM) −1, both of which are tethered to supported lipid bilayers by polyhistidine/nickel-chelating lipid linkages. Both proteins, freely mobile in the supported bilayer, readily assemble into microclusters and larger scale organization in response to driving forces applied by the cell. This hybrid live cell – supported membrane junction enables high resolution imaging of the immunological synapse using total internal reflection fluorescence (TIRF) microscopy[124]. By analyzing movements of TCRs, actin, and myosin, we demonstrate that myosin IIA makes a distinctive contribution to TCR cluster movement during the first one to two minutes after T cell stimulation. Inhibition with blebbistatin or ML-7 reduces both calcium influx and spatial colocalization of active ZAP-70 with TCR microclusters. Thus myosin IIA contributes, at least indirectly, to TCR signaling. A more telling observation is that myosin inhibition also reduces phosphorylation of the mechanosensing protein CasL (Crk-associated substrate of the lymphocyte type), raising the hypothesis of a direct mechanical mechanism of signal modulation involving CasL.

5.2 Materials and methods

5.2.1 Animals

AND X B10.BR transgenic mice (Jackson Laboratory), of both genders and of age between 6–16 weeks, were used as CD4+ cell donors. Mice were housed in a facility certified by AWRC, under continuous veterinary animal care with adequate water, food and comfort. Only AWRC veterinary certified researchers, who have passed specific animal handling tests for the procedure, were allowed to handle the mice.

5.2.2 CD4+ cell harvest

The procedure was performed in accordance with the American Veterinary Medical Association (AVMA) Guidelines on Euthanasia. Mice were first euthanized with carbon dioxide. Cervical dislocation was performed at least 5 minutes after euthanasia to minimize pain to the mice. Mice were sterilized with 70% ethanol prior to the harvest of lymph nodes and spleen. AND CD4+ T cells were expanded to T cell blasts after harvest and maintained as previously described[53,80].

5.2.3 DNA constructs

A plasmid containing enhanced green fluorescent protein fused to the calponin homology domain of utrophin (EGFP-UtrCH)[77] was a gift of Dr. William Bement, University of Wisconsin, Madison, WI. The EGFP-UtrCH coding sequence was amplified using PCR and subcloned into a murine stem cell virus plasmid (pMSCV-Puro). A plasmid containing EGFP fused to the heavy chain of human non-muscle myosin IIA (EGFP-NMHCIIA) was provided by Dr. Robert Adelstein, National Institutes of Health, Bethesda, MD through Addgene.org (Addgene plasmid 11347)[125], and the EGFP-NMHCIIA coding sequence was subcloned into pMSCV-Puro plasmid.

5.2.4 Reagents

Histidine-tagged ICAM-1 and MHC Class II I-E^K were expressed and purified as previously described[53,87]. Briefly, secreted ICAM-1 with a decahistidine tag at its C terminus (a gift of Dr. Mark Davis, Stanford University) was expressed using the baculovirus expression system in High Five cells (Invitrogen) and purified using a Ni^{2+}-NTA-agarose column (Qiagen). Secreted MHC with a hexahistidine tag at the C terminus of both α and β chains was similarly expressed and purified from S2 cells. Blebbistatin, ML-7 and jasplakinolide were purchased from EMD Chemicals. ZAP-70 (Tyr319) antibody and p130Cas (pY165) antibody were purchased from Cell Signaling.

5.2.5 Retroviral transfection

T cells were retrovirally transduced using supernatants derived from cultures of Phoenix cells as previously described[78]. Briefly, Phoenix cells were transfected with pMSCV-Puro-EGFP-UtrCH or pMSCV-Puro-EGFP-NMHCIIA immediately prior to T cell

harvest using the calcium phosphate method. The transfected Phoenix cells were cultured in T cell medium starting 24 hours after transfection and T cell harvest. Two days after transfection and T cell harvest, T cells were spun down, resuspended in supernatant collected from the Phoenix cell cultures, and spun at 2500 min^{-1} for 1 hr to encourage uptake of virus. T cells were selected in fresh medium containing 0.5 μg/ml puromycin 3 days after harvest and were allowed to recover from selection in fresh medium 5 days after harvest. They were used for imaging experiments starting from day 7 after cell culture.

5.2.6 Bilayer assembly and cell imaging

Moth cytochrome *c* 88–103 peptide (MCC, ANERADLIAYLKQATK) (Biosynthesis and the Dana-Farber Core Facility) was loaded onto the I-E^K protein overnight. Glass-supported lipid bilayers comprised of 98 mol% 1,2-dioleoyl-sn-glycero-3-phosphocholine (DOPC) and 2 mol% 1,2-dioleoyl-sn-glycero-3-[(N-(5-amino-1-carboxypentyl)iminodiacetic acid) succinyl] (nickel salt) (Ni^{2+}-NTA-DOGS) (Avanti Lipids) were prepared in flow chambers by standard methods[46,53,103]. Bilayers were loaded with ICAM-1 and pMHC by incubation at room temperature for 40 minutes. To label the T cell receptors, the non-blocking antibody H57 αTCR-Fab (conjugated to Alexa Fluor 594 or Alexa Fluor 643 as indicated) was incubated with T cells at 4°C for 20 min. To inhibit myosin or actin depolymerization, cells were then incubated with 100 μM blebbistatin, 20 μM ML-7 or 1 μM jasplakinolide at 37°C for 15 min before imaging. Inhibitors used at the indicated concentrations have been shown to effectively inhibit functions of their target proteins[59,126,127]. For fixed cell experiments, cells were injected into a sample chamber preheated to 37°C and allowed to interact with the bilayer for the indicated time. Cells were then fixed with 2% paraformaldehyde, permeabilized with 0.05% Triton X, blocked with 5% casein and labeled with antibodies at room temperature or as otherwise indicated. To label pZAP-70, fixed cells were incubated with anti-pZAP-70 IgG against Tyr319 (Cell Signaling) at 4°C overnight and then with Alexa Fluor-488 conjugated goat anti-rabbit IgG (Invitrogen) at room temperature for 20 min. Because the YxxP motifs are highly conserved between CasL and p130Cas, the YxxP motifs of CasL were labeled with p130Cas (pY165) antibody (Cell Signaling). Total internal reflection fluorescence (TIRF) microscopy images were acquired on a Nikon Ti-E/B inverted microscope with a 100× 1.49 NA oil immersion TIRF objective and an Andor iXon EMCCD camera. Images of phosphorylated pZAP70 or pCasL of different samples were acquired under the exact same settings for lasers, camera, and microscope; the angle of the input laser was also kept consistent throughout imaging under the control of a motorized laser TIRF illumination unit (Nikon) and the focus on the glass substrate was maintained by a Perfect Focus System (Nikon).

5.2.7 Calcium imaging

T cells were firstly incubated with 1 μM Fura-2-acetoxymethyl ester (Fura-2 AM) in serum-free cell media at room temperature for 15 minutes and then in Fura-2 free serum-rich media at 37°C for 20 minutes. After TCR labeling, cells were incubated with DMSO or 20 μM ML-7 at 37°C for 15 min before being injected into the imaging

chamber. Images were acquired on a Nikon TE 2000 microscope with a 40× S Fluor objective (Nikon) and a Coolsnap K4 camera (Roper Scientific). Emission at 510 nm was captured by alternating the excitation wavelength between 340 and 380 nm. The ratiometric value of the Fura-2 AM dye, indicating relative intracellular calcium levels, was obtained by using the program Imaris (Bitplane) and a custom Matlab algorithm.

5.2.8 Speckle tracking and image analysis

The custom speckle tracking algorithm as described previously[17,18], was used to identify the locations of speckles based on the fluorescent intensity gradient within the images. Following identification, nearest neighbors of speckles in consecutive frames were linked to generate trajectories. The position- and time- averaged radial velocities of the speckles relative to the defined cell center were then analyzed. Time-averaged radial velocity $<V(t)>$ was obtained by averaging the radial velocities of all microclusters located at the cell periphery during $(t, t+\Delta t)$, where t is the elapsed time after the initial cell-bilayer contact and Δt = 10 sec. The object-based colocalization algorithm contains two major steps: cluster identification and pairwise cluster matching between two fluorescent channels. The fluorescent clusters were firstly identified by the speckle tracking algorithm. The microclusters in two fluorescent channels are considered as colocalized if their center distance is within the diffraction limit (200 nm). TCRs accumulated in the cSMAC area were excluded from the analysis for control cells at 5 min due to their distinct signaling properties and the absence of ZAP-70 in this region[24]. The cSMAC region was outlined based on the higher fluorescence intensity by applying an imaging threshold calculated from Otsu's algorithm[128]. For the direct comparison of the phosphorylation level of pZAP-70 or pCasL between different samples, analysis was done in multiple steps. (1) Cells were first selected manually and outlined in each image. (2) Fluorescence intensities of all pixels at each cell-bilayer contact area were summed and an averaged fluorescence intensity per cell (I_{ave}) subtracted by background was obtained. (3) I_{ave} of each sample was then normalized to that of the control.

5.3 Results

5.3.1 Myosin IIA transiently drives translocation of TCR microclusters

During antigen recognition, TCR-pMHC complexes undergo a series of spatial translocations including: local clustering and long range transport to the center of the IS[23,24,67,68,122]. To explore the role of myosin IIA in these steps, we imaged fluorescently labeled TCRs at the cell-bilayer interface and tracked their movements with a custom tracking algorithm that implements an intensity gradient method to find centers of non-spherical fluorescent objects. Essentially, the entire ensemble of TCR microclusters within each individual cell (~100 microclusters) was imaged and tracked with ~50 nm spatial resolution and ~50 ms temporal resolution over the course of IS formation. In control cells, TCR trajectories reveal coordinated centripetal movement in pSMAC region and the cell periphery following the initial cell-bilayer contact, but more confined motion at the center (cSMAC) (Figure 5.1A). Pharmacological inhibition of myosin IIA by

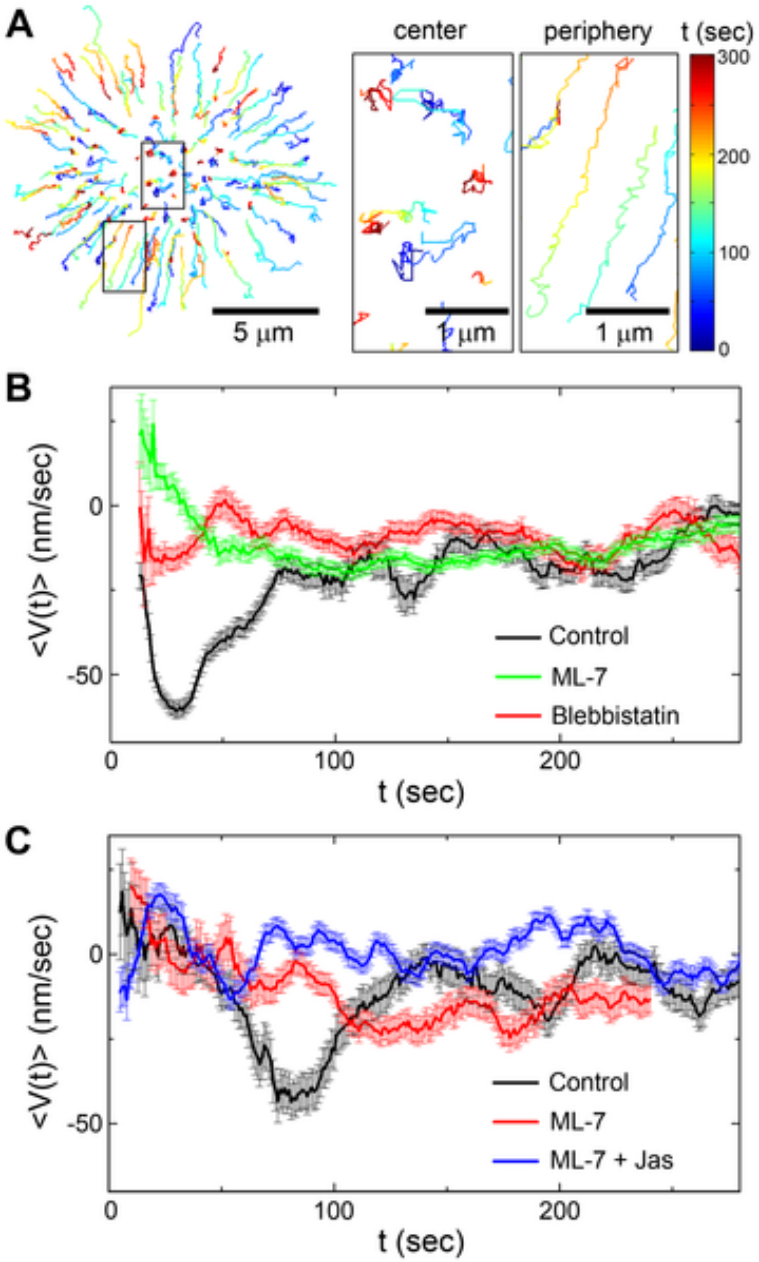


Figure 5.1. Myosin IIA transiently drives TCR translocation and actin retrograde flow in immunological synapse formation. T cell receptors (TCRs) were labeled with H57 αTCR Fab (Alexa Fluor dyes) and imaged starting from the initial cell-bilayer contact (t = 0 sec). (**A**) Trajectories of all TCR microclusters (Alexa Fluor 594) show their centripetal movement at the cell periphery and highly confined motion at the central area of the immunological synapse. Color bar corresponds to the elapsed time after the initial cell-bilayer contact. Data are representative of 6 independent experiments. (**B**) Inhibition of myosin IIA changes the time-dependence of TCR microcluster translocation. Time-averaged radial velocities (<V(t)>) of TCRs (Alexa Fluor 643) in individual cells are plotted against the elapsed time after the initial cell-bilayer contact in the presence of DMSO control, blebbistatin, or ML-7. Data are representative of 5 independent experiments. (**C**) Inhibition of myosin IIA changes the time-dependence of actin retrograde flow during the immunological synapse formation. Time-averaged radial velocities (<V(t)>) of tracked EGFP-UtrCH in individual cells are plotted against the elapsed time after the initial cell-bilayer contact in the presence of DMSO control, ML-7, or ML7 with jasplakinolide. Data are representative of 4 independent experiments. Error bars in (**B**) and (**C**) represent standard errors.

blebbistatin (100 μM) and ML-7 (20 μM) does not alter the clustering of TCRs, but leads to much less directed motion of the microclusters (Figure S1 in the associated manuscript[21]). For a more quantitative measure, we analyzed the time-dependence of TCR translocation during IS formation. Averaged radial velocities, <V(t)>, are plotted against time, t, on a single cell basis. <V(t)> is defined negative for centripetal movements and positive for movements toward the cell periphery. In control cells, translocation of TCR microclusters varies significantly as IS formation proceeds (Figure 5.1B). After the initial cell-bilayer contact (t = 0 sec) microclusters undergo very rapid centripetal movement ($\langle V(t)\rangle_{max} \approx -70$ nm/sec) for approximately 2 min and then maintain a reduced yet constant speed ($\langle V(t)\rangle \approx -15$ nm/sec) for an additional 3–5 min

until the central accumulation of TCRs stabilizes. By contrast, TCR microclusters in cells pretreated with blebbistatin or ML-7 do not exhibit the rapid initial centripetal movement, but move at an almost constant velocity (<V(*t*)>≈−10 to −15 nm/sec) throughout the entire time course of IS formation (Figure 5.1B). The loss of the initial rapid component of centripetal movement indicates that myosin IIA is transiently involved in TCR transport and the slower movement in the presence of myosin inhibitors suggests a secondary driving force, presumably actin polymerization. In control experiments in which we simultaneously imaged TCR translocation and cell edge movement, we confirm that TCR microclusters, which move almost one order of magnitude faster than the cell membrane contraction (−5 nm/sec), are actively driven by forces from myosin IIA instead of the global cell movement (Figure S2 in the associated manuscript[21]).

Next, we quantified the effect of myosin IIA on actin retrograde flow during IS formation by imaging and tracking actin labeled with the calponin homology domain of utrophin fused to EGFP (EGFP-UtrCH)[18,77]. Myosin IIA is known to exert contractile forces on the actin cytoskeleton for various cellular functions[54,129–131]. In agreement with previous reports[14], the flow of actin in control cells shows the same time-dependence as that of TCR microclusters: a rapid centripetal flow followed by a persistent and slower flow (Figure 5.1C and Figure S3 in the associated manuscript[21]). Similar to the effect of myosin inhibition on TCR translocation, actin flow in cells pretreated with ML-7 exhibits only a constant velocity of ≈−10 nm/sec. Blebbistatin was not used here due to its photoinactivation by short wavelength light[132]. Results from both TCR movement and actin flow indicate that myosin IIA transiently contributes to actin retrograde flow and, correspondingly, TCR transport during early times of IS formation. In T cells treated with both ML-7 (20 μM) and jasplakinolide (1 μM), a pharmacological agent to prevent actin depolymerization, actin retrograde flow is completely abrogated (Figure 5.1C). Therefore, actin polymerization provides a long-lasting driving force that operates in superposition to the more transient contribution from myosin.

The role of myosin IIA in IS formation has been controversial in previous studies[58,62,63]. Since our fluorescence tracking data suggests that TCR microclusters are able to translocate in the absence of myosin IIA, we studied whether myosin is required for the spatial organization at the IS. TCR and ICAM-1 in control cells exhibit the characteristic “bull's eye” pattern, where the TCR microclusters accumulate at the center while LFA-1 bound to ICAM-1 localizes at the periphery (Figure 5.2). Inhibition of myosin leads to a more dispersed distribution of TCR microclusters in cells fixed at 3 min after stimulation, but the difference becomes negligible when cells are fixed at 10 min (Figure 5.2 and Figure S4 in the associated manuscript[21]). The overall ring-like distribution of ICAM-1 in the pSMAC is not affected by myosin inhibition. This demonstrates that myosin IIA influences the time frame of IS formation, but is not required for the superficial appearance of the final pattern. It is important to recognize that these observations do not suggest that the cells arrive at the same final state with and without myosin, as detailed below. Rather, it reveals that the large scale spatial organization of the IS probably offers insufficient information from which to judge the more subtle internal state of the cell.

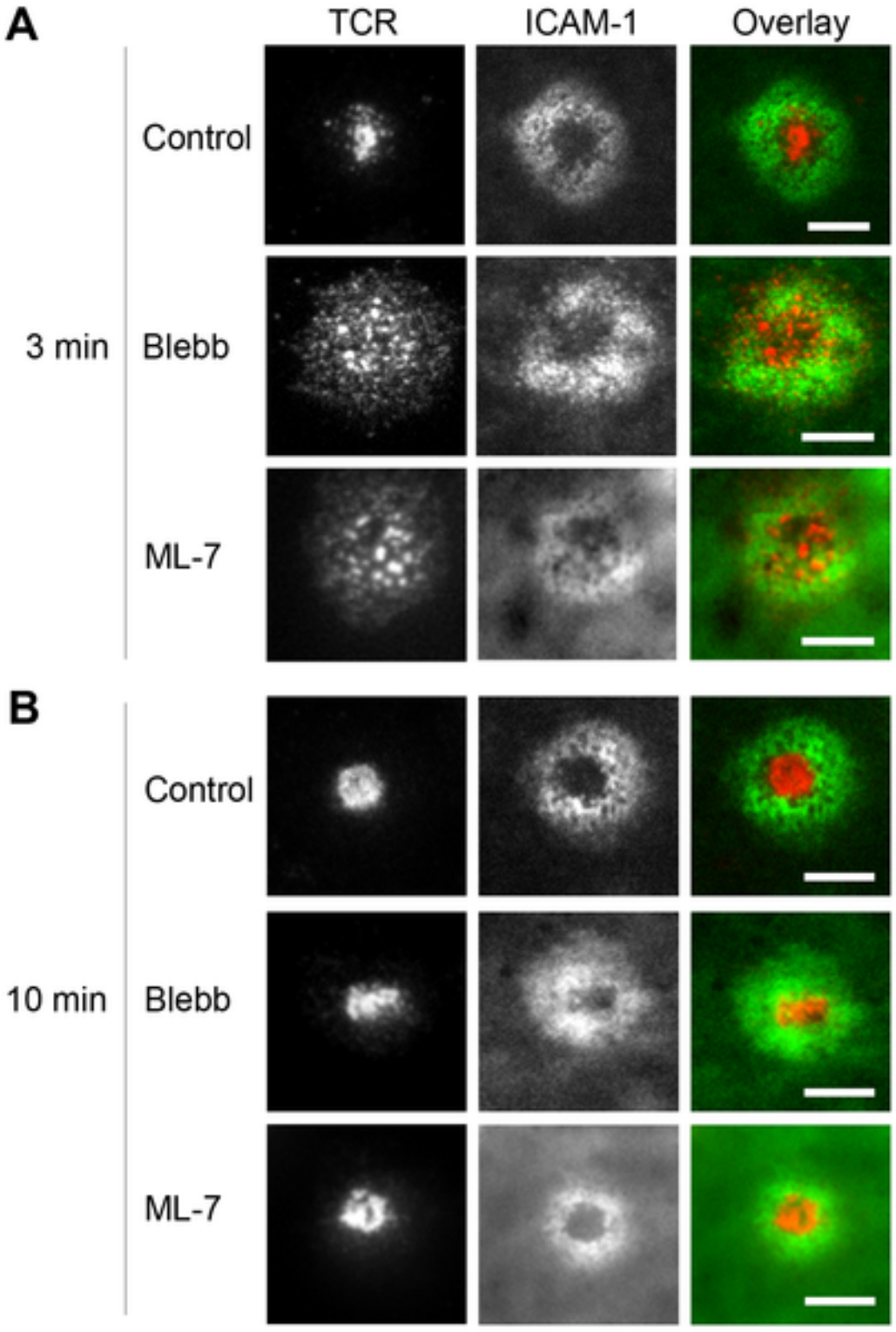


Figure 5.2. Inhibition of myosin only affects morphology of the early immunological synapse. Total internal reflection fluorescence (TIRF) images of TCRs labeled with H57 αTCR Fab (Alexa Fluor 594) and ICAM-1 (Alexa Fluor 488) are shown. Cells were pretreated with DMSO, blebbistatin, or ML-7, and fixed at (**A**) 3 min and (**B**) 10 min after interacting with bilayers. Data are representative of 3 independent experiments. Scale bars: 5 μm.

5.3.2 Forces applied to TCR clusters are translated to myosin IIA

Our results above have shown that myosin IIA transports TCR microclusters by driving actin retrograde flow. To further explore the mechanical link between myosin and TCR, we quantified if physical forces on TCR clusters can be transmitted to influence myosin. We formed lipid bilayers on substrates patterned with metal grids, which create barriers to lateral mobility of membrane-tethered pMHC and ICAM-1. Because patterned bilayers retain their fluidity[17,18,45,53,76], TCRs engaged with the constrained pMHC are trapped by the metal grids and experience passive opposing forces from the barriers that prevent their centripetal movement. As shown in Figure 5.3A, the adhesion of T cells and local clustering of TCRs remain unchanged on the patterned lipid bilayers, but TCR centripetal translocation is blocked by the metal barriers. The question, then, is how this physical trapping of TCR clusters affects myosin, which is itself not directly influenced by the substrate-imposed patterns. By plotting the radial velocity (<V(*t*)>)

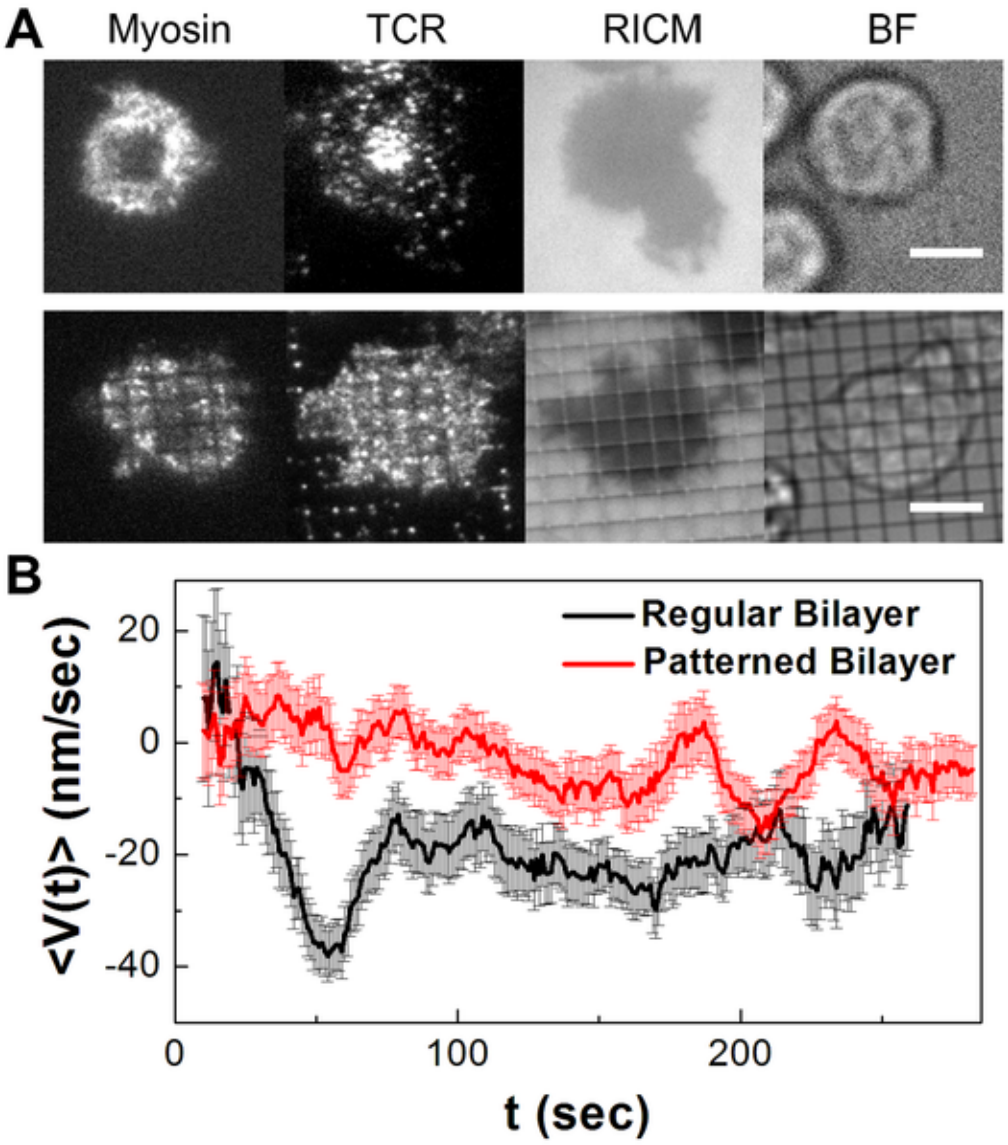


Figure 5.3. Physical constraints on TCR microcluster translocation impede myosin IIA movements. (**A**) TIRF, reflection interference contrast microscopy (RICM), and bright field (BF) images of T cells expressing EGFP-myosin on unpatterned or patterned bilayers. Scale bars: 5 μm. (**B**) Time-averaged radial velocities (<V(*t*)>) of EGFP-myosin in individual cells are plotted against the elapsed time (*t*) after the initial cell-bilayer contact (*t* = 0). Data are representative of 2 independent experiments.

against time (*t*), we observed that myosin exhibits similar time-dependent motion as that of TCR and actin on non-patterned lipid bilayers. However, on a patterned bilayer where TCR microclusters are hindered from moving past the metal line grids, the centripetal movement of myosin IIA at earlier times is significantly reduced (Figure 5.3B). By performing the same experiments on actin, we also observed that actin retrograde flow decreases on the patterned lipid bilayers consistently with myosin (Figure S5 in the associated manuscript[21]). The slow-down of myosin in response to physically constrained TCRs confirms the existence of a mechanical coupling between TCR and myosin. Moreover, because contractile forces in actin are generated by myosin and studies have shown that resistive load on non-muscle myosin IIA leads to its slower power stokes on actin[133], the reduced actin retrograde flow on pattern lipid bilayers points to actin cytoskeleton as responsible for transmitting the resisting force from TCR microclusters to myosin.

5.3.3 Myosin IIA is required for Ca^{2+} influx

A hallmark of T cell activation downstream of TCR signaling is the elevation of intracellular calcium, which in turn activates a number of calcium-dependent

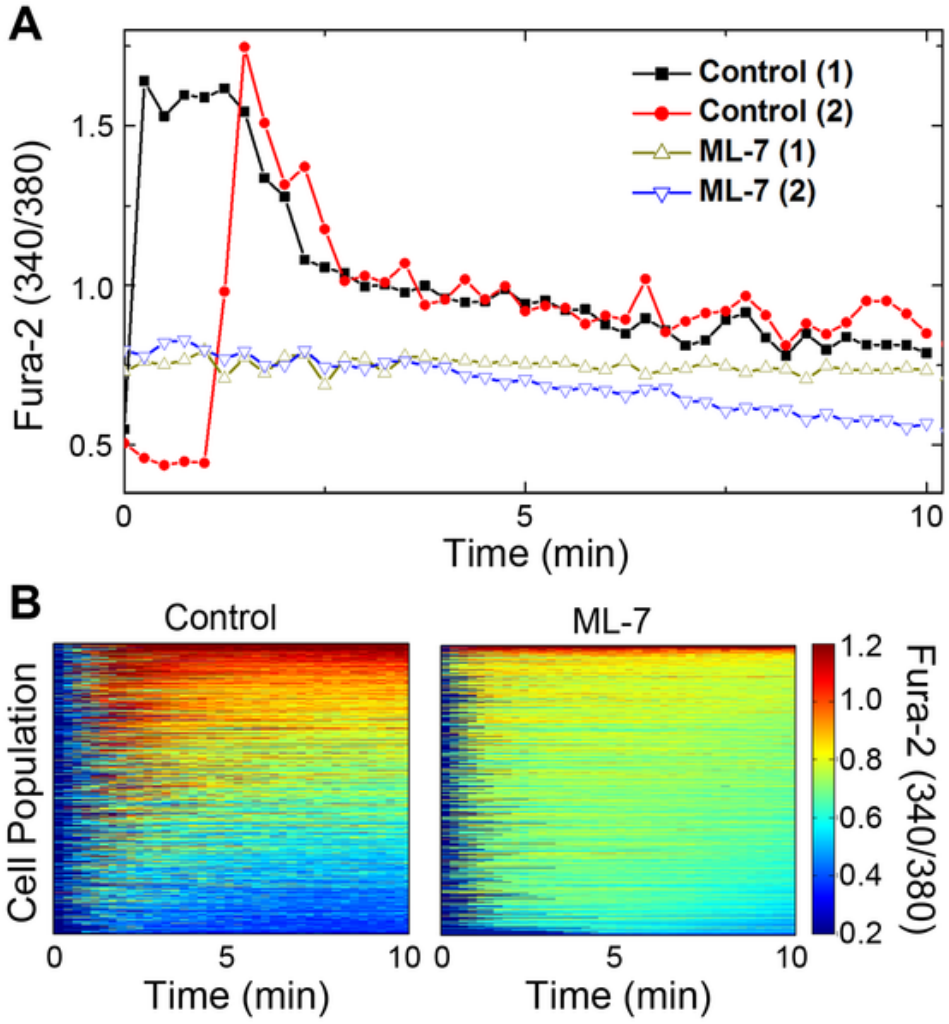


Figure 5.4. Inhibition of myosin IIA abolishes intracellular Ca^{2+} influx. The ratio of Fura-2 fluorescence emission intensity in response to 340 nm and 380 nm excitation (340/380) is proportional to intracellular [Ca^{2+}]. (**A**) Fura-2 340/380 emission ratios are plotted against the cell stimulation time for four representative cells pretreated with either DMSO or ML-7. (**B**) Fura-2 340/380 emission ratios of control cells (n = 1602) and cells pretreated with ML-7 (n = 2187) are plotted against time on a color scale and organized along the *y*-axis according to the summed calcium influx.

pathways[134]. We used Fura-2 as the indicator of intracellular calcium concentration; the ratio of its emission intensities at 340 nm excitation versus 380 nm is proportional to Ca^{2+} concentration. In control cells, intracellular Ca^{2+} concentration rapidly increases within 1 min after the initial cell-bilayer contact. By contrast, cells pretreated with ML-7 do not show any significant Ca^{2+} elevation, but maintain a low Ca^{2+} level similar to baseline (Figure 5.4A). The Ca^{2+} concentration traces of a large population of both control cells and cells pretreated with ML-7 show a dramatic reduction in the calcium influx in response to myosin IIA inhibition (Figure 5.4B). In agreement with previous work on Jurkat cells[63], the results show that myosin IIA is important for calcium signaling in primary T cells.

5.3.4 Inhibition of myosin IIA reduces association of active ZAP-70 with TCR

T cell signaling is initiated in discrete TCR microclusters, and association of kinases and adaptor proteins with the microclusters is a key step of sustaining the signaling reaction[23,24,40,69,134]. Upon TCR engagement to pMHC, ZAP-70 is recruited to the CD3 zeta chain and phosphorylated on tyrosine 319 (pZAP-70) for downstream signaling. To understand the role of myosin IIA in initiation of TCR signaling, we used ZAP-70 as a quantitative readout of TCR/CD3 signaling and quantified how myosin inhibition influences colocalization of pZAP-70 with TCR using an object-based colocalization algorithm. Unlike many intensity-based colocalization algorithms[135], this analysis avoids bias due to the variation in fluorescence intensities between TCR microclusters (Figure 5.5B). In control cells, pZAP-70 localizes mainly on the cell periphery and its colocalization with TCR decreases with stimulation time (Figure 5.5A and C, Figure S6 in the associated manuscript[21]). Inhibition of myosin IIA results in less colocalization of TCR microclusters with pZAP-70 in T cells fixed at both 1.5 min and 5 min after stimulation, but not at 45 sec (Figure 5.5C). The phosphorylation level of ZAP-70 at the IS also decreases in the absence of myosin function (Figure 5.5D). Myosin IIA therefore contributes to the stable association of active ZAP-70 with TCR, but it is not necessary for the initial recruitment.

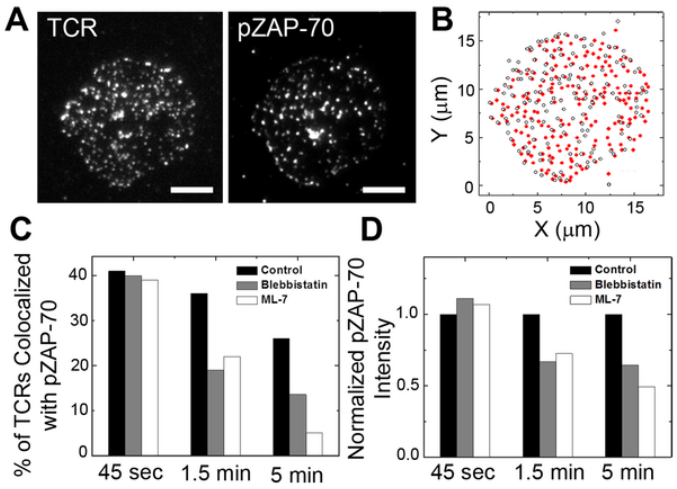


Figure 5.5. Inhibition of myosin IIA reduces phosphorylation of ZAP-70 and colocalization of pZAP-70 with TCR microclusters. (**A**) TIRF images of TCR and pZAP-70 (pY319) from a T cell fixed at 1.5 min. (**B**) Object-based colocalization analysis identifies TCRs and pZAP-70 in the T cell in panel (**A**). (**C**) The percentages of TCR microclusters colocalized with pZAP-70 are shown for the indicated stimulation times prior to fixation. (**D**) Fluorescence intensities of pZAP-70 in IS are shown normalized to those in control cells. Each column in panel (**C**) and (**D**) is an averaged value from approximately 200–300 cells. Data were reproduced in 2 independent experiments. Scale bars: 5 μm.

5.3.5 Inhibition of myosin IIA reduces CasL phosphorylation

To our knowledge, there have been no previous studies directly quantifying the cytoskeletal strain in T cells and correlating this to TCR signaling. The data we report above and other published results clearly indicate at least an indirect influence of myosin IIA on TCR signaling, but the role of its mechanical forces in the process still remains unclear. To explore that question we studied the phosphorylation of CasL. It is a member of the mechanosensing Cas protein family and is predominately expressed in T lymphocytes[136–139]. All Cas family proteins contain a highly conserved Src kinase substrate domain, which is consisted of multiple Tyr-x-x-Pro (YxxP) motifs. Studies on p130Cas, one of the Cas proteins, have shown that mechanical stretching changes conformation of the motifs and leads to enhancement of tyrosine phosphorylation and possibly downstream signaling[140]. Whether or not CasL is involved in molecular force transduction is less clear, but its phosphorylation level strongly depends on actin integrity in several cell types[141–143], suggesting that CasL might also function as a mechanosensor. Therefore, we investigated if CasL plays a possible role to transduce myosin contractile forces to modulate TCR signaling.

We quantified the phosphorylation of CasL by using a phosphorylation-specific antibody against its YxxP motifs and measuring the fluorescence intensity of secondary antibodies at the IS. It has been previously reported that either TCR or integrin crosslinking leads to CasL phosphorylation through possibly independent signaling pathways, and that the phosphorylation level upon TCR ligation peaks transiently within the first 5 min after stimulation while integrin crosslinking results in a later but more long-lasting phosphorylation[136]. Because our entire study here focuses on the early events of T cell signaling as well as the relevance between TCR and myosin, only pMHC was present in the supported lipid bilayer to exclude the potential influence of integrin signaling pathways on CasL function. While the nature of the IS is somewhat

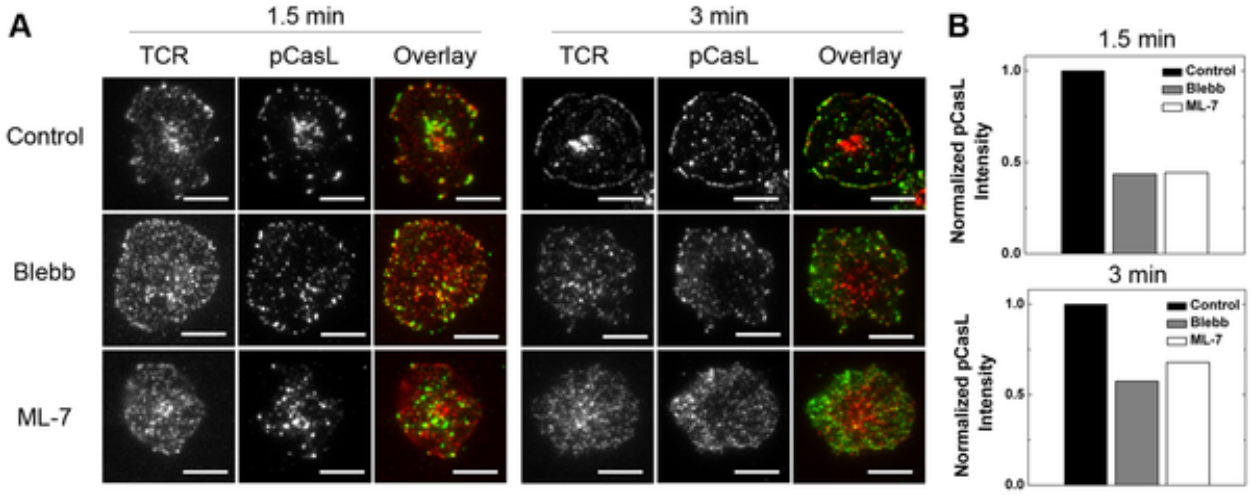


Figure 5.6. Inhibition of myosin IIA reduces phosphorylation of CasL. (**A**) TIRF images of TCR and pCasL from T cells fixed at 1.5 min and 3 min and pretreated with DMSO (control), blebbistatin or ML-7. (**B**) Fluorescence intensities of pCasL in IS are shown normalized to those in control cells. Each column in Panel (**A**) and (**B**) is an averaged value from approximately 200 cells. Data were reproduced in 2 independent experiments. Scale bars: 5 μm.

different without ICAM-LFA interactions, T cells can adhere and be normally activated by bilayer-tethered pMHC alone[38]. As shown in Figure 5.6A, phosphorylated CasL (pCasL) in control cells colocalizes with TCR microclusters across the entire IS at 1.5 min after stimulation. However, at a later time point (t = 3 min), pCasL is absent from the cSMAC region but still colocalizes with the discrete TCR microclusters on the cell periphery. Inhibition of myosin IIA has negligible effects on colocalization of TCR microclusters with pCasL, quantified by using the object-based colocalization analysis (Figure S7 in the associated manuscript[21]). However, immunofluorescence quantification of pCasL at the IS shows significantly reduced phosphorylation of CasL by myosin inhibition at both 1.5 min and 3 min after stimulation (Figure 5.6B).

5.4 Discussion

It is increasingly clear that the ability of cells to sense, interpret, and respond to mechanical signals plays a critical role in modulating diverse cellular functions, such as proliferation, migration, differentiation and homeostasis[144–147]. While integrins are the well-known force transducers in cells, recent data suggest that membrane receptors that are not directly associated with focal adhesions may also couple into force sensing roles, at least indirectly[90]. In T cells, the concept of force sensing is not well established although a number of recent studies have suggested the idea of mechanosensing in T cell activation[33–35]. We suggest that an indirect role for force in TCR signaling is all but guaranteed by the known significance of spatial organization in this system[17,18,45,46,53,103,123]. Any applied force that changes protein spatial organization in a manner to impact signaling reactions affords an indirect force response to the system. The resulted signaling, however, may be either reduced or enhanced depending on the exact mechanism. Previous studies have reported that impeded translocation of TCR microclusters leads to enhanced signaling, likely due to attenuated signal degradation at cSMAC[40,53,66]. By contrast, our results, in agreement with a previous study[63], suggest that inhibition of myosin leads to slower TCR transport and diminishes signaling. The bigger question is whether force from myosin plays a direct role in the modulation of TCR signaling. Although actin, microtubule, and some molecular motors have all been shown to play important mechanical roles in T cell signaling[14,23,62,63,66], they are unlikely to directly transduce mechanical forces into biochemical signaling cascades. Our observation of a decrease in CasL phosphorylation in response to myosin inhibition suggests that CasL may be involved in a mechanical signal transduction process in T cells. While working out details of the possible regulatory pathways is well beyond the scope of this paper, CasL is clearly a candidate for relating myosin to TCR signaling pathways. Studies have shown that CasL may be a substrate for Fyn and Lck, two key tyrosine kinases in initiating TCR activation[139]. Phosphorylated CasL can also bind to Src homology (SH) domains of signaling proteins, such as Crk, Cbl, and nucleotide exchange protein C3G, to regulate T cell signaling[148,149]. We observed the phosphorylation of CasL upon TCR ligation and its association with discrete TCR microclusters at the IS. Our results of calcium influx, ZAP-70 phosphorylation, and TCR microcluster formation all suggest that myosin is more important for sustained signaling than initiation. CasL might be involved in a feedback loop between myosin and multiple signaling pathways. While much remains to be uncovered concerning the nature of

mechanical influences on TCR activation, our observation of differential CasL phosphorylation with myosin inhibition clearly pinpoints a starting point to look into.

Chapter 6

Patterned two-photon photoactivation illuminates spatial reorganization in live cells

*The work presented in this chapter has been previously published as part of the following paper: Smith, A.W., Smoligovets, A.A., and Groves, J.T. Patterned Two-Photon Photoactivation Illuminates Spatial Reorganization in Live Cells. *J. Physical Chemistry A*, 115, 3867-3875 (2011).

*Adam Smith conceived the experiments, performed microscopy, analyzed and interpreted data, and wrote the manuscript. Alexander Smoligovets prepared necessary materials and reagents, cultured cells, performed the experiments, and wrote sections of the manuscript.

6.1 Introduction

Molecular movements in cells do not conform to simple diffusion laws. Within the cell, molecules are synthesized, trafficked, and degraded at high turnover rates. In addition, high molecular densities lead to crowding effects that hinder protein diffusion and create a need for actively driven transport mechanisms. Because trafficking of materials and signals within cells is actively regulated, following their dynamics requires a detailed description of spatial distributions over time. We report a method to track a spatially defined population of molecules as it redistributes within the cell. A matrix decomposition algorithm is used to analyze a series of time-lapse images that are taken after photoactivating a user-defined region of the cell. With this method we describe the time-evolution of patterned distributions of actin within the dense cytoskeletal network of live cells.

Recently developed photoactivatable fluorescent proteins offer the possibility to optically tag and track the location of molecules in their bright state with high spatial and temporal resolution[150,151]. With two-photon photoactivation it is possible to activate spatial distributions of these molecules within volumes limited to hundreds of nanometers in the lateral dimension and close to one micrometer in the axial dimension. Two-photon photoactivation allows for smaller photoactivation patterns in the axial and lateral dimensions compared to one-photon photoactivation because two-photon absorption depends on the square of the input power. Several studies using two-photon patterned photoactivation have been produced since the development of a photoactivatable variant of the green fluorescent protein (PaGFP) and the demonstration of two-photon activation of PaGFP[152,153]. For example, tissue-level protein migration has been observed by photoactivating a pool of PaGFP in targeted cells[154,155]. In single cells, small regions have been photoactivated to follow nucleocytoplasmic transport[156,157] and chromatin mobility within nuclear compartments[158]. The dynamics of the photoactivated pool of fluorophores are typically analyzed using intensity variations away from the photoactivation region. This is similar to the analysis of photobleaching experiments, but instead of monitoring fluorescence recovery after photobleaching (FRAP), the experiments monitor fluorescence migration after photoactivation. While analyzing simple intensity variations may be useful for following transport in and out of organelles and from cell to cell, it is not ideal for mapping spatial distributions for which the directionality and flow rates may not be homogeneous across the cell. Here we report on the use of singular value decomposition (SVD) to track the time-dependent distribution of fluorophores after photoactivation. SVD allows for a quantitative description of spatial reorganization without reducing the data to a raw intensity decay and without the need to fit the spatial distribution to a predetermined functional form.

SVD is a matrix algebra operation that is used to treat multivariate data[159–161] by decomposing a data matrix into basis states and weighting coefficients. For a time-dependent set of data, each measurement in time can be reconstructed as a linear combination of the basis states with the corresponding set of time-dependent coefficients. The advantage of SVD is that the weighting coefficients can be used to find so-called high ranking basis states that make the largest contributions to the data set. The high ranking basis states can then be used to identify the dominant changes to the

data over time. In this way, SVD functions analogously to a Fourier analysis in that it can be used to remove low-frequency noise from the data. Furthermore, the time-dependent weighting coefficients for the high-ranking basis states can be used to assign rates to the processes represented by those basis states. In our results below, the first and second SVD basis states dominate the time-dependent data set, accounting for over 99% of the intensity. The first component state is highly similar to the time average of the original data, while the profile of the second component state resembles the difference between the data at the first time point and a later time point. The rates of change to the amplitude of the two components are used to describe the time-dependent distribution of a photoactivated ensemble of molecules.

In this work we apply the above methodology to study the actin cytoskeleton of living cells. The dynamics of the actin network are a complex interplay of polymerization and depolymerization rates in feedback with other cellular functions. Cytoskeleton dynamics play an important role in cell function and are sensitive to the biological state of the cell. For this study, cells were transfected with PaGFP fused to the F-actin binding calponin homology domain of utrophin (UtrCH). Photoactivation patterns were written in each sample with a pair of galvanometric scanning mirrors that position the laser focus with accuracy approaching the diffraction limit at the image plane and pixel dwell times as fast as 100 μs. Photoactivation was localized to the cortex of the cell near the substrate, and photoactivated proteins were tracked using time-lapse total internal reflection fluorescence (TIRF) microscopy. Several mechanisms redistribute the bright fluorophores throughout the cell including diffusion of unbound fluorophores, fragmentation and regeneration of the cytoskeleton, and migration of the polymer network. These multiple mechanisms create the need to use SVD to characterize actin dynamics. For Cos-7 cells we find that the photoactivated fluorophores redistribute isotropically around the pattern region. This process occurs on a 3.8 s time scale indicating a relatively stable network with no net transport as expected for large adherent cells. For antigen-activated T-cells, we find that the actin filaments are highly mobile. Radial transport from the photoactivation region to the center of the cell occurs at a 1.7 s time scale, which is consistent with retrograde cycling[14,162]. The combination of patterned photoactivation and SVD analysis offers a unique way to measure spatial redistribution dynamics within live cells.

6.2 Materials and methods

6.2.1 Microscope

Photoactivation experiments were performed on an inverted microscope (Nikon Eclipse Ti; Technical Instruments, Burlingame, CA) with a custom-built laser scanning attachment. Photoactivation light was produced by an 80 MHz, 100 fs pulsed Titanium:Sapphire laser (Mai Tai HP; Newport Corp, Mountain View, CA) operating at a typical center wavelength of 775 nm. Laser power at the sample was controlled with an electro-optic modulator (350-80LA; Conoptics Inc., Danbury, CT) and was set to between 5 and 20 mW at the sample. An optical breadboard platform was built to access the infinity space of the microscope below the objective. The photoactivation laser was positioned using a pair of galvanometric scanning mirrors (6215H-M40B;

Cambridge Technology Inc., Cambridge, MA) that directed the light through a scan lens (Zeiss EC Plan-Neofluar 2.5x; Edmund Optics Inc., Barrington, NJ) and tube lens (130 mm tube lens; Edmund Optics Inc., Barrington, NJ) positioned as described by Tsai et al[163]. A dichroic beamsplitter (FF670-SDi01-25 × 36; Semrock Inc., Rochester, NY) reflected the light through the objective (Nikon 1.49 N.A. TIRF; Technical Instruments, Burlingame, CA) and allowed >95% transmission from 450 to 690 nm. Exposure times were set in the image collection software (MetaMorph 7.5; Molecular Devices Inc., Downingtown, PA), which drives an external shutter (Uniblitz LS6; Vincent Associates, Rochester, NY). Laser light to the camera was filtered with a short wave pass filter (FF01-680/SP-25; Semrock Inc., Rochester, NY). Because of the intensity requirements for two-photon processes, photoactivation was axially confined to approximately 1−2 μm at the cortical interface between the cell and the substrate[164].

TIRF microscopy was done using a fiber-coupled Nikon TIRF illuminator (Technical Instruments, Burlingame, CA) with a custom-built laser source. The 643 nm (RCL-050-640; Crystalaser, Reno, NV), 561 nm (GCL-100-561; Crystalaser, Reno, NV), and 488 nm (Sapphire HP; Coherent Inc., Santa Clara, CA) lasers were launched into a single mode fiber that was connected to the TIRF illuminator. Excitation powers at the sample were on the order of 1 kW/cm^2. Images were acquired with an EM-CCD (iXon 597DU; Andor Inc., South Windsor, CT). Bandpass emission filters for 488, 561, and 643 nm TIRF images are HQ515/30, ET630/75, and HQ700/75 (Chroma Technology Corp., Bellows Falls, VT), respectively.

6.2.2 DNA constructs

Plasmids containing photoactivatable green fluorescent protein or monomeric red fluorescent protein (mRFP) attached to the calponin homology domain of utrophin (PaGFP-UtrCH or mRFP-UtrCH, respectively) were a gift of William Bement, University of Wisconsin, Madison, WI[77]. A retroviral vector for Phoenix cell transfection (discussed below) and subsequent T-cell transduction was generated by amplifying the PaGFP-UtrCH coding sequence using polymerase chain reaction (PCR) and the primers 5′-AGGATCCTCGAGATGGTGAGCAAGGGCGAGGAGCTGTTCACC-3′ and 5′-AGCTTGGCGGCCGCTTAGTCTATGGTGACTTGCTGAGGTAGCACCTCAAACAAAG ATG-3′ and subcloning the resulting fragment into the XhoI and NotI sites of a murine stem cell virus−internal ribosome entry site−puromycin N-acetyl transferase plasmid.

6.2.3 Phoenix cell culture, transfection, and retrovirion production

Phoenix cells, an HEK 293T-based retroviral packaging cell line[165], were grown in Dulbecco's modification of Eagle's medium (DMEM) supplemented with 10% fetal bovine serum (Atlanta Biologicals Inc., Lawrenceville, GA), 1 mM sodium pyruvate, 2 mM L-glutamine, 100 U/mL of penicillin, and 100 μg/mL streptomycin. On day 1 of the transduction protocol discussed below, Phoenix cells at a confluency of approximately 70% were cotransfected with the target retroviral plasmid and the packaging plasmid pCL-Eco (Imgenex Inc., San Diego, CA) using the calcium phosphate method. At 6 h after transfection, the Phoenix medium was exchanged, and at 24 h (day 2), it was replaced with T-cell medium (RVC, as previously described[45]). The medium containing

retrovirions was collected at 48 h (day 3), when it was replaced with fresh RVC, and at 72 h (day 4).

6.2.4 T-cell culture and transduction

AND CD4+ T-cell blasts were cultured from the lymph nodes and spleens of first generation AND × B10.BR mice on day 1 of the T-cell transduction protocol in accordance with Lawrence Berkeley National Laboratory Animal Welfare and Research Committee-approved protocol 17702. The cells were stimulated with 2 μM moth cytochrome *c* (amino acids 88−103) peptide immediately after harvest. At 24 h after harvest (day 2), 50 U/mL mouse recombinant IL-2 (Roche Applied Science Inc., Indianapolis, IN) was added to the T-cell medium. At 48 h (day 3), the T-cells were pelleted and resuspended in Phoenix cell-derived retroviral supernatant filtered through a 0.45 μm PES syringe filter and supplemented with 50 U/mL IL-2 and 4 μg/mL polybrene. They were then centrifuged at 25 °C and 1328*g* for 1 h and returned to the incubator. At 72 h (day 4), the T-cells were again pelleted, resuspended in filtered and IL-2/polybrene-supplemented retroviral supernatant, centrifuged, and returned to the incubator. At 78 h (day 4), they were pelleted and resuspended in fresh RVC supplemented with 50 U/mL IL-2 and 0.5 μg/mL puromycin. At 120 h (day 6), they were pelleted and resuspended in fresh RVC supplemented with 50 U/mL IL-2. The cells were then used in experiments 168 h after harvest (day 8).

6.2.5 T-cell imaging: preparation of substrates, buffers, and cells

Glass coverslips were etched for 2 to 5 min in piranha etch solution (3:1 H_2SO_4/H_2O_2) and were used in the assembly of FCS2 Closed Chamber Systems (flow cells; Bioptechs Inc., Butler, PA), which were prefilled with Tris-buffered saline (19.98 mM Tris, 136 mM NaCl, pH 7.4; Mediatech Inc., Herndon, VA). Solutions of small unilamellar lipid vesicles (0.5−2.0 mg/mL) were prepared by the sonication or extrusion of evaporated mixtures of 2 mol % Ni^{2+}-DOGS/98 mol % DOPC (Avanti Polar Lipids Inc., Alabaster, AL). The lipid solutions were mixed 1:1 with Tris-buffered saline, injected into the flow cells, and incubated at room temperature for approximately 30 min. The flow cell chambers were then rinsed with Tris-buffered saline, incubated with 100 mM $NiCl_2$ for 5 min, rinsed once with Tris-buffered saline, and then rinsed again with an imaging buffer composed of 1 mM $CaCl_2$, 2 mM $MgCl_2$, 20 mM HEPES, 137 mM NaCl, 5 mM KCl, 0.7 mM Na_2HPO_4, 6 mM d-glucose, and 1% fetal bovine serum (HyClone Inc., Logan, UT), pH 7.3 ± 0.1. Finally, the flow cells were filled with a solution of moth cytochrome *c*-loaded hexahistidine-tagged MHC protein and 30 nM decahistidine-tagged ICAM-1 protein in imaging buffer[46,87], incubated at room temperature for 35 min, and then rinsed with imaging buffer and allowed to equilibrate for a further 35 min. During the final incubation, the flow cells were brought to 37 °C.

T-cells at 168 h after harvest (day 8) were pelleted, resuspended in a solution of 5 μL Alexa Fluor 647 (Invitrogen Inc., Carlsbad, CA)-conjugated H57 anti-TCR antibody fragment (Fab): 100 μL imaging buffer and incubated on ice for 20 min. They were then rinsed with imaging buffer, pelleted, resuspended in imaging buffer, and injected into flow cell chambers upon the completion of the flow cell equilibration. Throughout the T-

cell imaging process, the flow cell chambers were kept at 37 °C, and all images were acquired within 90 min after the cells were injected into the flow cell chambers.

6.2.6 Cos-7 cell culture, transfection, and preparation for imaging

Cos-7 cells were grown in DMEM supplemented with 10% fetal bovine serum (Atlanta Biologicals Inc., Lawrenceville, GA), 1 mM sodium pyruvate, and 2 mM L-glutamine. They were transfected using Lipofectamine 2000 and the associated protocols (Invitrogen Inc., Carlsbad, CA) 48 h after being seeded on 6-well plates at 2.5 × 10^5 cells per well in 2 mL of medium. The Cos-7 medium was exchanged 24 h after transfection, and the cells were imaged 48 h after transfection.

Prior to imaging, piranha-etched glass coverslips were coated in 0.01% (w/v) poly-L-lysine, dried, and used in the assembly of open-top cover glass imaging chambers. Transfected Cos-7 cells were rinsed once with phosphate-buffered saline and then treated with 0.5% phenol red-free trypsin-EDTA for 5 min. Following trypsinization, the cells were rinsed with phenol red-free DMEM, pelleted, resuspended in phenol red-free DMEM, and added to the cover glass chambers. They were then incubated at 37 °C/5% CO_2 for 30 min prior to imaging. For imaging the photoactivation patterns used in SVD analysis, cover glass chambers were kept at 37 °C throughout the measurement, while more complex images of custom photoactivation patterns were acquired with the live cells at room temperature.

For fixed-cell experiments, Cos-7 cells were added to the cover glass chambers and incubated at 37 °C/5% CO_2 as described above. After 30 min, cells were rinsed with phosphate-buffered saline, fixed with 10% formalin (4% formaldehyde; Sigma-Aldrich Corp, St. Louis, MO) for 20 min, and rinsed twice with phosphate-buffered saline. Images were acquired with the fixed cells prewarmed to 37 °C.

6.2.7 Optical patterning

Photoactivation patterns were generated using two different scanning modes. In the first, the mirrors were scanned continuously using the output of a waveform generator. In Figure 6.1B, for example, the drive voltage to each mirror was scanned from −60 to 60 mV using a 1 kHz sine wave with a 90° phase between the mirrors. The total photoactivation time was controlled with an external laser shutter timed with the camera acquisition. Exposure times varied across experiments but ranged between 0.1 and 1.5 s so that the pattern was traced on the sample 100 to 1500 times. To create the line shown in Figure 6.1A, only one mirror was scanned using a 1 kHz ramp waveform at ±70 mV.

In the second scanning mode, patterns were written using customized software integrated with the MPScope two-photon imaging package[166]. The software defined a field of view by a minimum and maximum scanning voltage, which was divided into a 512 × 512 grid of pixel positions. The program allowed access to arbitrary pixels at definable dwell times and was limited only by the small angle response time of the galvanometer mirror set (~100 μs). The pattern shown in Figure 6.1H was programmed as a sequential set of pixel positions (285 total pixel positions) with 1 ms pixel dwell times. Total photoactivation exposure times were set to 3−5 times the pattern rate.

When the custom software was used in this modality, it was possible to build arbitrary scan patterns as shown in Figure S1 in the associated manuscript[78], which depicts a cartoon drawing of the green fluorescent protein downloaded from nobelprize.org. The image was made by creating a binary mask from the original JPG file that defined the set of 14855 pixels to be exposed. With 0.1 ms pixel dwell times, the total pattern time was 1.45 s, so that the pattern was traced 5 times during the exposure for Figure S1a. In both of the patterning modalities described above, the lateral photoactivation resolution was consistent with previous work[164]. The line scans in Figure 6.1C showed a full width at half-maximum of 900 nm.

6.3 Results

6.3.1 Patterned photoactivation in cells

To demonstrate the feasibility of visualizing a discrete ensemble of photoactivated proteins within a live cell, we chose to observe the actin cytoskeleton, a highly organized yet dynamic protein network ubiquitous among eukaryotes. There are a number of probes available for visualizing the actin cytoskeleton in live cells, which encompass three broad categories, each with distinct advantages and disadvantages: fluorescently labeled phalloidin, fluorescent G-actin, and labeled actin binding proteins or domains (ABPs)[77,167]. For studying cytoskeletal dynamics, phalloidin, a cell-impermeant F-actin binding small molecule, must be microinjected into live cells, which is laborious and extremely low-throughput[167]. Fluorescent protein (FP)-conjugated G-actin and ABPs can conveniently be genetically encoded to enable higher-throughput data acquisition, but both can also interfere with the cytoskeletal dynamics they are intended to probe. FP-actin fails to rescue actin knockouts in yeast[168], and *Dictyostelium discoideum* cells transfected with FP-actin show significantly altered cell morphology[169], indicating that the fluorescent protein adduct has some effect on wild-type actin function. Indeed, there is evidence that cytoskeletal dynamics measured by FP-actin labeling may not correspond to endogenous values[167]. These defects are typically avoided by the use of FP-ABPs; however, actin binding domains can instead compete with similar domains in endogenous proteins[167,170]. While the overall cell phenotype typically remains much closer to wild-type with FP-ABPs than with FP-actin, one further consideration in their use is that F-actin binding domains may unbind from cytoskeletal filaments, making them potentially more diffusive than FP-actin. Both FP-ABPs and FP-actin can also have separate and distinct incorporation biases for certain cellular actin pools[77,168,171]. To minimize disruption of endogenous actin filament polymerization and depolymerization dynamics, we chose to label the cytoskeleton with a fluorescently labeled probe composed of the calponin homology domain of the actin binding protein utrophin (UtrCH)[77]. This probe robustly labels F-actin in both cellular systems we employed and remains strongly bound to filaments on the time scale of our experiments.

We photopatterned the actin cytoskeleton labeled with PaGFP-UtrCH in live immortalized simian kidney (Cos-7) cells that were seeded onto poly-L-lysine-coated substrates. For each cell, bright field, reflection interference contrast microscopy (RICM), and TIRF images (488 and 561 nm excitation) were acquired before

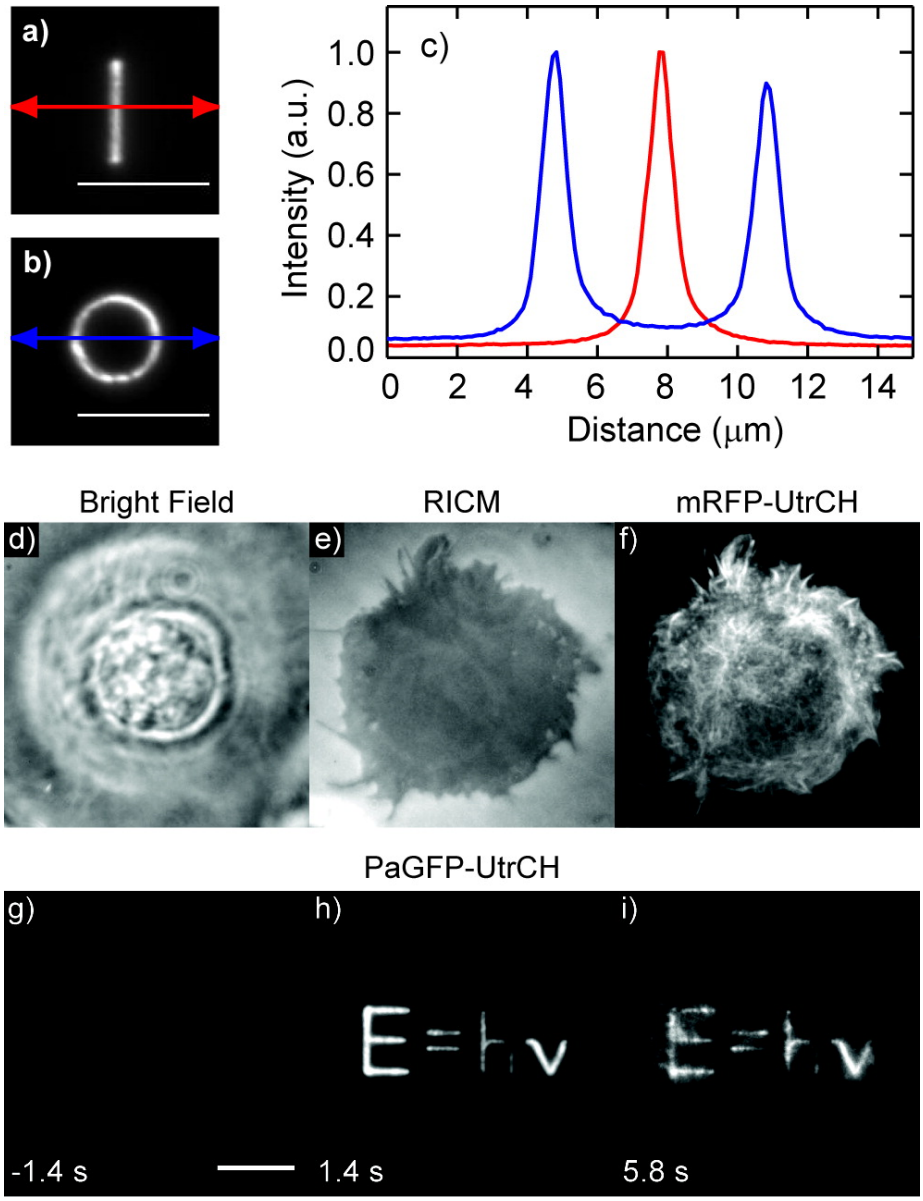


Figure 6.1. (**A,B**) Simple patterns used in live cell experiments. Images are from two-photon excitation during the photoactivation frame. (**A**) Line scan 6.5 μm long. (**B**) Circle scan 3.0 μm radius. (**C**) Image slices shown for circle and line scans. The full width at half of peak maximum is ≈0.9 μm. (**D−I**) Images of a live Cos-7 cell showing fluorescence before and after exposure of the custom photoactivation pattern consisting of 285 pixels scanned at a rate of 1 ms/pixel for 1 s duration. This cell was also transfected with mRFP-UtrCH to highlight the underlying cytoskeleton in the absence of photoactivation. Frames (**D-F**) show bright field (**D**), RICM (**E**), and mRFP-UtrCH 561 nm TIRF (**F**) images. Bottom row shows 488 nm TIRF images at −1.4 (**G**), 1.4 (**H**), and 5.8 s (**I**) after photoactivation. All image scale bars represent 10 μm.

photoactivation. The cell was then exposed to the scanning photoactivation laser, which traced a pattern of arbitrary complexity on the cytoskeleton. Following the photoactivation, a sequence of 488 nm TIRF images was taken at 2 frames per second.

A series of images following the preceding protocol is shown in Figure 6.1D−I. Cos-7 cells are relatively large, adherent cells with extended plasma membrane regions that generate little contrast in the bright field image (Figure 6.1D). The RICM image (Figure 6.1E) shows the outline of the cell, and the even intensity shows that it adheres well to the poly-L-lysine coated substrate. The cells were also cotransfected with mRFP-UtrCH so that the actin filament network could be imaged independent of photoactivation (Figure 6.1F). Before activation, the 488 nm TIRF image shows very little intensity (Figure 6.1G). Figure 6.1H shows the photoactivated population 1.4 s after the beginning of the exposure to the scanning laser pattern. At 5.8 s (Figure 6.1I), the

pattern is blurred due to a combination of bleaching and diffusion/transport of PaGFP-UtrCH.

6.3.2 Spatial dynamics with singular value decomposition

The dynamics of the actin network are a complex interplay of polymerization and depolymerization rates in feedback with other cellular functions. Arp2/3 and WASP proteins, for example, nucleate filaments and control branching, which help define the size and density of actin filaments[172]. The function of actin cofactors is highly regulated within the cell, and it is therefore essential that the dynamics of the actin network be studied in situ. One limiting factor in imaging the actin network is its high density, which hinders observation of molecular turnover during polymerization and depolymerization. Speckle imaging[91] and single molecule tracking[173] are well-suited for molecular turnover assays because the fate of individual monomer units can be measured over time. Both methods, however, are limited in application and in the type of information one can obtain. Speckle imaging requires a specific density of fluorophore that is difficult to control experimentally, particularly in primary cell lines. More importantly, speckle microscopy requires an algorithm for particle identification and tracking that is prone to interpretive error[174]. Single molecule methods in live cells have been difficult in the past because the diffraction limit of optical microscopes limits the allowable density of fluorophores and thus undersamples the cortical actin meshwork. Photoactivatable probes have revived this method because small populations can be stochastically activated, localized, and tracked[173]. The weakness of this approach is that dynamic information is uncorrelated over the total acquisition time and that the duration of individual tracks is fundamentally limited by fluorophore bleaching.

Patterned photoactivation offers a complementary method to track small, spatially defined populations of molecules for longer times than other methods. The bright ensemble samples the pattern area, and intensity shifts out of the activation region can be directly related to molecular transport. To make the best use of patterned photoactivation time-lapse images, a quantitative method is needed to describe the time-evolution of the spatial distributions. In the few patterned photoactivation studies to date, the data have typically been quantified by measuring intensity decays/increases in user-defined regions of interest[156,157]. While simple and functional, this approach is prone to bias and does not make full use of the information available in the data. To overcome these limitations, we used SVD to decompose the time-dependent spatial distribution into components ranked by their contribution to the time-evolution of the data set. In this way, the spatial and temporal information was conserved and could be used to better characterize the dynamics of the system.

SVD is a commonly used algorithm that has found applications ranging from time-resolved spectroscopy to DNA microarray analysis[159–161,175]. In one typical application, SVD is used to analyze time-dependent spectroscopy data following a perturbation[160,161,176]. SVD simplifies the analysis of time-evolving spectra that are simultaneously undergoing peak shifts, line broadening, and frequency-dependent intensity changes. In a similar way, it is difficult to characterize time-lapse images of photopatterned regions that are shaped by multiple effects like bleaching, lateral diffusion, axial diffusion out of the observation volume, and directed transport or flow. In

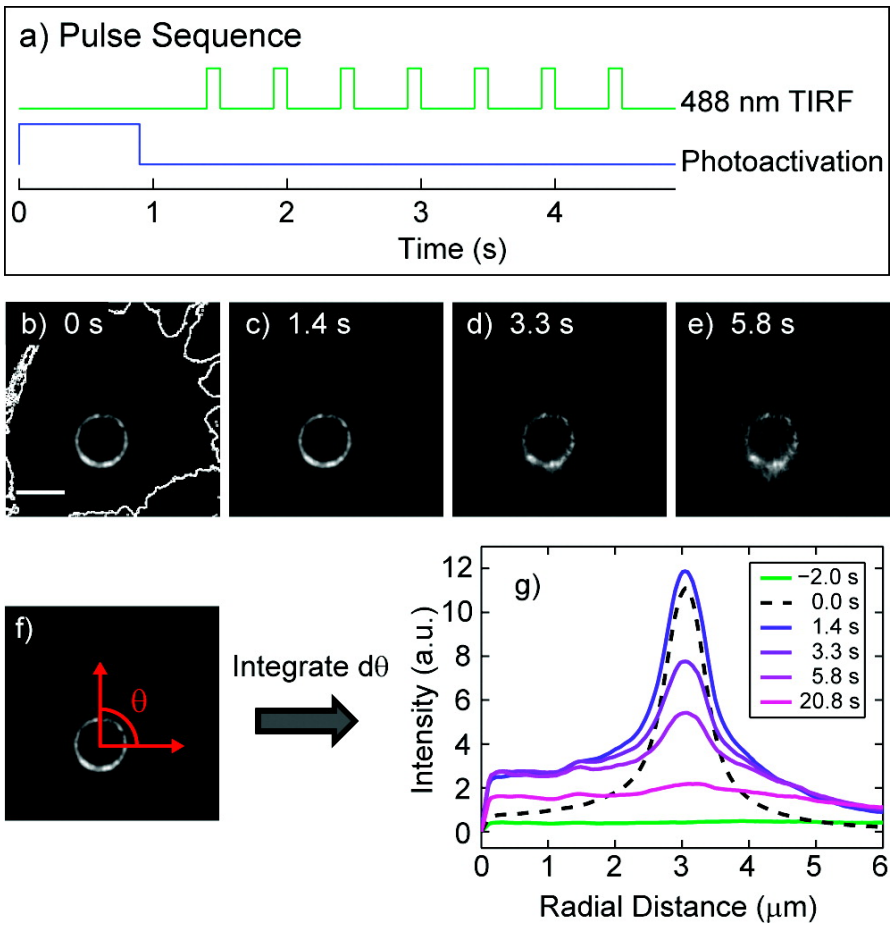


Figure 6.2. (**A**) Diagram of the image collection sequence shows the 900 ms photoactivation pulse followed by a 2 Hz pulse train of 100 ms exposures of 488 nm TIRF. (**B–E**) Selected images from time-lapse imaging of a live Cos-7 cell. At *t* = 0 s (**B**), the scanned circular pattern (3 μm radius) is exposed to the cell outlined in white. Subsequent 488 nm TIRF images are collected at the specified times. Image intensities are rescaled for each frame to highlight topology. (**F**) Each image is centered to the activation ring, transformed into polar coordinates, and integrated with respect to the angle. (**G**) Time series of integrated radial distributions used in the SVD analysis. Scale bar in (**B**) represents 5 μm.

the present work SVD is used to analyze the time-dependent, postphotoactivation images, where the pattern-activated ensemble is simultaneously shifting and decaying without a well-defined final state.

SVD analysis was first applied to PaGFP-UtrCH photoactivated in Cos-7 cells, which are nonmotile and in which the actin cytoskeleton is expected to be relatively stable based on an observed lack of filament turnover and actin flow. A 3 μm radius ring was photoactivated near the center of the cell (Figure 6.2B) using the pattern technique introduced in Figure 6.1B. Images are represented by the variable: I(*x,y,t*). The data are first reduced to two dimensions by taking advantage of the radial symmetry of the photoactivation pattern. This is motivated by the centro-symmetric retrograde flow in T-cells that will be discussed in the following section. The center of the activation annulus is defined as the origin, and the spatial *x* and *y* positions are transformed into polar coordinates. The image matrix is then integrated over the azimuthal angle, so that the traces represent the radial distribution of the fluorophores (see Figure 6.2F):

$$\mathbf{I}(x,y,t) \rightarrow \mathbf{I}(r,\theta,t);\ \mathbf{D}(r,t) = \int \mathbf{I}(r,\theta,t)\,d\theta$$

Several time points from the resultant data matrix, **D**(*r,t*), are shown in Figure 6.2G.

In the following implementation of SVD, **D**(*r,t*) is an *m*×*n* matrix, where the *m* dimension is the radial profile of the fluorescence intensity, *r* and *n*, is the time dimension, *t*. SVD decomposes **D** so that

$$\mathbf{D} = \mathbf{USV}^{\mathbf{T}}$$

Where **U** is an $m \times n$ matrix with n orthonormal basis states, $\mathbf{V}^{\mathbf{T}}$ is an $n \times n$ matrix with each row representing the time-evolution of the corresponding basis state, and **S** is an $n \times n$ diagonal matrix where elements $s_{i,i}$ are the singular values, or weighting factors.

The first three component basis states from the data in Figure 6.2 are shown in Figure 6.3C. The singular values $s_{1,1}$, $s_{2,2}$, and $s_{3,3}$ are 2.2×10^7, 3.9×10^6, and 6.8×10^5, respectively. The ratio of these values falls into a range where the first and second basis states represent the majority of the changes over time but cannot be rigorously separated from the other data. In this regime, the SVD analysis is analogous to a Fourier filter that isolates and ranks the dominant components of the time-dependent spatial distribution. For the time-lapse images shown in this report, the first component basis state (Figure 6.3C, blue) is nearly identical to the time average of $\mathbf{D}(r,t)$ (shown in Figure S2 in the associated manuscript[78]), and its weighting factor over time is dependent on total fluorophore intensity. The decay of the first component is shown in Figure 6.3D (blue) and is interpreted to represent photobleaching and axial transport of the fluorophores out of the TIRF excitation region. The second component basis state (Figure 6.3C, red) is very similar to the difference between the radial distributions over time (i.e., $\mathbf{D}(r,t = 0) - \mathbf{D}(r,t = 5\text{ s})$; see Figure S2 in the associated manuscript[78]). It is interpreted as the shift in the radial distribution of the fluorophores, so that the decay of the second component (Figure 6.3D, red) over time is assigned to lateral transport.

The first SVD basis state of the data above shows an even intensity inside the activation ring and slowly decaying intensity at increasing radial distance. The time decay of the first SVD component (Figure 6.3D, blue) is well described by a single exponential function with $\tau = 7.8$ s. This is interpreted as the time scale for photobleaching and axial migration of fluorophores out of the TIRF excitation volume. The second SVD basis state shows a maximum at the activation ring radius and two symmetric lobes of opposite sign away from the activation ring. This means that actin transport away from the activation ring has no directional bias toward or away from the center of the ring, as expected for a largely stable cytoskeletal network. The rate of lateral transport is found by fitting the time decay of the second component basis state to a single exponential function with $\tau = 2.8$ s.

To confirm that our interpretation of the SVD analysis was based on actual cytoskeletal dynamics, patterned photoactivation was also done on live and fixed Cos-7 cells under identical imaging conditions. The photoactivation area in this case was a 4 μm radius ring, and the postactivation time-lapse imaging protocol was similar to that shown in Figure 6.2. The lateral transport dynamics of the live cells, quantified as the decay of the second SVD component, are nearly identical to those in Figure 6.2 (data not shown), with an average $\tau = 3.8 \pm 0.6$ ($N = 5$). The fixed cells, however, show a dramatic difference in the profile of the first and second component basis states (Figure 6.3E) and in the time decay of the component coefficients (Figure 6.3F). The first component basis state ($s_{1,1} = 2.0 \times 10^8$) is 2 orders of magnitude larger than all the other components ($s_{2,2} = 1.8 \times 10^6$) and looks identical to the time average of the images. The first component coefficient does not decay appreciably with time, reflecting the fact that there is very little change in the radial profile or the intensity of the photoactivated fluorophore distribution. This is evidence that photobleaching may not play a dramatic role in the decay of the first component in the live cell data. While it is

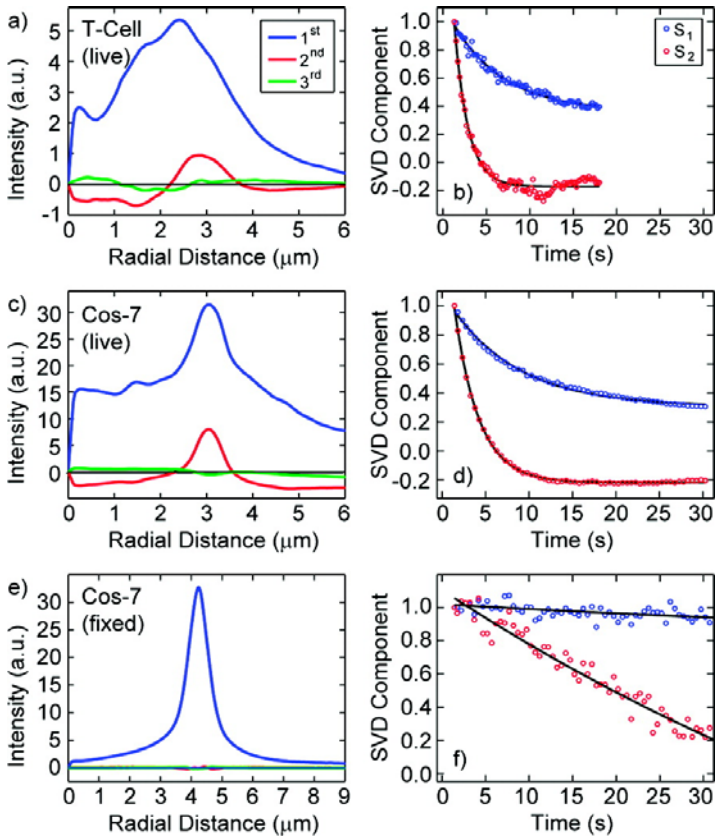


Figure 6.3. Summary of SVD results for three representative cells. Top row: Live T-cell. Panel (**A**) shows the first three SVD component states from the data in Figure 6.4 scaled by their value at t = 1.3 s. (**B**) The decays of the SVD components over time (normalized to t = 1.3 s) are fit to a single exponential function ($y = c + A \cdot e^{-t/\tau}$) with τ_{first} = 5.3 s and τ_{second} = 1.6 s. **Middle row**: Live Cos-7 cell. Panel (**C**) shows the first three SVD component states from the data in Figure 6.2 scaled by their value at t = 1.4 s. (**D**) The decays of the normalized SVD components over time are fit to the single exponential function above with τ_{first} = 7.8 s and τ_{second} = 2.8 s. **Bottom row**: Fixed Cos-7 cell. Panel (**E**) shows the first three SVD component states for data collected from fixed Cos-7 cells described in the text. (**F**) The decays of the normalized SVD components over time (up to 90 s) are fit to the single exponential function above with τ_{first} = 89 s and τ_{second} = 87 s. Note that the fitted time constants are at the end of the data series and therefore can only represent a lower bound to the time decay.

possible that the photostability of the fluorophores may be different in the two different environments, it is still likely that axial transport out of the TIRF illumination volume plays a major role in the decay of the first component basis state in live cells. The second component state of the fixed cells no longer looks like the difference in the radial distribution over time, and the decay of that component coefficient is very slow (>83 s). This is an expected result of the fixation process, which cross-links fluorophores and hinders their lateral transport. The identical set of experiments was performed on several cells, giving an average τ = 58 ± 33 (N = 4).

6.3.3 Actin dynamics in live T-cells

The actin cytoskeleton of T-cells is more dynamic than that of Cos-7 cells. It must enable T-cells in their native environment to crawl through narrow gaps in epithelial sheets in response to secreted chemokines. Upon T-cell antigen recognition on an antigen-presenting cell, the cytoskeleton adopts a pattern of planar, centrosymmetric retrograde flow characterized by actin polymerization near the cell periphery and net transport of monomers within filaments toward the center of the cell−cell interaction[72]. At the same time, the T-cell surface undergoes a dramatic actin-dependent protein rearrangement to generate an ordered T-cell/antigen-presenting cell interface known as the immunological synapse[68].

Exactly how the cytoskeleton acts to rearrange the surface proteins is still under debate. The Brownian ratchet model of actin monomer addition to a filament near a

fluctuating plasma membrane describes a mechanism by which actin polymerization can generate force[177,178]. When such a filament is able to move relative to the cell cortex, any proteins that are directly or indirectly coupled to it may be pulled by this polymerization-driven retrograde flow[46]. Alternatively, if the cargo protein itself is a site of filament nucleation, it may be pushed by a polymerizing but nonmotile filament[177]. Both mechanisms may also be affected by the presence of myosins, actin binding proteins that can actively move cargo along filaments, slide filaments with respect to each other, or anchor filaments to each other or to the cell substratum[179]. Actin retrograde flow has so far been observed in the immortalized Jurkat T-cell line using fluorescence speckle microscopy[14,17], and while this method has clearly shown monomer retrograde flow in this system, the characterization of larger-scale filament dynamics remains incomplete due to a lack of methodology to describe them. Furthermore, it is not well-established how Jurkat cell actin dynamics compare to those of primary T-cells.

We applied the SVD analysis to primary murine T-cells, which are nonmotile during their triggering, but which, unlike Cos-7 cells, have highly dynamic actin cytoskeletons. T-cells were retrovirally transduced with PaGFP-UtrCH and then presented to a supported lipid bilayer containing agonist peptide-major histocompatibility complex (pMHC) and intercellular adhesion molecules (ICAM-1), which is an established model system that triggers T-cell activation[53,68]. Each set of experiments also included fluorescent images of labeled T-cell receptors (TCR) and ICAM-1 to confirm that the cells under study were forming the canonical protein patterns at the immunological synapse (Figure S3 in the associated manuscript[78]).

Ring photoactivation patterns were used to follow the dynamics of the immunological synapse. First, a 3 μm radius ring was activated near the periphery of the cell, and images postactivation were recorded at 5 Hz frame rates. In Figure 6.4, several images are shown before, during, and after photoactivation, along with the corresponding radial profiles. The largest redistribution of intensity occurs between photoactivation and the first frame (1.3 s, Figure 6.4J), where the width of the main peak in the radial distribution is at least twice that of the original activation pattern. This is in contrast to the Cos-7 data, where the radial distribution at t = 1.4 s (Figure 6.2C) is very similar in width to the original photoactivation ring. We propose that this difference in the magnitude of immediate PaGFP redistribution between T-cells and Cos-7 cells is due to the presence, in T-cells, of highly mobile and potentially segmented actin filaments consistent with those cells' observed dynamic cytoskeletons. However, we cannot exclude the possibility that T-cells may contain a larger population of unbound PaGFP-UtrCH than Cos-7 cells. If this were the case, it would likely be due to a smaller-than-expected F-actin pool in T-cells relative to Cos-7 cells as opposed to relatively higher expression of the probe in the former cell type, since the absolute value of the PaGFP signal was very similar across both cell types.

The radial distribution profiles after 100 ms show a shift toward the center of the cell. This is seen in the peak maxima of the profiles in Figure 6.4J and in the second SVD component of the radial distribution profile (Figure 6.3A). The positive peak in the second SVD component at the ring radius and the negative intensity in the central region show that intensity is shifting inward with a time constant of 1.6 s. This same measurement was made in several cells that give an average time constant of 1.7 ± 0.4

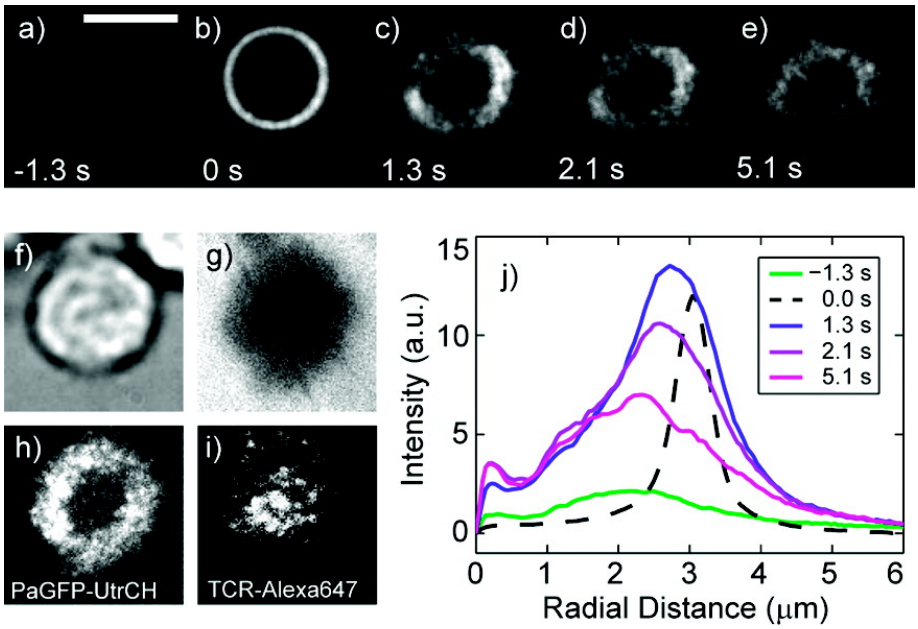


Figure 6.4. Photoactivation in live, antigen-activated T-cells. (**A**–**E**) Time-lapse images of PaGFP-UtrCH are taken at sample time points before (**A**), during (**B**), and after (**C**–**E**) photoactivation with the same pattern as in Figure 6.2. Bright field (**F**), RICM (**G**), PaGFP-UtrCH (**H**), and TCR-Alexa Fluor 647 (**I**) images are taken before photoactivation. (**J**) Integrated radial slices at sample time points corresponding to images above. Scale bar in (**A**) represents 5 μm.

s (N = 17). To test if the time constant for the second SVD component decay is dependent on the frame rate, we repeated the measurement in the same cell at 2 and 5 Hz acquisition frame rates. We found that the fitted time constants of the second SVD component decay at the two acquisition rates were 95% similar.

The shape and time decay of the second SVD component are evidence that F-actin is being transported from the periphery of the cell to the center, consistent with observations of retrograde flow[14,17,162]. Also visible in the images and radial profiles is an actin depletion zone with a radius of about 0.8 μm, which is consistent with previous experiments. A second measurement was performed on the same cell with a smaller activation radius that matched the actin depletion zone (Figure S4 in the associated manuscript[78]). As expected, there was little photoactivation corresponding to a low local actin concentration in that region, but there was additionally very little transport of F-actin out of the center of the immunological synapse. These data were also consistent with actin retrograde flow.

6.4 Discussion

In this work we have shown that patterned two-photon photoactivation and singular value decomposition can be used to track an ensemble of molecules in live cells. Circular activation patterns were analyzed by transforming the time-lapse images into a time series of radial distribution profiles. The time-evolution of the distribution profiles is well-described by the first two SVD component states. In activated T-cells the lateral redistribution is consistent with two types of motion. First, there is a fast spread of intensity out of the activation region that is faster than the lag time between photoactivation and the first image acquisition. This is attributed to highly dynamic filaments and unbound PaGFP-UtrCH. The second motion has a longer time constant as observed in the second component state, and is a measure of dynamic actin filaments migrating to the center of the cell. These results are consistent with a cortical

actin network that is mobile and undergoes continual retrograde flow. By contrast, in Cos-7 cells, radial actin distribution following photoactivation shows no directional bias, as expected for a more stable cytoskeletal network.

When the singular value decomposition method is used, it is possible to identify the dominant components of change in the lateral distribution of fluorophores within a single cell. This makes SVD a useful tool in the processing of image data from patterned photoactivation and patterned photobleaching experiments. One drawback of SVD is that the interpretation of the components and decays is dependent on the pattern. The ring patterns and radial profiles used in this study will not be appropriate for every application. For more general applications, the method can be applied directly to the images themselves without reducing them to a one-dimensional profile. An example of this is shown in Figure 6.5, which is the two-dimensional SVD of the images taken for Figure 6.2. Because of computational restrictions, we limit the analysis to a 150 × 150

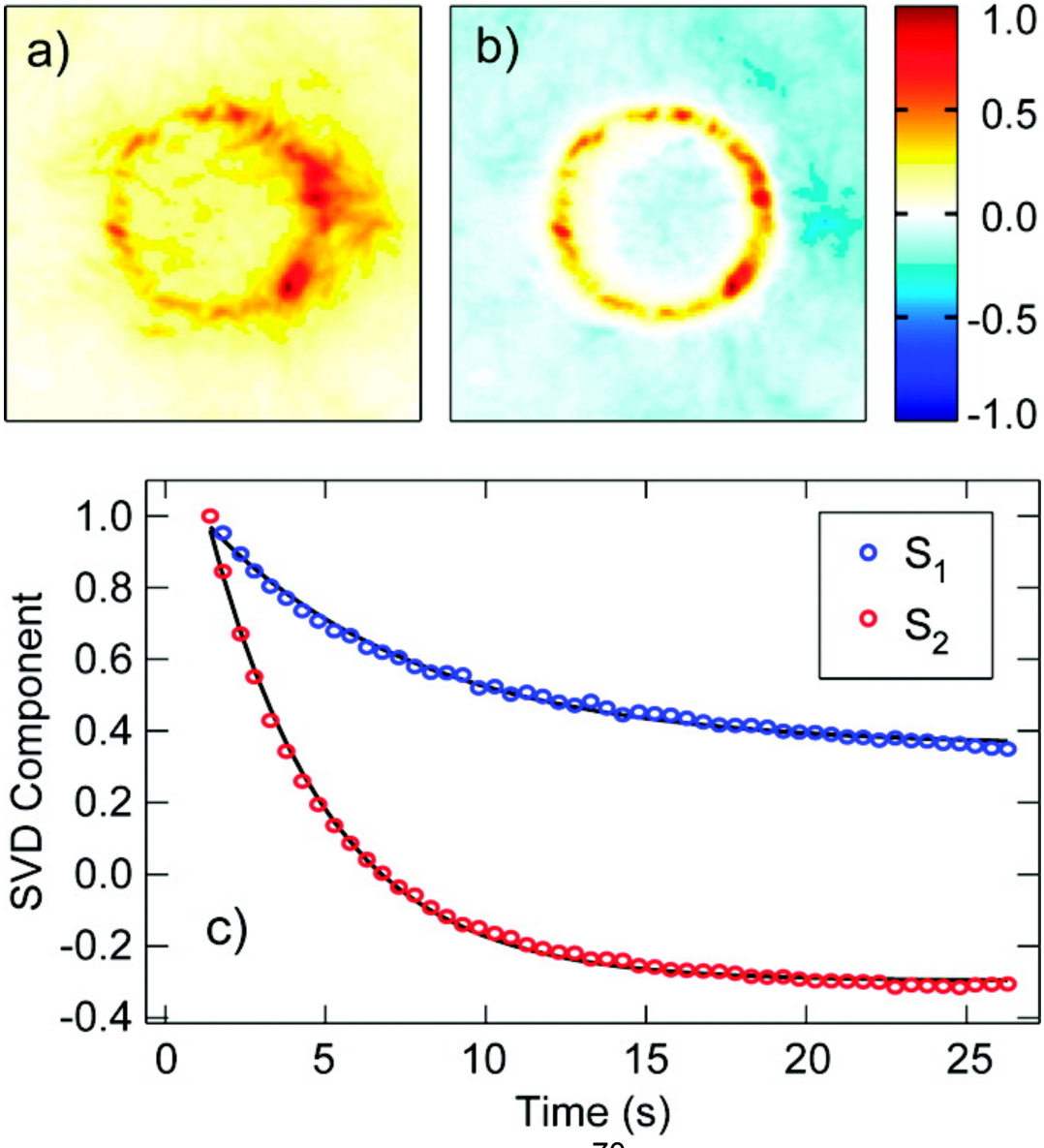


Figure 6.5. SVD whole-image analysis of the image sequence from Figure 6.2. Top panels show the first (**A**) and second (**B**) component states normalized to their respective maxima. (**C**) The decay of the image SVD components over time (normalized to t = 1.4 s) are fit to a single exponential function ($y = c + A \cdot e^{-t/\tau}$) with τ_{first} = 6.6 s and τ_{second} = 3.7 s.

pixel area. The first and second image components are analogous to those from the radial profile analysis in that the first component basis state represents the average of the image sequence and the second component basis state represents lateral transport. Furthermore, the time decays of the component coefficients match those in Figure 6.3 very well. This type of analysis could be used to quantify the dynamics of more complex photoactivation patterns in the future.

Fluorescence microscopy is a powerful tool for live cell experiments, but one must negotiate between labeling methods and imaging modalities. At high labeling densities the optical diffraction limit makes fine structures difficult to resolve. At low labeling densities it is possible to localize particles with high resolution, but the image features are susceptible to Nyquist aliasing, and the photophysics of the fluorophore limit the total time of observation. Photoactivatable fluorescent proteins have made it possible to control the effective fluorophore density within cells. With patterned photoactivation, a regime can be accessed between high and low labeling densities in which it is feasible to follow the dynamics of small populations of molecules with a well-defined starting point. By combining a system-motivated activation pattern with a quantitative image analysis tool like SVD, it is possible to make detailed observations of protein spatial dynamics within living cells.

Chapter 7

Closing remarks

This thesis has sought to address how the actomyosin cytoskeleton interacts with T-cell receptors in live T cells undergoing antigen-mediated activation. The work presented here confirms that actin slows and dynamically fluctuates at sites of trapped TCR clusters and shows that these fluctuations result from three-dimensional bunching of filamentous actin. Separately, it adds to the body of evidence supporting a role for actin in directly modulating TCR-pMHC interaction kinetics. It also demonstrates that while myosin IIA is dispensable for eventual immunological synapse formation, it is necessary for proper calcium flux during T-cell triggering.

Some of these results are observational in nature; consequently, it would be interesting to determine whether, for example, physical actin fluctuations correlate with the kinetic properties of the TCR. Additionally, because the experiments presented in this thesis have been performed using the supported lipid bilayer platform as a proxy for antigen-presenting cells, follow-on research will need to determine whether the observed behaviors occur at T cell-APC interfaces. Such a scientific direction opens up a host of new questions about what other factors present *in vivo* but absent from simple lipid bilayers contribute to the behaviors and responses of T-cell actin. Candidates include costimulatory molecules, the cytoskeleton, and even the topology of APCs, as well as the influence of the extracellular environment. A further level of inquiry would be how the TCR-actin interaction is affected by variability – how different are the responses of different TCRs to different peptide agonists presented on different MHCs by different classes of APCs in different cellular contexts.

To fully answer these questions, new techniques will need to be developed and established methods will need to be applied in innovative ways. Here, actin slowing was revealed using a custom speckle identification algorithm, dynamic enrichment was highlighted using image time-autocorrelation, and the bunching of filamentous actin was evidenced by a characteristic labeling pattern among two cytoskeletal probes of different colors. Similar methodological developments included direct single-molecule observation of agonist peptides interacting with TCRs and an application of singular value decomposition to analyze photoactivated probe redistribution in cells. Future work, particularly the interrogation of cytoskeletal behaviors at T cell-APC interfaces, will benefit from new ways of labeling, imaging, analyzing, and computationally modeling the cytoskeleton.

Bibliography

1. Wang, H. *et al.* ZAP-70: An Essential Kinase in T-cell Signaling. *Cold Spring Harbor Perspectives in Biology* **2**, (2010).

2. Sherman, E. *et al.* Functional Nanoscale Organization of Signaling Molecules Downstream of the T Cell Antigen Receptor. *Immunity* **35**, 705–720 (2011).

3. Nika, K. *et al.* Constitutively Active Lck Kinase in T Cells Drives Antigen Receptor Signal Transduction. *Immunity* **32**, 766–777 (2010).

4. Lillemeier, B. F. *et al.* TCR and Lat are expressed on separate protein islands on T cell membranes and concatenate during activation. *Nat Immunol* **11**, 90–96 (2010).

5. Barda-Saad, M. *et al.* Cooperative interactions at the SLP-76 complex are critical for actin polymerization. *EMBO J* **29**, 2315–2328 (2010).

6. Gomez, T. S. & Billadeau, D. D. T Cell Activation and the Cytoskeleton: You Can't Have One Without the Other. *Adv. Immunol.* **97**, 1–64 (2008).

7. Reicher, B. & Barda-Saad, M. Multiple pathways leading from the T-cell antigen receptor to the actin cytoskeleton network. *FEBS Letters* **584**, 4858–4864 (2010).

8. Geiger, B., Rosen, D. & Berke, G. Spatial relationships of microtubule-organizing centers and the contact area of cytotoxic T lymphocytes and target cells. *The Journal of Cell Biology* **95**, 137–143 (1982).

9. Ryser, J., Rungger-Brandle, E., Chaponnier, C., Gabbiani, G. & Vassalli, P. The area of attachment of cytotoxic T lymphocytes to their target cells shows high motility and polarization of actin, but not myosin. *J. Immunol.* **128**, 1159–1162 (1982).

10. Barda-Saad, M. *et al.* Dynamic molecular interactions linking the T cell antigen receptor to the actin cytoskeleton. *Nat. Immunol.* **6**, 80–89 (2005).

11. Billadeau, D. D., Nolz, J. C. & Gomez, T. S. Regulation of T-cell activation by the cytoskeleton. *Nat Rev Immunol* **7**, 131–143 (2007).

12. Dustin, M. L. Cell adhesion molecules and actin cytoskeleton at immune synapses and kinapses. *Current Opinion in Cell Biology* **19**, 529–533 (2007).

13. Beemiller, P. & Krummel, M. F. Mediation of T-Cell Activation by Actin Meshworks. *Cold Spring Harb. Perspect. Biol.* **2**, a002444 (2010).

14. Kaizuka, Y., Douglass, A. D., Varma, R., Dustin, M. L. & Vale, R. D. Mechanisms for segregating T cell receptor and adhesion molecules during immunological synapse formation in Jurkat T cells. *Proc. Natl. Acad. Sci. U.S.A.* **104**, 20296–20301 (2007).

15. Suzuki, J., Yamasaki, S., Wu, J., Koretzky, G. A. & Saito, T. The actin cloud induced by LFA-1-mediated outside-in signals lowers the threshold for T-cell activation. *Blood* **109**, 168 –175 (2007).

16. Jacobelli, J., Bennett, F. C., Pandurangi, P., Tooley, A. J. & Krummel, M. F. Myosin-IIA and ICAM-1 Regulate the Interchange between Two Distinct Modes of T Cell Migration. *The Journal of Immunology* **182**, 2041–2050 (2009).

17. Yu, C., Wu, H., Kaizuka, Y., Vale, R. D. & Groves, J. T. Altered actin centripetal retrograde flow in physically restricted immunological synapses. *PLoS ONE* **5**, e11878 (2010).

18. Smoligovets, A. A., Smith, A. W., Wu, H.-J., Petit, R. S. & Groves, J. T. Characterization of dynamic actin associations with T-cell receptor microclusters in primary T cells. *J. Cell Sci.* **125**, 735 –742 (2012).

19. Beemiller, P., Jacobelli, J. & Krummel, M. F. Integration of the movement of signaling microclusters with cellular motility in immunological synapses. *Nat Immunol* **13**, 787–795 (2012).

20. Yi, J., Wu, X. S., Crites, T. & Hammer, J. A. Actin Retrograde Flow and Acto-Myosin II Arc Contraction Drive Receptor Cluster Dynamics at the Immunological Synapse in Jurkat T-Cells. *Mol. Biol. Cell* **23**, 834–852 (2012).

21. Yu, Y., Fay, N. C., Smoligovets, A. A., Wu, H.-J. & Groves, J. T. Myosin IIA Modulates T Cell Receptor Transport and CasL Phosphorylation during Early Immunological Synapse Formation. *PLoS ONE* **7**, e30704 (2012).

22. Valitutti, S., Dessing, M., Aktories, K., Gallati, H. & Lanzavecchia, A. Sustained signaling leading to T cell activation results from prolonged T cell receptor occupancy. Role of T cell actin cytoskeleton. *The Journal of Experimental Medicine* **181**, 577–584 (1995).

23. Campi, G., Varma, R. & Dustin, M. L. Actin and agonist MHC-peptide complex-dependent T cell receptor microclusters as scaffolds for signaling. *J. Exp. Med.* **202**, 1031–1036 (2005).

24. Varma, R., Campi, G., Yokosuka, T., Saito, T. & Dustin, M. L. T Cell Receptor-Proximal Signals Are Sustained in Peripheral Microclusters and Terminated in the Central Supramolecular Activation Cluster. *Immunity* **25**, 117–127 (2006).

25. Rozdzial, M. M., Malissen, B. & Finkel, T. H. Tyrosine-phosphorylated T cell receptor zeta chain associates with the actin cytoskeleton upon activation of mature T lymphocytes. *Immunity* **3**, 623–633 (1995).

26. Yokosuka, T. *et al.* Newly generated T cell receptor microclusters initiate and sustain T cell activation by recruitment of Zap70 and SLP-76. *Nat. Immunol.* **6**, 1253–1262 (2005).

27. Tybulewicz, V. L. Vav-family proteins in T-cell signalling. *Current Opinion in Immunology* **17**, 267–274 (2005).

28. Gomez, T. S. *et al.* HS1 Functions as an Essential Actin-Regulatory Adaptor Protein at the Immune Synapse. *Immunity* **24**, 741–752 (2006).

29. Miletic, A. V. *et al.* Vav Links the T Cell Antigen Receptor to the Actin Cytoskeleton and T Cell Activation Independently of Intrinsic Guanine Nucleotide Exchange Activity. *PLoS ONE* **4**, e6599 (2009).

30. Miletic, A. V. *et al.* Vav1 Acidic Region Tyrosine 174 Is Required for the Formation of T Cell Receptor-induced Microclusters and Is Essential in T Cell Development and Activation. *Journal of Biological Chemistry* **281**, 38257–38265 (2006).

31. Ma, Z., Sharp, K. A., Janmey, P. A. & Finkel, T. H. Surface-Anchored Monomeric Agonist pMHCs Alone Trigger TCR with High Sensitivity. *PLoS Biol* **6**, e43 (2008).

32. Ma, Z. & Finkel, T. H. T cell receptor triggering by force. *Trends in Immunology* **31**, 1–6 (2010).

33. Kim, S. T. *et al.* The αβ T Cell Receptor Is an Anisotropic Mechanosensor. *Journal of Biological Chemistry* **284**, 31028 –31037 (2009).

34. Li, Y.-C. *et al.* Cutting Edge: Mechanical Forces Acting on T Cells Immobilized via the TCR Complex Can Trigger TCR Signaling. *The Journal of Immunology* **184**, 5959 –5963 (2010).

35. Husson, J., Chemin, K., Bohineust, A., Hivroz, C. & Henry, N. Force Generation upon T Cell Receptor Engagement. *PLoS ONE* **6**, e19680 (2011).

36. Adams, J. J. *et al.* T Cell Receptor Signaling Is Limited by Docking Geometry to Peptide-Major Histocompatibility Complex. *Immunity* **35**, 681–693 (2011).

37. Salazar-Fontana, L. I., Barr, V., Samelson, L. E. & Bierer, B. E. CD28 Engagement Promotes Actin Polymerization Through the Activation of the Small Rho GTPase Cdc42 in Human T Cells. *The Journal of Immunology* **171**, 2225–2232 (2003).

38. Huppa, J. B. *et al.* TCR-peptide-MHC interactions in situ show accelerated kinetics and increased affinity. *Nature* **463**, 963–967 (2010).

39. Huang, J. *et al.* The kinetics of two-dimensional TCR and pMHC interactions determine T-cell responsiveness. *Nature* **464**, 932–936 (2010).

40. Bunnell, S. C. *et al.* T cell receptor ligation induces the formation of dynamically regulated signaling assemblies. *The Journal of Cell Biology* **158**, 1263–1275 (2002).

41. Kusumi, A. *et al.* Paradigm Shift Of The Plasma Membrane Concept From The Two-Dimensional Continuum Fluid To The Partitioned Fluid: High-Speed Single-Molecule Tracking of Membrane Molecules. *Annual Review of Biophysics and Biomolecular Structure* **34**, 351–378 (2005).

42. Treanor, B. *et al.* The Membrane Skeleton Controls Diffusion Dynamics and Signaling through the B Cell Receptor. *Immunity* **32**, 187–199 (2010).

43. Treanor, B., Depoil, D., Bruckbauer, A. & Batista, F. D. Dynamic cortical actin remodeling by ERM proteins controls BCR microcluster organization and integrity. *The Journal of Experimental Medicine* **208**, 1055 –1068 (2011).

44. Andrews, N. L. *et al.* Actin restricts Fc[epsilon]RI diffusion and facilitates antigen-induced receptor immobilization. *Nat Cell Biol* **10**, 955–963 (2008).

45. DeMond, A. L., Mossman, K. D., Starr, T., Dustin, M. L. & Groves, J. T. T cell receptor microcluster transport through molecular mazes reveals mechanism of translocation. *Biophys. J.* **94**, 3286–3292 (2008).

46. Hartman, N. C., Nye, J. A. & Groves, J. T. Cluster size regulates protein sorting in the immunological synapse. *Proc. Natl. Acad. Sci. U.S.A.* **106**, 12729–12734 (2009).

47. Manz, B. N. & Groves, J. T. Spatial organization and signal transduction at intercellular junctions. *Nat. Rev. Mol. Cell Biol.* **11**, 342–352 (2010).

48. Groves, J. T. & Kuriyan, J. Molecular mechanisms in signal transduction at the membrane. *Nat Struct Mol Biol* **17**, 659–665 (2010).

49. Dustin, M. L. & Depoil, D. New insights into the T cell synapse from single molecule techniques. *Nat Rev Immunol* **11**, 672–684 (2011).

50. Dustin, M. L. & Groves, J. T. Receptor Signaling Clusters in the Immune Synapse. *Annu. Rev. Biophys.* **41**, 543–556 (2012).

51. Seminario, M.-C. & Bunnell, S. C. Signal initiation in T-cell receptor microclusters. *Immunological Reviews* **221**, 90–106 (2008).

52. Choudhuri, K. & Dustin, M. L. Signaling microdomains in T cells. *FEBS Letters* **584**, 4823–4831 (2010).

53. Mossman, K. D., Campi, G., Groves, J. T. & Dustin, M. L. Altered TCR signaling from geometrically repatterned immunological synapses. *Science* **310**, 1191–1193 (2005).

54. Vicente-Manzanares, M., Ma, X., Adelstein, R. S. & Horwitz, A. R. Non-muscle myosin II takes centre stage in cell adhesion and migration. *Nat Rev Mol Cell Biol* **10**, 778–790 (2009).

55. Betapudi, V. Myosin II Motor Proteins with Different Functions Determine the Fate of Lamellipodia Extension during Cell Spreading. *PLoS ONE* **5**, e8560 (2010).

56. Arii, J. *et al.* Non-muscle myosin IIA is a functional entry receptor for herpes simplex virus-1. *Nature* **467**, 859–862 (2010).

57. Bhuwania, R. *et al.* Supervillin couples myosin-dependent contractility to

podosomes and enables their turnover. *Journal of Cell Science* **125**, 2300–2314 (2012).

58. Jacobelli, J., Chmura, S. A., Buxton, D. B., Davis, M. M. & Krummel, M. F. A single class II myosin modulates T cell motility and stopping, but not synapse formation. *Nat Immunol* **5**, 531–538 (2004).

59. Smith, A., Bracke, M., Leitinger, B., Porter, J. C. & Hogg, N. LFA-1-induced T cell migration on ICAM-1 involves regulation of MLCK-mediated attachment and ROCK-dependent detachment. *Journal of Cell Science* **116**, 3123–3133 (2003).

60. Sanchez-Madrid, F. & Serrador, J. M. Bringing up the rear: defining the roles of the uropod. *Nat Rev Mol Cell Biol* **10**, 353–359 (2009).

61. Jacobelli, J. *et al.* Confinement-optimized three-dimensional T cell amoeboid motility is modulated via myosin IIA-regulated adhesions. *Nat Immunol* **11**, 953–961 (2010).

62. Wülfing, C. & Davis, M. M. A Receptor/Cytoskeletal Movement Triggered by Costimulation During T Cell Activation. *Science* **282**, 2266–2269 (1998).

63. Ilani, T., Vasiliver-Shamis, G., Vardhana, S., Bretscher, A. & Dustin, M. L. T cell antigen receptor signaling and immunological synapse stability require myosin IIA. *Nat Immunol* **10**, 531–539 (2009).

64. Kumari, S. *et al.* T lymphocyte myosin IIA is required for maturation of the immunological synapse. *Front. Immun.* **3**, 230 (2012).

65. Babich, A. *et al.* F-actin polymerization and retrograde flow drive sustained PLCγ1 signaling during T cell activation. *J. Cell Biol.* **197**, 775–787 (2012).

66. Hashimoto-Tane, A. *et al.* Dynein-Driven Transport of T Cell Receptor Microclusters Regulates Immune Synapse Formation and T Cell Activation. *Immunity* **34**, 919–931 (2011).

67. Monks, C. R. F., Freiberg, B. A., Kupfer, H., Sciaky, N. & Kupfer, A. Three-dimensional segregation of supramolecular activation clusters in T cells. *Nature* **395**, 82–86 (1998).

68. Grakoui, A. *et al.* The Immunological Synapse: A Molecular Machine Controlling T Cell Activation. *Science* **285**, 221–227 (1999).

69. Lee, K.-H. *et al.* T Cell Receptor Signaling Precedes Immunological Synapse Formation. *Science* **295**, 1539–1542 (2002).

70. Dustin, M. L., Chakraborty, A. K. & Shaw, A. S. Understanding the Structure and Function of the Immunological Synapse. *Cold Spring Harb. Perspect. Biol.* **2**, (2010).

71. Bunnell, S. C., Kapoor, V., Trible, R. P., Zhang, W. & Samelson, L. E. Dynamic Actin Polymerization Drives T Cell Receptor-Induced Spreading: A Role for the Signal Transduction Adaptor LAT. *Immunity* **14**, 315–329 (2001).

72. Burkhardt, J. K., Carrizosa, E. & Shaffer, M. H. The Actin Cytoskeleton in T Cell Activation. *Annu. Rev. Immunol.* **26**, 233–259 (2008).

73. Tanimura, N. *et al.* Dynamic changes in the mobility of LAT in aggregated lipid rafts upon T cell activation. *J. Cell Biol.* **160**, 125–135 (2003).

74. Bartelt, R. R., Cruz-Orcutt, N., Collins, M. & Houtman, J. C. D. Comparison of T Cell Receptor-Induced Proximal Signaling and Downstream Functions in Immortalized and Primary T Cells. *PLoS ONE* **4**, e5430 (2009).

75. Dobson-Belaire, W. N., Cochrane, A., Ostrowski, M. A. & Gray-Owen, S. D. Differential Response of Primary and Immortalized CD4+ T Cells to Neisseria gonorrhoeae-Induced Cytokines Determines the Effect on HIV-1 Replication. *PLoS ONE* **6**, e18133 (2011).

76. Groves, J. T., Ulman, N. & Boxer, S. G. Micropatterning Fluid Lipid Bilayers on Solid Supports. *Science* **275**, 651–653 (1997).

77. Burkel, B. M., Von Dassow, G. & Bement, W. M. Versatile fluorescent probes for actin filaments based on the actin-binding domain of utrophin. *Cell Motil. Cytoskeleton* **64**, 822–832 (2007).

78. Smith, A. W., Smoligovets, A. A. & Groves, J. T. Patterned Two-Photon Photoactivation Illuminates Spatial Reorganization in Live Cells. *J. Phys. Chem. A* **115**, 3867–3875 (2011).

79. Ballestrem, C., Wehrle-Haller, B. & Imhof, B. Actin dynamics in living mammalian cells. *J. Cell Sci.* **111**, 1649–1658 (1998).

80. Kaye, J. *et al.* Selective development of CD4+ T cells in transgenic mice expressing a class II MHC-restricted antigen receptor. *Nature* **341**, 746–749 (1989).

81. Xu, C. & Prince, J. L. Snakes, shapes, and gradient vector flow. *IEEE Trans. Image Process.* **7**, 359–369 (1998).

82. Thompson, R. E., Larson, D. R. & Webb, W. W. Precise Nanometer Localization Analysis for Individual Fluorescent Probes. *Biophys. J.* **82**, 2775–2783 (2002).

83. Saxton, M. J.in *Fundamental Concepts in Biophysics* 1–33 (Humana Press, 2009).at <http://dx.doi.org/10.1007/978-1-59745-397-4_6>

84. Betzig, E. *et al.* Imaging Intracellular Fluorescent Proteins at Nanometer Resolution. *Science* **313**, 1642–1645 (2006).

85. Rust, M. J., Bates, M. & Zhuang, X. Sub-diffraction-limit imaging by stochastic optical reconstruction microscopy (STORM). *Nat. Methods* **3**, 793–796 (2006).

86. Mossman, K. D. & Groves, J. T. Micropatterned supported membranes as tools for quantitative studies of the immunological synapse. *Chem. Soc. Rev.* **36**, 46–54 (2007).

87. Nye, J. A. & Groves, J. T. Kinetic Control of Histidine-Tagged Protein Surface Density on Supported Lipid Bilayers. *Langmuir* **24**, 4145–4149 (2008).

88. Dustin, M. L. Supported bilayers at the vanguard of immune cell activation studies. *J. Struct. Biol.* **168**, 152–160 (2009).

89. Groves, J. T. & Boxer, S. G. Micropattern Formation in Supported Lipid Membranes. *Acc. Chem. Res.* **35**, 149–157 (2002).

90. Salaita, K. *et al.* Restriction of Receptor Movement Alters Cellular Response: Physical Force Sensing by EphA2. *Science* **327**, 1380–1385 (2010).

91. Waterman-Storer, C. M., Desai, A., Chloe Bulinski, J. & Salmon, E. D. Fluorescent speckle microscopy, a method to visualize the dynamics of protein assemblies in living cells. *Curr. Biol.* **8**, 1227–1230 (1998).

92. McQuarrie, D. A. *Statistical Mechanics*. (University Science Books, 2000).

93. Petersen, N. O., Hoddelius, P. L., Wiseman, P. W., Seger, O. & Magnusson, K. E. Quantitation of membrane receptor distributions by image correlation spectroscopy: concept and application. *Biophys. J.* **65**, 1135–1146 (1993).

94. Wiseman, P. W. *et al.* Spatial mapping of integrin interactions and dynamics during cell migration by Image Correlation Microscopy. *J. Cell Sci.* **117**, 5521–5534 (2004).

95. Hebert, B., Costantino, S. & Wiseman, P. W. Spatiotemporal Image Correlation Spectroscopy (STICS) Theory, Verification, and Application to Protein Velocity Mapping in Living CHO Cells. *Biophys. J.* **88**, 3601–3614 (2005).

96. Kulkarni, R. P., Wu, D. D., Davis, M. E. & Fraser, S. E. Quantitating intracellular transport of polyplexes by spatio-temporal image correlation spectroscopy. *Proc. Natl. Acad. Sci. U.S.A.* **102**, 7523–7528 (2005).

97. Rossow, M., Mantulin, W. W. & Gratton, E. Spatiotemporal image correlation spectroscopy measurements of flow demonstrated in microfluidic channels. *J. Biomed. Opt.* **14**, 024014–7 (2009).

98. Edelstein, A., Amodaj, N., Hoover, K., Vale, R. & Stuurman, N. Computer Control of Microscopes Using μManager. *Curr. Prot. Mol. Biol.* **92**, 14.20.1–14.20.17 (2010).

99. Al-Alwan, M. M., Rowden, G., Lee, T. D. G. & West, K. A. Cutting Edge: The Dendritic Cell Cytoskeleton Is Critical for the Formation of the Immunological Synapse. *J. Immunol.* **166**, 1452 –1456 (2001).

100. Hsu, C.-J. *et al.* Ligand Mobility Modulates Immunological Synapse Formation and T Cell Activation. *PLoS ONE* **7**, e32398 (2012).

101. Patla, I. *et al.* Dissecting the molecular architecture of integrin adhesion sites by cryo-electron tomography. *Nat. Cell Biol.* **12**, 909–915 (2010).

102. Irvine, D. J., Purbhoo, M. A., Krogsgaard, M. & Davis, M. M. Direct observation of ligand recognition by T cells. *Nature* **419**, 845–849 (2002).

103. Manz, B. N., Jackson, B. L., Petit, R. S., Dustin, M. L. & Groves, J. T-cell triggering thresholds are modulated by the number of antigen within individual T-cell receptor clusters. *Proceedings of the National Academy of Sciences* **108**, 9089–9094 (2011).

104. Huse, M. *et al.* Spatial and Temporal Dynamics of T Cell Receptor Signaling with a Photoactivatable Agonist. *Immunity* **27**, 76–88 (2007).

105. Tian, S., Maile, R., Collins, E. J. & Frelinger, J. A. CD8+ T Cell Activation Is Governed by TCR-Peptide/MHC Affinity, Not Dissociation Rate. *The Journal of Immunology* **179**, 2952–2960 (2007).

106. Matsui, K., Boniface, J. J., Steffner, P., Reay, P. A. & Davis, M. M. Kinetics of T-cell receptor binding to peptide/I-Ek complexes: correlation of the dissociation rate with T-cell responsiveness. *Proceedings of the National Academy of Sciences* **91**, 12862–12866 (1994).

107. Newell, E. W. *et al.* Structural Basis of Specificity and Cross-Reactivity in T Cell Receptors Specific for Cytochrome c–I-Ek. *The Journal of Immunology* **186**, 5823–5832 (2011).

108. Stone, J. D., Chervin, A. S. & Kranz, D. M. T-cell receptor binding affinities and kinetics: impact on T-cell activity and specificity. *Immunology* **126**, 165–176 (2009).

109. Crocker, J. C. & Grier, D. G. Methods of Digital Video Microscopy for Colloidal Studies. *Journal of Colloid and Interface Science* **179**, 298–310 (1996).

110. Ensign, D. L. & Pande, V. S. Bayesian Detection of Intensity Changes in Single Molecule and Molecular Dynamics Trajectories. *J. Phys. Chem. B* **114**, 280–292 (2009).

111. Lin, W.-C., Yu, C.-H., Triffo, S. & Groves, J. T.in *Current Protocols in Chemical Biology* (John Wiley & Sons, Inc., 2009).at <http://dx.doi.org/10.1002/9780470559277.ch100131>

112. Axmann, M., Huppa, J. B., Davis, M. M. & Schütz, G. J. Determination of Interaction Kinetics between the T Cell Receptor and Peptide-Loaded MHC Class II via Single-Molecule Diffusion Measurements. *Biophysical Journal* **103**, L17–L19 (2012).

113. Valitutti, S., Muller, S., Cella, M., Padovan, E. & Lanzavecchia, A. Serial triggering of many T-cell receptors by a few peptide–MHC complexes. *Nature* **375**, 148–151 (1995).

114. Govern, C. C., Paczosa, M. K., Chakraborty, A. K. & Huseby, E. S. Fast on-rates allow short dwell time ligands to activate T cells. *Proceedings of the National Academy of Sciences* **107**, 8724–8729 (2010).

115. Robert, P. *et al.* Kinetics and Mechanics of Two-Dimensional Interactions between T Cell Receptors and Different Activating Ligands. *Biophysical Journal* **102**, 248–257 (2012).

116. Ha, T. *et al.* Single-molecule fluorescence spectroscopy of enzyme conformational dynamics and cleavage mechanism. *Proceedings of the National Academy of Sciences* **96**, 893–898 (1999).

117. Evans, E. A. & Calderwood, D. A. Forces and Bond Dynamics in Cell Adhesion. *Science* **316**, 1148–1153 (2007).

118. Palmer, E. & Naeher, D. Affinity threshold for thymic selection through a T-cell receptor-co-receptor zipper. *Nat Rev Immunol* **9**, 207–213 (2009).

119. Grecco, H. E., Schmick, M. & Bastiaens, P. I. H. Signaling from the Living Plasma Membrane. *Cell* **144**, 897–909 (2011).

120. Scott, J. D. & Pawson, T. Cell Signaling in Space and Time: Where Proteins Come Together and When They're Apart. *Science* **326**, 1220–1224 (2009).

121. Loose, M., Fischer-Friedrich, E., Ries, J., Kruse, K. & Schwille, P. Spatial Regulators for Bacterial Cell Division Self-Organize into Surface Waves in Vitro. *Science* **320**, 789–792 (2008).

122. Lee, K.-H. *et al.* The Immunological Synapse Balances T Cell Receptor Signaling and Degradation. *Science* **302**, 1218–1222 (2003).

123. Doh, J. & Irvine, D. J. Immunological synapse arrays: Patterned protein surfaces that modulate immunological synapse structure formation in T cells. *Proceedings of the National Academy of Sciences* **103**, 5700–5705 (2006).

124. Groves, J. T., Parthasarathy, R. & Forstner, M. B. Fluorescence Imaging of Membrane Dynamics. *Annu. Rev. Biomed. Eng.* **10**, 311–338 (2008).

125. Wei, Q. & Adelstein, R. S. Conditional Expression of a Truncated Fragment of Nonmuscle Myosin II-A Alters Cell Shape but Not Cytokinesis in HeLa Cells. *Molecular Biology of the Cell* **11**, 3617–3627 (2000).

126. Takács, B. *et al.* Myosin complexed with ADP and blebbistatin reversibly adopts a conformation resembling the start point of the working stroke. *Proceedings of the National Academy of Sciences* **107**, 6799–6804 (2010).

127. Bubb, M. R., Spector, I., Beyer, B. B. & Fosen, K. M. Effects of Jasplakinolide on the Kinetics of Actin Polymerization: AN EXPLANATION FOR CERTAIN IN VIVO OBSERVATIONS. *Journal of Biological Chemistry* **275**, 5163–5170 (2000).

128. Otsu, N. A threshold selection method from gray-level histograms. *IEEE Transactions on Systems, Man and Cybernetics* **9**, 62–66 (1979).

129. Cai, Y. *et al.* Nonmuscle Myosin IIA-Dependent Force Inhibits Cell Spreading and

Drives F-Actin Flow. *Biophysical Journal* **91**, 3907–3920 (2006).

130. Giannone, G. *et al.* Periodic Lamellipodial Contractions Correlate with Rearward Actin Waves. *Cell* **116**, 431–443 (2004).

131. Aratyn-Schaus, Y. & Gardel, M. L. Transient Frictional Slip between Integrin and the ECM in Focal Adhesions under Myosin II Tension. *Current Biology* **20**, 1145–1153 (2010).

132. Sakamoto, T., Limouze, J., Combs, C. A., Straight, A. F. & Sellers, J. R. Blebbistatin, a Myosin II Inhibitor, Is Photoinactivated by Blue Light. *Biochemistry* **44**, 584–588 (2004).

133. Kovács, M., Thirumurugan, K., Knight, P. J. & Sellers, J. R. Load-dependent mechanism of nonmuscle myosin 2. *Proceedings of the National Academy of Sciences* **104**, 9994–9999 (2007).

134. Lewis, R. S. CALCIUM SIGNALING MECHANISMS IN T LYMPHOCYTES. *Annu. Rev. Immunol.* **19**, 497–521 (2001).

135. Bolte, S. & Cordelieres, F. P. A guided tour into subcellular colocalization analysis in light microscopy. *Journal of Microscopy* **224**, 213–232 (2006).

136. Ohashi, Y., Tachibana, K., Kamiguchi, K., Fujita, H. & Morimoto, C. T Cell Receptor-mediated Tyrosine Phosphorylation of Cas-L, a 105-kDa Crk-associated Substrate-related Protein, and Its Association of Crk and C3G. *Journal of Biological Chemistry* **273**, 6446–6451 (1998).

137. Ohashi, Y., Iwata, S., Kamiguchi, K. & Morimoto, C. Tyrosine Phosphorylation of Crk-Associated Substrate Lymphocyte-Type Is a Critical Element in TCR- and β1 Integrin-Induced T Lymphocyte Migration. *The Journal of Immunology* **163**, 3727–3734 (1999).

138. Minegishi, M. *et al.* Structure and function of Cas-L, a 105-kD Crk-associated substrate-related protein that is involved in beta 1 integrin-mediated signaling in lymphocytes. *The Journal of Experimental Medicine* **184**, 1365–1375 (1996).

139. Kanda, H. *et al.* Fyn and Lck tyrosine kinases regulate tyrosine phosphorylation of p105CasL, a member of the p130Cas docking protein family, in T-cell receptor-mediated signalling. *Immunology* **97**, 56–61 (1999).

140. Sawada, Y. *et al.* Force Sensing by Mechanical Extension of the Src Family Kinase Substrate p130Cas. *Cell* **127**, 1015–1026 (2006).

141. Alexander, N. R. *et al.* Extracellular Matrix Rigidity Promotes Invadopodia Activity. *Current Biology* **18**, 1295–1299 (2008).

142. Zheng, M. & McKeown-Longo, P. J. Cell adhesion regulates Ser/Thr phosphorylation and proteasomal degradation of HEF1. *Journal of Cell Science* **119**,

96–103 (2006).

143. Liu, X. *et al.* A novel ability of Smad3 to regulate proteasomal degradation of a Cas family member HEF1. *EMBO J* **19**, 6759–6769 (2000).

144. Ingber, D. E. Mechanobiology and diseases of mechanotransduction. *Ann Med* **35**, 564–577 (2003).

145. Levental, K. R. *et al.* Matrix Crosslinking Forces Tumor Progression by Enhancing Integrin Signaling. *Cell* **139**, 891–906 (2009).

146. Vogel, V. & Sheetz, M. Local force and geometry sensing regulate cell functions. *Nat Rev Mol Cell Biol* **7**, 265–275 (2006).

147. Engler, A. J., Sen, S., Sweeney, H. L. & Discher, D. E. Matrix Elasticity Directs Stem Cell Lineage Specification. *Cell* **126**, 677–689 (2006).

148. Reedquist, K. A. *et al.* Stimulation through the T Cell Receptor Induces Cbl Association with Crk Proteins and the Guanine Nucleotide Exchange Protein C3G. *Journal of Biological Chemistry* **271**, 8435–8442 (1996).

149. Gelkop, S., Babichev, Y. & Isakov, N. T Cell Activation Induces Direct Binding of the Crk Adapter Protein to the Regulatory Subunit of Phosphatidylinositol 3-Kinase (p85) via a Complex Mechanism Involving the Cbl Protein. *Journal of Biological Chemistry* **276**, 36174–36182 (2001).

150. Hell, S. W. Far-Field Optical Nanoscopy. *Science* **316**, 1153–1158 (2007).

151. Lukyanov, K. A., Chudakov, D. M., Lukyanov, S. & Verkhusha, V. V. Photoactivatable fluorescent proteins. *Nat Rev Mol Cell Biol* **6**, 885–890 (2005).

152. Schneider, M., Barozzi, S., Testa, I., Faretta, M. & Diaspro, A. Two-Photon Activation and Excitation Properties of PA-GFP in the 720–920-nm Region. *Biophysical Journal* **89**, 1346–1352 (2005).

153. Post, J. N., Lidke, K. A., Rieger, B. & Arndt-Jovin, D. J. One- and two-photon photoactivation of a paGFP-fusion protein in live Drosophila embryos. *FEBS Letters* **579**, 325–330 (2005).

154. Stark, D. A. & Kulesa, P. M. An in vivo comparison of photoactivatable fluorescent proteins in an avian embryo model. *Dev. Dyn.* **236**, 1583–1594 (2007).

155. Murray, M. J. & Saint, R. Photoactivatable GFP resolves Drosophila mesoderm migration behaviour. *Development* **134**, 3975–3983 (2007).

156. Martini, J. *et al.* Multifocal two-photon laser scanning microscopy combined with photo-activatable GFP for in vivo monitoring of intracellular protein dynamics in real time. *Journal of Structural Biology* **158**, 401–409 (2007).

157. Chen, Y., Macdonald, P. J., Skinner, J. P., Patterson, G. H. & Müller, J. D.

Probing nucleocytoplasmic transport by two-photon activation of PA-GFP. *Microsc. Res. Tech.* **69**, 220–226 (2006).

158. Wiesmeijer, K., Krouwels, I. M., Tanke, H. J. & Dirks, R. W. Chromatin movement visualized with photoactivable GFP-labeled histone H4. *Differentiation* **76**, 83–90 (2008).

159. Wall, M., Rechtsteiner, A. & Rocha, L.in *A Practical Approach to Microarray Data Analysis* (Berrar, D. P., Dubitzky, W. & Granzow, M.) 91–109 (Springer US, 2003).at <http://www.springerlink.com/content/x035256j0h64h187/abstract/>

160. Hofrichter, J. *et al.* Nanosecond optical spectra of iron-cobalt hybrid hemoglobins: geminate recombination, conformational changes, and intersubunit communication. *Biochemistry* **24**, 2667–2679 (1985).

161. Shrager, R. I. & Hendler, R. W. Titration of individual components in a mixture with resolution of difference spectra, pKs, and redox transitions. *Anal. Chem.* **54**, 1147–1152 (1982).

162. Lin, C.-H., Thompson, C. A. & Forscher, P. Cytoskeletal reorganization underlying growth cone motility. *Current Opinion in Neurobiology* **4**, 640–647 (1994).

163. Tsai, P. *et al.* Principles, design, and construction of a two photon laser scanning microscope for in vitro and in vivo brain imaging. *In vivo optical imaging of brain function* 113–171 (2002).

164. Pantazis, P. & González-Gaitán, M. Localized multiphoton photoactivation of paGFP in Drosophila wing imaginal discs. *J. Biomed. Opt* **12**, 044004–044004 (2007).

165. Pear, W. S., Nolan, G. P., Scott, M. L. & Baltimore, D. Production of high-titer helper-free retroviruses by transient transfection. *Proceedings of the National Academy of Sciences* **90**, 8392–8396 (1993).

166. Nguyen, Q.-T., Tsai, P. S. & Kleinfeld, D. MPScope: A versatile software suite for multiphoton microscopy. *Journal of Neuroscience Methods* **156**, 351–359 (2006).

167. Riedl, J. *et al.* Lifeact: a versatile marker to visualize F-actin. *Nat Meth* **5**, 605–607 (2008).

168. Doyle, T. & Botstein, D. Movement of yeast cortical actin cytoskeleton visualized in vivo. *Proceedings of the National Academy of Sciences* **93**, 3886–3891 (1996).

169. Aizawa, H., Sameshima, M. & Yahara, I. A Green Fluorescent Protein-actin Fusion Protein Dominantly Inhibits Cytokinesis, Cell Spreading, and Locomotion in Dictyostelium. *Cell Structure and Function* **22**, 335–345 (1997).

170. Hozumi, S. *et al.* An unconventional myosin in Drosophila reverses the default handedness in visceral organs. *Nature* **440**, 798–802 (2006).

171. Wu, J.-Q. & Pollard, T. D. Counting Cytokinesis Proteins Globally and Locally in

Fission Yeast. *Science* **310**, 310–314 (2005).

172. Rohatgi, R. *et al.* The Interaction between N-WASP and the Arp2/3 Complex Links Cdc42-Dependent Signals to Actin Assembly. *Cell* **97**, 221–231 (1999).

173. Manley, S. *et al.* High-density mapping of single-molecule trajectories with photoactivated localization microscopy. *Nat Meth* **5**, 155–157 (2008).

174. Vallotton, P. & Small, J. V. Shifting views on the leading role of the lamellipodium in cell migration: speckle tracking revisited. *Journal of Cell Science* **122**, 1955–1958 (2009).

175. Chung, H. S., Khalil, M. & Tokmakoff, A. Nonlinear Infrared Spectroscopy of Protein Conformational Change during Thermal Unfolding. *J. Phys. Chem. B* **108**, 15332–15342 (2004).

176. Chen, W.-G. & Braiman, M. S. Kinetic Analysis of Time-Resolved Infrared Difference Spectra of the L and M Intermediates of Bacteriorhodopsin. *Photochemistry and Photobiology* **54**, 905–910 (1991).

177. Theriot, J. A. The Polymerization Motor. *Traffic* **1**, 19–28 (2000).

178. Fletcher, D. A. & Geissler, P. L. Active Biological Materials. *Annu. Rev. Phys. Chem.* **60**, 469–486 (2009).

179. Wilson, C. A. *et al.* Myosin II contributes to cell-scale actin network treadmilling through network disassembly. *Nature* **465**, 373–377 (2010).